Generation and post modification of nanoparticles by plasmas

A Dissertation by

Amir Mohammad Ahadi

Submitted in partial fulfillment
of the Requirements
for the Degree of
Doctor of Philosophy

Faculty of Engineering
Christian-Albrechts-Universität zu Kiel

September 2016

1. First examiner:	Prof. Dr. Franz Faupel
2. Second examiner:	Prof. Dr. Holger Kersten
Date of Examination:	25/Feb/2016

To my lovely family & my Parents

Declaration

Hereby, I, Amir Mohammad Ahadi, declare that content of this thesis is my original work which is prepared based on my knowledge to fulfill the objectives of this study. Research Foundation I certify that this dissertation does not contain any material which has been previously submitted to any other university or equivalent institution for any academic degree. This thesis has been prepared subject to the rules of good scientific practice of the German.

Amir Mohammad Ahadi

Date: Signature:

Abstract

Generation, deposition and functionalization of nanoparticles (NPs) have received much numerous attention during the last decades due to the outstanding features of NPs and their unique roles in adjusting different properties of advanced materials. This dissertation includes three individual projects focused on synthesis and modification of different NPs based on using plasmas. Finding correlations between the plasma parameters and the observed phenomena is very crucial in this study. Particularly, we investigate metal and oxide-metal NP formation by a gas aggregation source (GAS) combined with conventional DC and/or pulsed DC magnetron sputtering. Utilizing a hollow electrode to modify metal NPs by a radio frequency discharge and also synthesis of semiconductor NPs by nonthermal plasma technique are other investigated subjects in current work. Stable production and controlled formation of NPs are two important challenges in novel technology. The first part of this dissertation is devoted to investigating the NP formation of highly reactive metals. Our quantitatively assessment reveals that the NP generation of reactive metals, using a GAS combined with magnetron sputtering technique, is possible only in the presence of a small content of reactive gas admixture in the nucleation region. The NP formation for such a system strongly depends on competition between sputtering process and target poisoning process. The outstanding role of the reactive gas admixture, the pressure and the applied power on the TiO_x NP generation are demonstrated by using different material characterization methods. We succeed to practically stabilize the formation of TiO_x NPs for a long term by establishing the equilibrium between sputtering and poisoning processes. At typical operating conditions, tuning the oxygen admixture is a key factor to get the equilibrium. The presented model for the NP formation can precisely interpret our findings. Feeding the magnetron with a pulsed DC power (instead of conventional DC power) increases the rate of NP generation considerably. Investigating the role of oxygen in the clustering process and also the influence of pulsing parameters clarifies the dominant mechanisms at this regime. Plasma with specific characteristics is vastly employed, as a desired system, for material processing in advanced technologies. The next part of this dissertation is focused on the plasma characterization of a hollow electrode discharge and the influence of the ignited discharge, in radio frequency (RF) regime, on metal NPs. The stable RF discharge and high electron density at low gas pressures are big advantages of the used configuration. It is demonstrated that the ignited discharge can significantly change the characteristics of the passing NP beam

by charging metal NPs and redistributing them in the beam. Semiconductor NPs are main constitutes of the novel photovoltaic and optoelectronic devices. Since the desired properties of the fabricated structures are strongly influenced by the physical and chemical properties of the semiconductor NPs, control over the synthesis process is very important. The last part of this research is devoted to study the synthesis of germanium (Ge) NPs in a nonthermal plasma reactor. It is shown that by adjusting the gas composition, and consequently varying the dominant mechanisms in the plasma, the size, crystallinity and surface chemistry of the synthesized Ge NPs can be controlled.

Acknowledgements

During last years, several persons in different ways, have positively influenced on my life and research work. They will be in my heart and their memories will be with me, forever.

First, I would like to express my deep gratitude to my main advisor and mentor; Prof. Farnz Faupel for giving the opportunity to work in his group and for his incredible support during my research. I appreciate the wisdom, time and patient he has given to me. I am also grateful my second advisor Prof. Holger Kersten in group of plasma technology who allowed me to work in his group and for his helpful scientific comments in our meetings. He has helped me to learn more about plasma technology during my PhD. I deeply acknowledge Dr. Thomas Strunskus for supervision this work and for his collaboration in different steps of my research. I have received several whitening comments and arguments from his side, especially, in preparing of our articles. I should thank Shahid Chamran (Jondishapour) university of Ahvaz and Iran ministry of science and technology for financial support. I am also much thankful to Dr. Oleksandr Polonskyi, for his collaboration during most parts of my PhD work. He always shared his great experiences with me, during our incredible discussions. Many thanks to Alexander Hinz for his assistance in performing some experiments and also measuring several TEM samples. I am also grateful to Maryam Nojabaee and Waqas Saddique for their helps in some parts of this dissertation as a student assistant. I am sending my sincere grateful to Dr. Vladimir Zaporojtchenko, who initially supervised this work but unfortunately, he unexpectedly left us very soon. I would like to thank Dr. Thomas Trottenberg for his effective cooperation in characterizations of hollow discharge and writing the corresponding publications. I also appreciate him for the time, scientific comments and several discussions in our joint project. I express my sincere acknowledgments to my best friends; Dr. Mehdi Keshavarz Hedayati, Ali Tavassolizadeh and Babak Mozooni who made a warm atmosphere for me and my family, here, in Kiel. I appreciate their continuous helps, kindly guidance and sharing their experiences in different ways. During my PhD, I had a chance to visit the lab of Prof.Uwe Kortshagen in university of Minnesota for a short term where I performed experiments on particle synthesis in nonthermal plasmas. It was a wonderful time and instructive experience for me. I am grateful Prof. Kortshagen who allowed me to join his group and doing experiments in his advanced Lab. I also thank my nice friend, Dr. Nicolaas Kramer in group of Prof. Kotshagen. I learned so many things about their lab systems and also valuable details of the new project during discussions with

him. He greatly helped me to be adopted with the new environment in the USA. I would like to acknowledge the technicians of our group, Stefan Rehder and Christoph Ochmann for constructing and maintaining the mechanical and electronic devices and also, Rainer Kloth and Peter Sommer for maintaining the software systems and surviving our computers. Additionally, I sincerely thank the secretaries of our group; Sieglinde Kastaun and Nicole Gühlke who helped me in the administration process. I would also like to thank all my group mates, especially; Dr. Jian Xiong and Bodo Henkel, who provided a friendly atmosphere in our work office.

I can not find words to express my sincere grateful to my parents who are the best for me. They raised me up under their unlimited kindness and support. Their endless encouragements always push me towards the best levels. I wish all the best for them. My lovely sisters and their families and also my dear brother, have non-deniable roles in my life. I would like to hearty thank them for their selfless support and wish all the best for their own life and dreams. Last but not the least, I should express the most profound gratitude to my wife who has an outstanding role in my life. She was with me everywhere during last years and patiently tolerated so many difficulties. Her encouragements, selfless support and unconditional love provided a great atmosphere for me during my PhD. She also kindly spent all of her time and energy to take care our son, Parham, during my writing. Finally, I would thank my smart angel, Parham, who could not see me for long periods during preparing this dissertation.

Amir Mohammad Ahadi

Kiel, 2016

Publications and Presentations

Peer-reviewed Articles

- ***A. M. Ahadi***, V. Zaporojtchenko, T. Peter, O. Polonskyi, T. Strunskus and F. Faupel, "Role of reactive gas admixtures in stabilizing nanocluster deposition from a gas aggregation source", *Journal of Nanoparticles Research*, 15 (12), 2125 (2013).

- ***A. M. Ahadi***, O. Polonskyi, U. Schürmann, T. Strunskus and F. Faupel, "Stable production of TiO_x nanoparticles with narrow size distribution by reactive pulsed dc magnetron sputtering", *Journal Physics D : Applied Physics*, 48 (3), 35501 (2015)

- ***A. M. Ahadi***, T. Trottrnberg, S. Rehders, T. Strunskus, H. Kersten and F. Faupel, "Characterization of a radio frequency hollow electrode discharge at low gas pressures", *Physics of Plasmas*, 22, 83513 (2015)

- ***A. M. Ahadi***, A. Hinz, O. Polonskyi, T. Strunskus, T. Trottrnberg, H. Kersten and F. Faupel, "Modification of a metal nanoparticle beam by a hollow electrode discharge", *Journal of Vacuum Science and Technology A*, 34 (2), 21301 (2016)

- ***A. M. Ahadi***, N. J. Keramer, T. Strunskus, H. Kersten, F. Faupel and U. R. Kortshagen, "Controlled synthesis of germanium nanopartilces by nonthermal plasmas", *submitted to Applied Physics Letters* (2015)

- T. Peter, O. Polonskyi, B. Gojdka, ***A. M. Ahadi***, T. Strunskus, V. Zaporojtchenko, H. Biederman and F. Faupel, "Influence of reactive gas admixture on transition metal cluster nucleation in a gas aggregation cluster source", *Journal of Applied Physics*, 112, 114321 (2012).

- O. Polonskyi, T. Peter, ***A. M. Ahadi***, A. Hinz, T. Strunskus, V. Zaporojtchenko, H. Biederman and F. Faupel, "Huge increase in gas phase cluster generation by reactive pulsed DC sputtering", *Applied Physics Letters*, 103, 033118 (2013).

Conference: Presentations and Posters

- ***A. M. Ahadi***, V. Zaporojtchenko, A. M. Hinz, T. Peter, O. Polonskyi, T. Strunskus and F. Faupel, "Role of oxygen on stabilization of TiO_x cluster production by gas aggregation cluster source", *DFG meeting*, 10 - 15 March 2013, Regensburg - Germany.

- ***A. M. Ahadi***, O. Polonskyi, T. Strunskus, V. Zaporojtchenko and F. Faupel, "Study of cluster formation by DC and pulsed DC magnetron sputtering in a gas aggregation source", 18^{th} *Summer school on low temperature plasma physics*, 5 - 10 Oct 2013, Bad Honnef - Germany.

- ***A. M. Ahadi***, T. Trottenberg, O. Polonskyi, T. Strunskus, H. Kersten and F. Faupel, "Influence of RF hollow cathode discharge on metal nanocluster beam",2^{nd} *German - Czech workshop Nanoparticles from low temperature plasma and their applications*, 23 - 24 May 2014, Prague - Czech Republic.

- ***A. M. Ahadi***, T. Trottenberg, O. Polonskyi, T. Strunskus, H. Kersten and F. Faupel, "RF hollow discharge and its influence on metal nanoclusters", 4^{th} *Graduate Summer Institute "Complex Plasmas"*, 30 July - 8 August 2014, South Orange - USA.

- F. Faupel, V. Zaporojtchenko, T. Peter, ***A. M. Ahadi***, T. Strunskus, S. Zabel, O. Polonskyi and H. Biederman, "Critical Influence of oxygen on the formation of titanium nanoparticles for deposition of titania thin films from a gas aggregation cluster source", *Material Science Engineering (MSE)*, 25 - 27 Sep 2012, Darmstadt - Germany.

- O. Polonskyi, T. Peter, ***A. M. Ahadi***, A. Hinz, T. Strunskus, V. Zaporojtchenko, H. Biederman and F. Faupel, "High deposition rate of metal (oxide) nanoclusters generated in pulsed DC magnetron sputtering system", *DFG meeting*, 10 - 15 March 2013, Regensburg - Germany.

- T. Strunskus, O. Polonskyi, T. Peter, ***A. M. Ahadi***, V. Zaporojtchenko, H. Biederman and F. Faupel, "Preparation of nanoparticles and nanocomposites through high efficiency cluster generation in the gas phase by reactive pulsed DC sputtering", *European congress and exhibition on advanced materials and processes (EuroMat)*, 8 - 13 Sep 2013, Sevilla - Spain.

- O. Polonskyi, T. Peter, ***A. M. Ahadi***, T. Strunskus and F. Faupel, "Highly efficient transition metal nanoparticle generation in the gas phase by pulsed DC magnetron sputtering", 6^{th} *International Workshop on Polymer Metal Nanocomposites*, 16 - 18 Sep 2013, Toulouse - France.

- O. Polonskyi, ***A. M. Ahadi***, A. Hinz, E. Vasiliauskaite, T. Strunskus and F. Faupel, " Metal and metal oxide nanoparticles generated in gas phase by pulsed DC sputtering in a reactive gas admixture", *DFG meeting*, 17 - 21 March 2014, Berlin - Germany.

- T. Strunskus, O. Polonskyi, ***A. M. Ahadi***, T. Peter and F. Faupel, "Influence of reactive gas admixtures on transition metal nanoparticles deposition by gas aggregation

cluster source", 2^{nd} *German - Czech workshop Nanoparticles from low temperature plasma and their applications*, 23 - 24 May 2014, Prague - Czech Republic.

– O. Polonskyi, E. Vasiliauskaite, ***A. M. Ahadi***, A. Hinz, T. Strunskus and F. Faupel, "Highly efficient transition metal nanoparticle generation in the gas phase by reactive pulsed DC magnetron sputtering", 2^{nd} *German - Czech workshop Nanoparticles from low temperature plasma and their applications*, 23 - 24 May 2014, Prague - Czech Republic.

– O. Polonskyi, ***A. M. Ahadi***, T. Strunskus and F. Faupel, "The effect of different gas admixtures on nanoparticles formation in a gas aggregation source and their treatment by hollow cathode plasma", 7^{th} *International Workshop on Polymer Metal Nanocomposites*, 2 - 5 Nov 2015, Jaipur - India.

Contents

Preface

This dissertation, as a cumulative thesis, is prepared based on the papers which have been published in peer review journals. Five chapters of the current thesis are devoted to the five original articles of which I am the first author (chapters 2-6). I have contributed to all experiments, data analysis and writing the text of these papers. For using of each article, and also other published materials such as individual figures, a written permission from the publisher was obtained. The styles of the articles have properly been changed in the way to fulfill the thesis format. The size and numbering of figures and tables and the citations in the text, were correspondingly adopted too.

The first chapter of this thesis is devoted to a comprehensive introduction where the basic concepts of this work and also the utilized characterization methods are reviewed. Some results of the current research have already been published in other papers where I have contributed to them as co-author. They are briefly discussed in the first chapter and used as preliminary works for the next chapters. In the last chapter of this dissertation, the summary and outlook of this work are presented.

Amir Mohammad Ahadi
Christian Albrechts University of Kiel

Acronyms and Symbols

D.R. Deposition Rate

IR Infrared

XRD X-Ray diffraction

XPS X-Ray Photoelectron Spectroscopy

TEM Transmission Electron Microscope

SEM Scanning Electron Microscope

FTIR Fourier Transform Infrared Spectroscopy

PVD Physical Vapor Deposition

RF Radio Frequency

DC Direct Current

TMP Turbo Molecular Pump

GAS Gas Aggregation Source

QMS Quadrupole Mass Spectrometer

NP Nanoparticle

NC Nanocrystal

FWHM Full Width of Half Maximum

eV electron Volt

sccm Standard-state Cubic Centimetres per Minute

UHV Ultra High Vacumm

G Gauge

B Baratron

SP Scroll Pump

a.u. arbitrary unit

O Oxygen

Ar Argon

Ag Silver

Ti Titanium

Si Silicon

Ge Germanium

Ni Nickel

Co Cobalt

Cu Copper

HRTEM High Rsolution Transmission Electron Microscope

SAED Selected Area Electron Diffraction

HC Hollow Cathode

$\mathbf{V}_P$ Plasma potential

$\mathbf{V}_f$ Floating potential

$\mathbf{r}_W$ Wigner-Seitz radius

T Temperature

λ Wavelength

Chapter 1

Introduction

The peculiar properties of nanoparticles (NPs) and their role in adjusting optical, chemical, electrical and physical properties of nanocomposite materials and nanodevices, represent their importance in today's science [1, 2]. Furthermore, the vast applications of NPs in biocompatible sensors, optoelectronic devices, solar cells and energy storage devices attracted significant attention to the NP synthesis and tailored applications. The physical properties of NPs are not the same as those of either liquids or gases instead, they show a new form of matter. Furthermore, the NP beams are useful tools for the investigation of the fundamentals of solid sate physics, chemistry and related materials science.

Among several employed techniques for NP generation [3], gas phase routes are desired for fundamental investigations and detailed study of transition from atomic scale physics to bulk material. Additionally, gas phase approaches have high ability to form NPs from a wide range of materials. The physical and chemical properties of the NPs produced by these methods can be highly controlled by operating conditions. In such a synthesis approach, atoms and molecules as main constitutes, can build up the NPs through condensation of a supersaturated vapor or by chemical reaction of precursor species. The concentration of nucleus, temperature and pressure of the vapor, determine the dominant mechanism of the NP growth [4]. Gas phase processes are environmentally benign as they are not connected to liquid effluents. The cleaning of liquid effluents is difficult and costly. Synthesis based on reactions in the gas phase is based on purely random processes for particle formation. In general, this leads to a broad distribution of particle sizes and, in some variants of these processes, to the formation of NPs. There are applications where the broad NP size distributions are disadvantageous. To solve this problem, many process variants and nuances in processing were developed. A broad group of gas phase processes is connected to the plasma. Within the large group of plasma processes for NP synthesis, a very special class of methods is connected to plasma produced by electrical systems. The other processes where plasma is involved apply laser or just high temperatures for excitation. Some of the processes work at ambient pressure, however, most of plasma processes at reduced gas pressure. Another means to differentiate plasma processes is based on the precursors. They may be gaseous, solid, liquid, or solutions. Sorting the size, geometry classification and the ability to modify

the physical or chemical properties of NPs are the current challenges of using NPs in the technological breakthroughs [4].

The main goal of this thesis is focused on the generation and modification of various NPs based on gas phase approaches. In these methods different plasmas, with exclusive properties, play outstanding roles in the NP formation and modification processes by providing the seeds and interaction with the NPs.

Gas aggregation source (GAS) is a desired system to produce NPs from a wide range of materials such as; metals [5], oxide metals [6], polymers [7] and semiconductors [8]. The metal NP generation by a GAS combined with a magnetron sputtering, was initially introduced by Haberland at 1992 [9]. Nowadays this approach is known as a very effective route for metal and oxide metal NP generation. Using a magnetized plasma to sputter off the target atoms (or/and species) is the first step of the NP formation by this technique. So many factors of the applied discharge can directly (or indirectly) influence on nucleation and growth processes in the GAS. Particularly, in the case of adding a reactive gas admixture into the GAS volume, the dominant mechanisms in the plasma are much more complicated. In spit of several investigations, many aspects of this approach are remained intact from physical and technical point of view. For instance, the physics of NP charging in the GAS and the role of different parameters such as working pressure, orifice dimensions and shape, magnetron power and working gas, are not well known yet. The complexity of the processes and hardly access into the GAS system are the main difficulties of study on this technique.

As has been demonstrated [10], the NP generation from a reactive metal such as titanium is not possible by using the conventional DC sputtering in a pure noble gas atmosphere. As Marek et al. [11] and Peter et al. [10] have shown, switching to reactive sputtering is a beneficial solution to overcome this problem. However, as will be discussed later, adding reactive gas admixture to the inlet gas can directly switch the magnetron sputtering from metallic to ceramic mode by forming a poisoned layer on the target. Additionally, the presence of the reactive gas can effectively change the plasma parameters by producing chemically active compounds in the volume. These phenomena inherently have dynamic natures and their corresponding effects are gradually changed with time. Consequently, a stable NP formation will not be resulted in this regime. This instability is undesired for film deposition. Furthermore, forming a poisoned layer on the target surface, reduces the active area in sputtering and subsequently, the clustering process in the GAS is decelerated by decreasing the seed density.

Next two chapters (chapter 2 and 3) of this dissertation are devoted to the TiO_x NP generation from a titanium target. It will be demonstrated that the NP formation by a GAS combined with the reactive magteron sputtering, can be stabilized by establishing an equilibrium between the poisoning and sputtering process. Tuning the reactive admixed gas is an important factor to achieve the equilibrium. The certain content of reactive gas admixture (which results the stable NP generation) strongly depends on the applied power, the working pressure and the chemical activity of the used target material [12]. Furthermore, using pulsed power can increase the rate of NP deposition by enhancing the sputtering rate [6, 13]. The concentration of oxygen admixture, not only changes the chemistry of NPs

and the rate of NP formation, but also, in the pulsed DC regime, it can significantly influence on the size of NPs [6]. The role of reactive gas admixture in the clustering process and the dominant mechanisms in different operating regimes are investigated in those chapters by presenting a proper model.

During production of nanomaterials, employing several processing techniques to generate, modify, functionalize and combine, different constitutes are needed. Varying the operating parameters of the applied technique can dramatically change the properties of the resulted nanomaterials. Therefore, control over individual process is a crucial step in the fabrication of functional nanomaterials with desired properties. Furthermore, the applied techniques for production and processing of each species can undesirably affect other constitutes. Hence, employing separate environments for each process is almost preferred. Although, performing different processes in the separated environments is a helpful solution to control individual mechanism, but combining these processes through matching the operating conditions is usually difficult. Additionally, when a complex medium like plasma, is required for material processing, interactions between different species and interpreting the observed behavior will be much more complicated. As the next project of this research, a cylindrical electrode is utilized to ignite symmetric radio frequency (RF) discharges at the low pressure regime for material processing. In chapter 4, by employing different plasma characterization methods, several aspects of the RF discharge are studied. The ignited plasma interestingly resembles a hollow cathode discharge at RF regime. High electron density at different operating conditions offers a suitable environment for plasma polymerization and functionalization of NPs. The influence of the RF discharge on metal NPs at regulated operating conditions is investigated by combining the hollow electrode with a GAS. The obtained results (chapter 5) elucidate that the RF plasma can significantly change the feature of the NPs deposited spot. Furthermore, most of the NPs are negatively charged in the discharge volume.

Semiconductor materials are characterized by bandgaps between 0.5 and 3 eV, which makes them ideal materials for many electronic and optical applications. Semiconductors are now vastly used in microelectronic circuits and also light emitting devices and light detectors [14]. While the bandgap of bulk semiconductors is not easily changed, the bandgap of semiconductor nanocrystals (NCs) can be adjusted over quite wide ranges based on a mechanism known as quantum confinement [15]. The optical and electrical properties of semiconductor NPs (and NCs), promising technological applications of this type of materials. Since the size and shape of NCs determine their chemical and physical properties, the controlled synthesis process is very important. As will be discussed in the current chapter, the nonthermal plasmas are a very suitable system for synthesis NCs from precursors.

According to the previous reports [14, 16, 17], the NPs with desired characters can be generated by adjusting the operation conditions, such as the working pressure, the residence time and the discharge power. Herein, as the last part of this dissertation, we concentrate on the role of gas composition in the synthesis process of germanium (Ge) NPs as a novel route to control the NPs properties. Germanium NCs may be of interest for a variety of electronic and optoelectronic applications including photovoltaics, due to the tunability of their band gap from the infrared into the visible range of the spectrum [17]. Data analyzing

(in the chapter 6), obviously reveals that the chemistry of the gas species has a key role in the synthesis process. The NPs with desired size, surface chemistry and crytallinity can be synthesized in nonthermal plasma by tuning the concentration of admixed reactive gas.

This is a cumulative dissertation. In the following chapter (chapter 1), a comprehensive introduction to the next chapters is presented and the basics of different employed techniques are overviewed. Furthermore, some practical results which are used as preliminary experiments for the next chapters are presented in the following chapter. Next five chapters are devoted to the five articles which have been published in peer review journals wherein the author of the current thesis was the main contributor and also the first author. The summary and the outlook of this work are given in the last chapter (chapter 7).

1.1 Magnetron sputtering

Magnetron sputtering is routinely used in industry for a broad range of application due to increasing demand for qualified functional films in different markets [18, 19]. Furthermore, so many scientific works have been reported on the physics of magnetron sputtering [18–21]. Since we frequently use this system to provide vaporized metal atoms in a GAS, a brief review over the physics of magnetron sputtering is presented in this section.

Sputtering is called to the mechanism of detachment atomic size particles from a substance (target) by impacting fast ions. During ion-target collision, transferred momentum to the target removes atomic size particles from the target. These sputtered species can fly to a substrate and condense on it, to cast a thin film. Volatilization any material, the stoichiometry of the gasified compound and uniform film deposition over large areas are the advantages of this technique [22]. Furthermore, in comparison with other physical vapor deposition methods, more energetic sputtered atoms are generated by sputtering.

Different physical approaches can be engaged to produce fast ions for sputtering process. Plasmas, with specific properties, are used as desired system to accelerate ions for sputtering. The plasma ions can be accelerated in the potential of the plasma sheath near the target and get sufficient energy for sputtering. During the ion bombardment, secondary electrons are emitted, as byproducts, from the target. These electrons have a vital role in surviving the discharge. The sputtering by this method is restricted by low deposition rate (D.R.) and low plasma ionization [19]. To avoid losing kinetic energy of the sputtered atoms and also reducing their backscattering, a magnetic field is usually employed. This magnetic field can also reduce the work pressure of the plasma. Nowadays, well modified magnetron sputtering with special magnetic field configuration is used to overcome the sputtering limitations. The magnets, in the used magnetron, are arranged beyond the target as; one central pole placed coaxial with the target and second pole, consists several magnets arranged like a ring, surrounds the central pole with a small gap (Figure 1.1). The created magnetic field, by this arrangement of magnets, can confine the plasma electrons in the vicinity of the target. Increasing the plasma density causes more ionization and more ion bombardments of the target which gives a higher sputtering rate. Furthermore, stable plasma can be ignited at

lower pressure.

One should note that the energy of impacting ions is not totally spent in the sputtering process and acceleration of atoms, but some of the ion's energy is transferred to the target as thermal energy which can crack or melt the target. This thermal energy also influences on the magnets and change the magnetic field configuration. For avoiding these problems, the magnetrons are usually equipped with a cooling system to dissipate the thermal energy released during operation.

The magnetron plasma can be considered as a dynamic system which depends on the interaction of the sputtered atoms and the background discharge (gas). Collisions between the sputtered species and the background gas result in a rarefied gas. Then on the given discharge current, the electron temperature should be sufficiently high to sustain the current by holding the ionization at a consistent level [18].

The ratio of the number of sputtered atoms to the number of impacting ions is named *sputtering yield*. This factor strongly depends on the used gas species (mass), energy and impact angel of ions and also the target material. As a general rule, ions with higher energy can proportionally increase the sputtering yield. Furthermore, materials such as gold and silver have high yields while the refractory materials and compounds have relatively low yields [19].

In this dissertation, a commercial magnetron (ION′X2 UHV, Thin Film Consulting) equipped with a flat circular target is used. The argon discharge was applied to produce fast ions for sputtering. For plasma ignition the system was powered with a DC power supply (MDX 500) provided by Advanced Energy. The applied DC power was in the range of 20–120 W. The silver and titanium targets provided by Good Follow, with 50 mm in diameter and 6 mm in thickness, were used. The inert gas streams through a narrow channel with 1 mm width, around the magnetron. A scheme of the used magnetron system is displayed in Figure 1.1.

1.2 Reactive magnetron sputtering

Magnetron sputtering in the presence of reactive gas species is known as reactive magnetron sputtering. This type of sputtering is already applied to cast a wide variety of thin film deposition, particularly oxides, nitrides and carbides. This technique provides a possibility to deposit non-conductive films from a metallic target by reacting the metal particles with reactive species. This reaction can be happened on the surface of the target, on the substrate or on the fly path of the sputtered atoms from the target to the substrate (in the volume).

The reactive species not only can change the chemistry of resulting films, but can also vary the sputtering rate from the target. Furthermore, they can influence on the discharge chemistry and plasma parameters. Chemical reactions between the reactive species and the top atoms of the target is known as *poisoning process* which results in an insulating layer on the target surface. The poisoned zones will be shielded with respect to the sputtering process

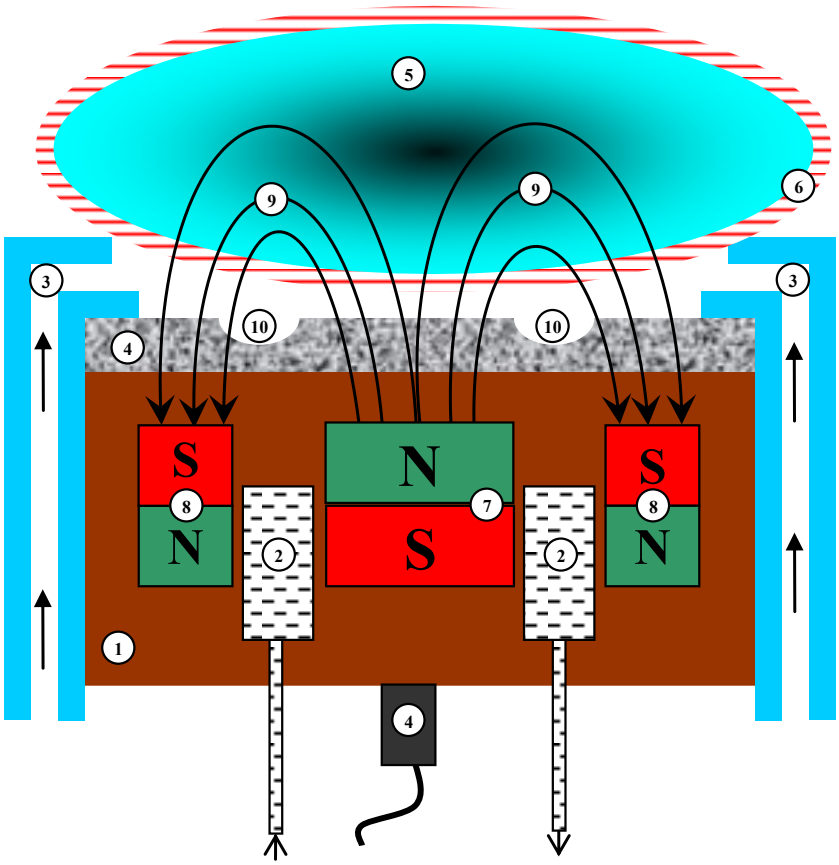

Figure 1.1: *Schematic drawing of the used magnetron system. 1) copper cathode, 2) water cooling 3) inlet gas channel 4) metal target 5) discharge 6) discharge sheath 7) central magnet 8) edge magnets 9) magnetic field lines 10) erosion zone.*

because the incoming ions in the poisoned area cannot be discharged and subsequently, the rate of impacting ions is dramatically decreased due to emerging a new electrical field at these regions.

At low reactive admixtures, the poisoning process is not much pronounced (*metallic mode* of sputtering) but increasing the flux of reactive species accelerates the poisoning process. Consequently, the sputtering rate is decreased by increasing the poisoned area. Eventually, the discharge is almost quenched when the poisoned regions completely cover the target surface (*ceramic mode* of sputtering). Growing poisoned area, even at constant reactive gas flow, results in a similar mode transition of sputtering. This phenomenon is reversible. Decreasing the reactive gas flow makes a possibility to clean the poisoned area gradually. Whenever the reactive gas flow reaches zero (or sufficiently low value) the metallic mode will recover. Since the reverse process does not follow through the route of direct process, the evolution of the sputtering rate versus reactive gas flux, in a complete cycle, reveals a hysteresis curve (Figure 1.2). To avoid the mode transition in the presence of reactive gas, using pulsed DC power is developed as a powerful solution. This technique will be discussed in the next sections.

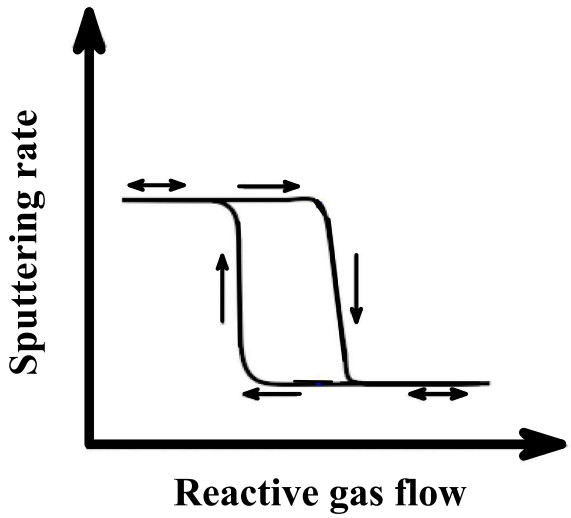

Figure 1.2: *A scheme of hysteresis behavior of sputtering rate with increasing and then decreasing the reactive gas flux in a reactive magnetron sputtering.*

1.3 Gas phase nanoparticle generation

Particle formation by gas phase routes can perform by homogeneous nucleation and also by coagulation of collided seeds. The thermodynamics and kinetics of the system specify the preferred growing mechanism. The Kelvin diameter gives a criterion to determine the growing path of NPs [4]. This critical diameter is a function of the surface tension of the NP, the saturation ratio, the temperature and the molecular volume of the NP. If the diameter of a single molecule is much bigger than its critical diameter, the nucleus is stable and coagulation is the dominant growth mechanism [4].

Due to small critical diameters in comparison to the molecular diameters, ceramics are good examples for considering the coagulation mechanism. According to the classical coagulation theory, the full coalescence can happen only at sufficiently high temperature. Furthermore, depending on agglomeration conditions the resulted particles by this mechanism can have certain shape or fractal like shape. When the primary particles strongly agglomerate together (*hard agglomeration*) the resulted NPs are spherical, while at *soft agglomerates* the interparticle forces are mostly van der Waals forces and the resulted NPs have a fractal shape [4].

When the NP is not stable, due to its small size, homogeneous nucleation mechanism will govern the growth process. Metals mostly follow the homogeneous nucleation (and growth) in the preliminary steps of the clustering process [23, 24]. In this work, metal and oxide metal NPs are generated based on homogeneous nucleation in a GAS. In the next section, we overview a simple model (presented for the NP formation in a GAS) to clarify the physics beyond the nucleation and growth of NPs in the used system.

1.4 Nanoparticle formation in a gas condensation source

The vapor phase of material provided by physical method such as heating the target, laser ablation and discharge sputtering, can be transferred rapidly to supersaturated vapor by cooling and then forming the cluster embryos through homogeneous nucleation.

We utilized magnetron sputtering to produce vaporized metal atoms (and oxide metal molecules) from a target in a GAS. In the case of presence of reactive admixture gas (such as nitrogen and oxygen) in the volume, a chemical reaction between the evaporated atoms and reactive gas species is the first step in the NP formation process [4], otherwise the free atoms in the volume themselves are main constitutes for nucleation and growth processes.

Increasing the concentration of free sputtered species in the volume of the GAS can exceed the saturation vapor density and then start the nucleation process in the vapor. The nucleation in the background gas initiates by three-body collision between two free species (denoted by M) and a buffer gas atom (denoted by A) to form dimer molecules from free sputtered species [25]:

$$M + M + A \rightarrow M_2 + A \tag{1.1}$$

This dimer molecule serves as a nucleus center and can grow through attachment individual free species in the volume. According to the literatures [25], the constant rates of three-body process for titanium and silver atoms are 2.5×10^{-33} $\mathrm{cm^6 s^{-1}}$ and 5.5×10^{-33} $\mathrm{cm^6 s^{-1}}$, respectively. Presence of buffer gas atom in three-body process is needed for momentum equilibrium and also to dissipate the thermal energy released during the bonding process.

According to the liquid drop model, the NP nucleus and also small NPs containing of n species, can grow up in the supersaturated vapor by attachments of free species [26]:

$$M_n + M \rightarrow M_{n+1} \tag{1.2}$$

The rate of NP growth in this regime depends on the size of NP and can be expressed as [26]:

$$k_n = k_0 n^{2/3}, k_0 = \pi r_W^2 \sqrt{8T/\pi m} \tag{1.3}$$

Where, r_W denote the Wigner-Seitz radius of the NP. Also, T and m are temperature and mass of seeds, respectively. The r_W values for titanium and silver are 1.67 ^{0}A and 1.66 ^{0}A, respectively. At T=1000 K, these values propose k_0=$3.3 \times 10^{-11} \mathrm{cm^3 s^{-1}}$ for titanium and k_0=$2.2 \times 10^{-11} \mathrm{cm^3 s^{-1}}$ for silver [18].

As it is clear, the nucleation and preliminary growth of NPs consume free individual species in the volume. Furthermore, the rate of nucleation (through three-body collision) is slower than the rate of NP growth. This causes the mean size of NPs to grow in the volume. With some mathematical calculations, which can be found in literature [25–27], the mean size of the formed NPs ($\overline{n}$), the size of largest formed NP ($n_{\max}$) and the number density of produced NPs (N_{NPs}) at the end of nucleation and growth processes in the supersaturation vapor can be expressed as following:

$$\overline{n} = 0.31(\frac{k_0}{KN_a})^{3/4} \tag{1.4}$$

$$n_{\max} = 1.2(\frac{k_0}{KN_a})^{3/4} \tag{1.5}$$

$$N_{\mathrm{NPs}} = 3.2N(\frac{k_0}{KN_a})^{-3/4} \tag{1.6}$$

Where, N is the initial number density of the sputtered species participated in clustering process and N_a denotes the number density of buffer gas atoms. The rate of three-body process is also shown by K. As it is clear, the ratio of the rate of nucleation through three-body process to the rate of attachment of individual free species to the small NPs, is the main factor of all above parameters.

At the end of the above process, the formed NPs are quite stable and the number density of the NPs is significantly high. However, the number density of seeds (the free sputtered species) is lower than that of supersaturation vapor. If the number density of the NPs in the volume is sufficiently high, the NP growth can continue with a coalescence process. The latter process can be represented as:

$$M_n + M_p \rightarrow M_{\mathrm{n+P}} \tag{1.7}$$

At this regime, due to adding large particles, the growth rate of NPs is more pronounced compared with that in the previous regime. Furthermore, by decreasing the number density of NPs during this process, bigger NPs can be formed.

In this thesis, a home constructed gas aggregation chamber is used to produce metal NPs from silver target and also oxide metal NPs from titanium target. For this purpose, the GAS is combined with a magnetron discharge operated in DC and/or pulsed DC regimes. Argon is used as working gas, while in the case of reactive sputtering a small admixture of oxygen as reactive gas was added. The GAS involves a stainless steel cylindrical chamber

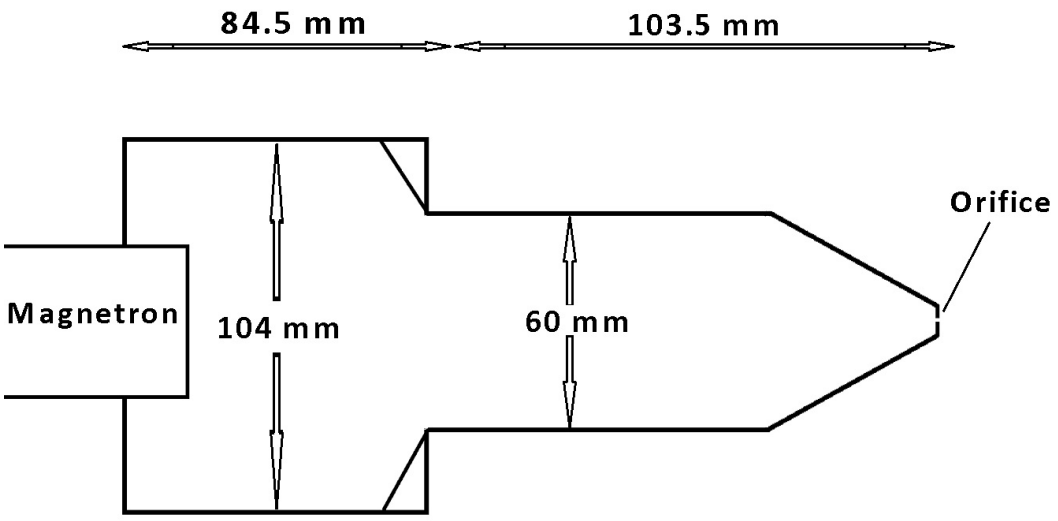

Figure 1.3: *A scheme of our home constructed GAS with different dimensions used in this dissertation. It made of stainless steel and connected to the deposition chamber via 3 mm orifice.*

with 104 mm in diameter and 84.5 mm in length. An extra cylinder with cone shape head placed on the top with a 3 mm orifice at the end, where it was connected to a deposition chamber. No separate pumping system is employed for the GAS and it pumps down through the pumping system of the deposition chamber. The magnetron system is installed in the bottom of the GAS as the total distance between the target surface and the orifice was about 188 mm. Neither a water cooling system, nor a liquid nitrogen cooling system was integrated with the GAS. Only in the case of titanium, a fan is used for air cooling to the room temperature. A schematic drawing of the used GAS is shown in Figure 1.3. Due to the important role of the dimensions of the GAS on the clustering process, these are also mentioned in the scheme.

1.5 Possible scenarios for oxygen in a GAS

As already discussed, the reactive admixtures play an important role in excitation and control of different mechanisms in the aggregation chamber during sputtering and clustering processes. Therefore, considering the role of reactive species in different possibilities is very instructive. Particularly in the current research, understanding the channels of oxygen consumption in the applied system is of interest.

When the oxygen is injected into the GAS, it starts to diffuse into the volume. During this process, some of oxygen species can meet the sputtered atoms and bond to them. These oxidized species (metal oxide molecules) are the main constitutes for nucleation and growth of NPs in the GAS. The rate of oxygen consumption by free sputtered atoms depends on the concentration of oxygen species, the density of free sputtered atoms and specially the diffusion rate in the buffer gas. Furthermore, the flux of oxygen, the working pressure

and the temperature are considered as important parameters which can indirectly influence on the rate of oxygen-sputtered atom reactions. The non-reacted oxygen particles in the above mentioned mechanism can reach the walls and also the target surface. Those oxygen particles that reach the walls, can be bound by the available metal atoms on the GAS walls through chemical reactions or stick to the walls individually. Furthermore, the arrived oxygen particles on the target can react with upper atoms of the target surface and poison the target by forming a dielectric oxide layer on it. Finally, the remaining oxygen, which does not participate in the above processes, can escape from the GAS via the small orifice.

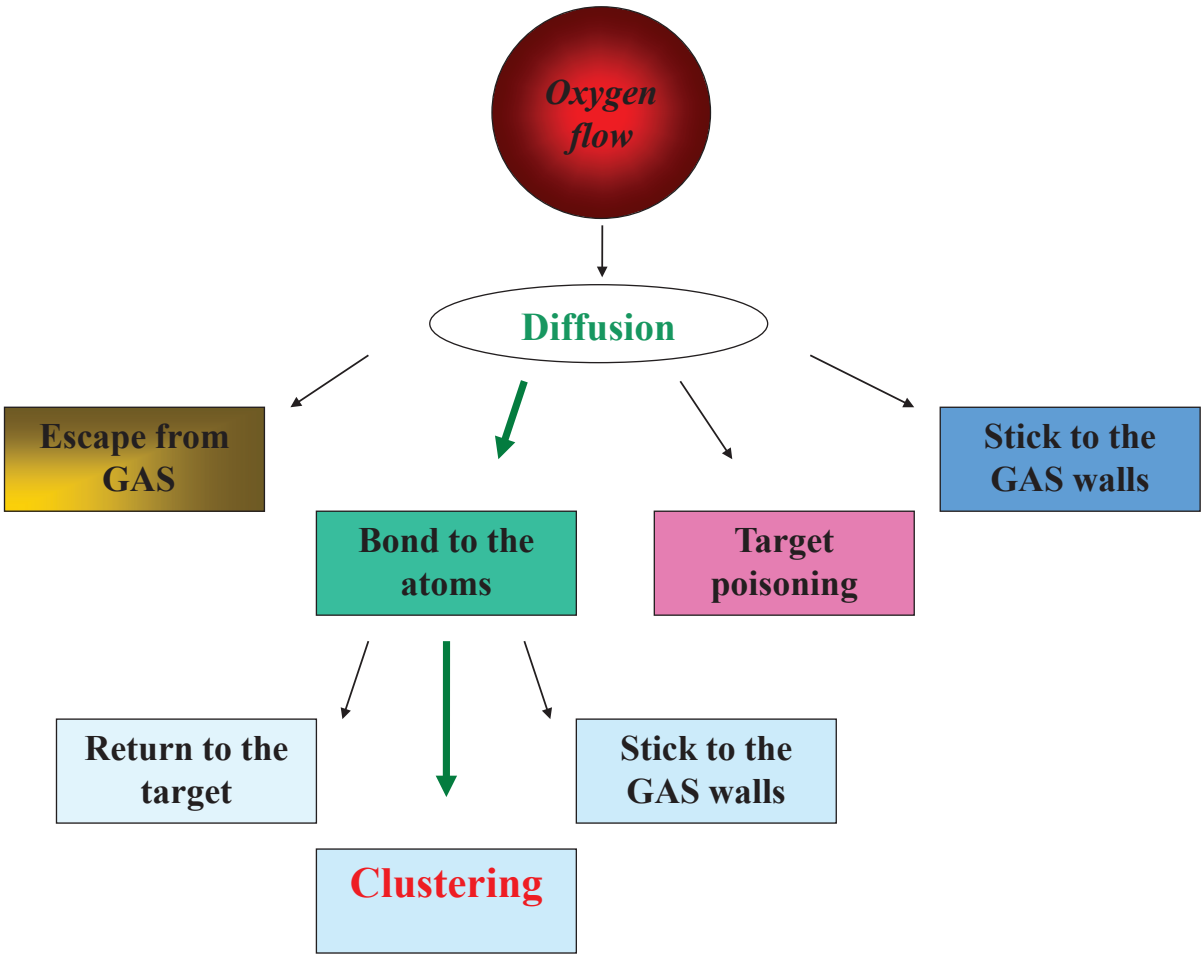

Figure 1.4: *A schematic chart of different possibility for oxygen consumption in the GAS. The green line is the favored route leading to the NP generation.*

The rate of oxygen consumption by each mechanism depends on how the oxygen is introduced into the GAS. Since in the used setup, the gases stream into the GAS from a narrow channel in vicinty of the the target (See Figure 1.1), the target poisoning process is more pronounced in a short period after oxygen injection.

A study on each possible scenario of oxygen consumption provides useful knowledge to understand the physics of processes in the GAS. As will be addressed in detail in the next chapters, the escaped oxygen from GAS can monitor by a mass spectrometer installed in

the deposition chamber. In-situ measurement of chemical composition of the formed NPs can give some information about the content of oxygen consumed in the clustering process. Furthermore, the evolution of bias voltage (of magnetron discharge) is proportional to the development of the poisoned regions on the target.

As will be seen, by measuring the evolution of parameters in different steps, a proper model for the NP generation can be extracted. Figure 1.4 displays a chart of possible scenarios for oxygen in a GAS. Although the highlighted green route is the desired scenario that leads to the NP generation, the optimized NP formation can be achieved only by controlling all scenarios.

1.6 Deposition chamber

A cylindrical vacuum chamber (deposition chamber) was the central part of the used setup for most of the experiments in this work, which was designed by S. Rehders. The diameter of the vacuum chamber was 250 mm and its length was 525 mm. This stainless steel chamber includes several flanges with different sizes. A picture of the used vacuum chamber is shown in Figure 1.5. More details of the applied setup will be presented in the next chapters.

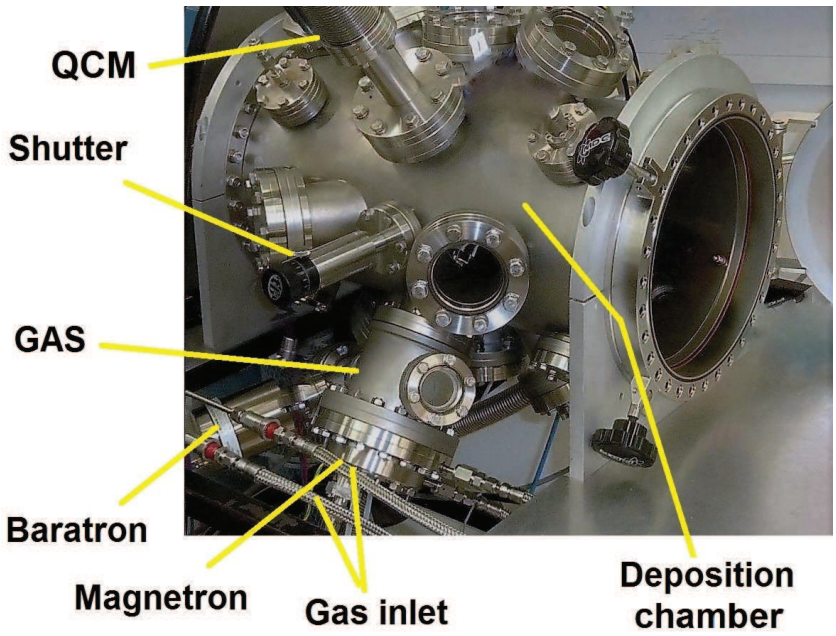

Figure 1.5: *A picture of the deposition chamber utilized in this research.*

1.7 Transition TiO_x nanoparticles by GAS

In this section, we investigate the TiO_x NP generation in a GAS by employing reactive magnetron sputtering. Previously, Marek and co-authors [11] have shown that using a small

oxygen admixture can significantly enhance the TiO_x NP generation by such a system.

For determining the influence of oxygen on the rate of TiO_x NP generation, a set of experiments was performed. The first experiment was started by adding 80 sccm argon to the GAS and running DC magnetron discharge at 50 W. Initially, a high flux of oxygen was added into the chamber which causes poisoned areas on the titanium target. Subsequently, by growing the formed isolator layer on the target, the mode of sputtering was transited from metallic to ceramic. As could be expected, by reducing the sputtering rate, no NP deposition was monitored at this regime. In the next step, the oxygen flow is gently decreased. Upon decreasing the oxygen flow, the target will switch to metallic, and below 0.050 sccm a small D.R. can be recorded (Figure 1.6). With decreasing oxygen flow, the NP deposition increases until an optimal oxygen flow was found about 0.01 sccm where the maximum D.R. of NPs is measured (Figure 1.6). Further decreasing in oxygen flow leads to a drop in the D.R. and without oxygen no deposition can be detected at all. The concentration of escaped oxygen from the GAS was also considered during the experiment by a mass spectrometer. As it is clear from Figure 1.6, at high oxygen flux and highly poisoned target, most of the oxygen is escaped from the GAS and the corresponding signal is much pronounced. Reducing the oxygen flow into the GAS and also consumption of more oxygen in the NP generation process, result in a weaker signal of the escaped oxygen [10].

In the next experiment, the evolution of the NPs generation was studied. The discharge was run at 40 W and pressure was fixed at 200 Pa by adding 115 sccm argon without any reactive gas. The chamber was pumped down to 10^{-5} Pa before starting this experiment. As shown in Figure 1.7, the D.R. is not stable and continuously decreases with time. Eventually, it reaches zero value after long term. Probably the water and carbon oxide in the walls of GAS and also the poisoned region on the target are the main sources of oxygen in the system. These chemical compounds can release oxygen during the sputtering process due to ion and electron bombardments. Consumption reactive species in the clustering process decreases the concentration of reactive species which leads to lower D.R.. Finally, the NP generation is stopped when the density of reactive species is negligible. Running the same experiment in a baked out system to 8×10^{-6} Pa before starting the sputtering, accelerates the evolution of the D.R.. In this condition, the D.R. of NPs is rapidly (in 2 min) reached zero level because the walls of the baked out chamber do not provide sufficient oxygen for the NP formation and just the poisoned regions on the target surface provides a weak source for a short time.

The above experiments suggest that oxygen binds with titanium atom and forms stable titanium oxide molecules. These molecules serve as nucleation centers for the growth of TiO_x NPs. In the case of the optimal (very low) oxygen concentration which yields the maximum D.R., the added oxygen is totally consumed by sputtered atoms in the gas phase and is not sufficient to switch the sputtering mode by highly oxidize the target. Using higher oxygen flow leads to an increasing oxidized area on the target. Subsequently, reducing the sputtering rate leads to a decreasing the NP formation due to less seeds coming from the target. In opposite direction, at lower oxygen flow, less D.R. will be resulted because less numbers of Ti atoms can bind with oxygen to make nucleation centers.

The observed behavior is dissimilar from that of noble metals like copper. Nobel

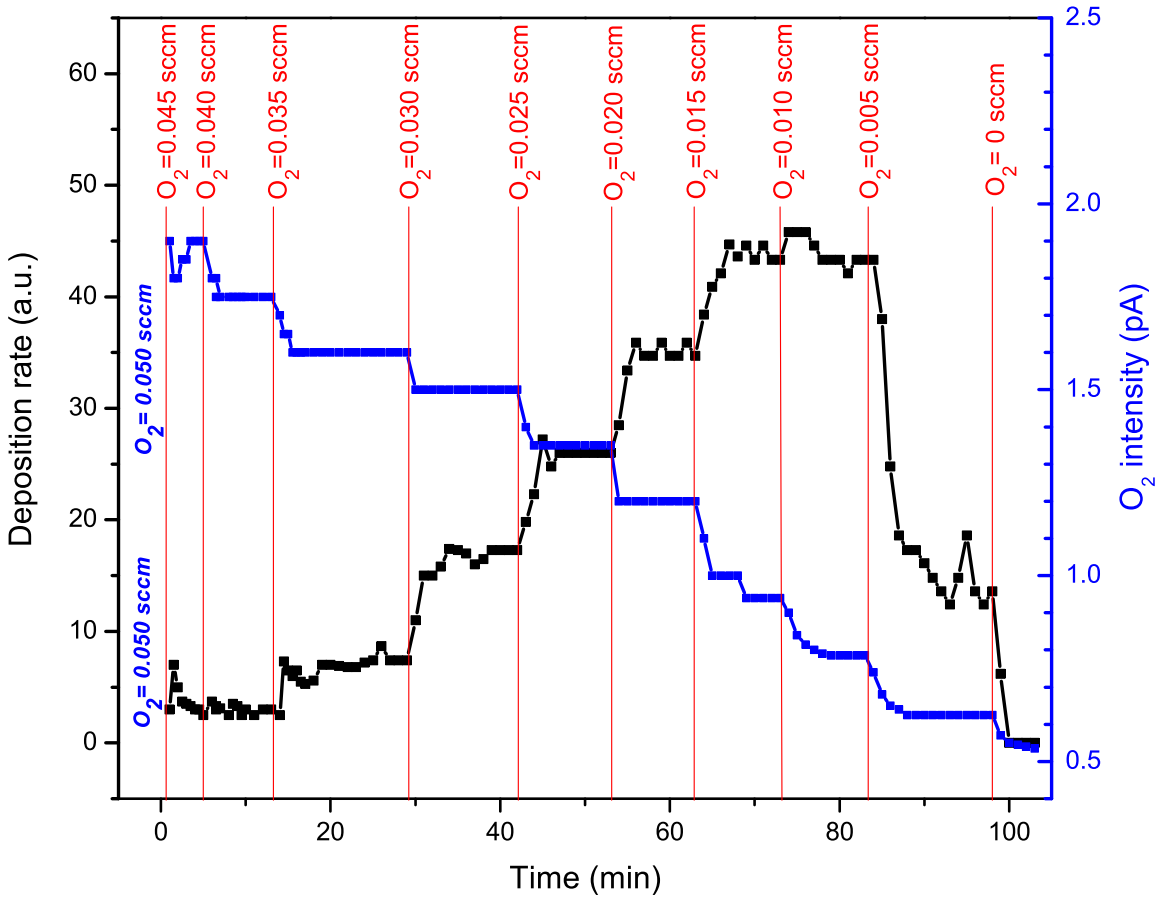

Figure 1.6: *Dependence of the NPs D.R. on the reactive gas flow for titanium with oxygen (argon flux 80 sccm, 150 Pa). The intensity of escaped oxygen (O_2, 32 amu) from GAS is shown as measured with a mass spectrometer [10].*

metals show a high D.R. without any reactive gases and the oxygen concentration has minor influence on the NP generation [11]. This difference can be explained by the diatomic binding energies and sputtering yields of the different materials. For instance, for a copper dimer the binding energy is 2.083 eV while for a copper-oxygen dimer it is 2.979 eV. In the case of titanium dimers this value is 1.219 eV and for titanium-oxygen dimers the binding energy is 6.908 eV [28]. Furthermore, the sputtering yields for copper and titanium are 1.3 and 0.3, respectively [29]. Therefore, in the absence of the reactive gases, copper builds more clusters than titanium, since the much larger sputtering yield provides more free metal atoms as seeds for stable cluster formation. However, with the addition of oxygen the situation is reversed, since the binding strength of titanium-oxygen is much higher than that for copper-oxygen, which results in very efficient generation of stable seeds of titanium NPs.

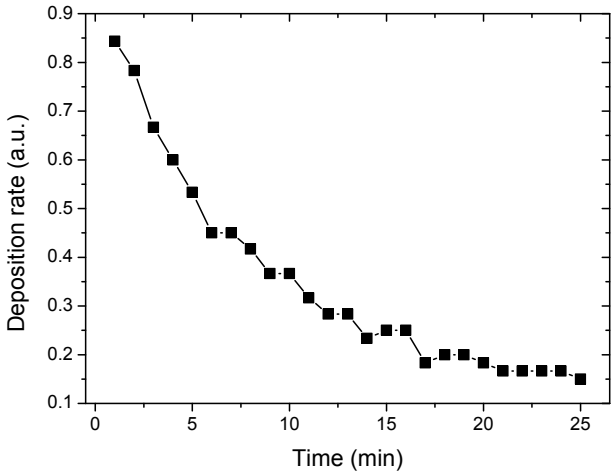

Figure 1.7: *The evolution of D.R. with time at constant discharge and gas parameters, for titanium. The experiment started directly after venting and then pumping the chamber, without baking it out [10].*

1.8 Nanoparticle generation by reactive pulsed DC sputtering

As mentioned in the previous sections, when a reactive gas is added to the magnetron discharge, a decrease in the sputtering rate will be observed due to forming a ceramic layer on the target. In this condition, the impacting ions to the poisoned area can not be discharged totally, and create a strong local electric field in the poisoned regions which prevents sputtering from those zones. Another possibility resulting from the presence of reactive admixture is *arc* discharge which can happen at high local electric fields. As a favorable solution for the above mentioned problems, the pulsed DC sputtering was developed. In this technique, a fixed voltage does not use to power the magnetron instead, the compressed power is delivered to the target in a short period called *time on* (t_{on}). In the next time period, called *time off* (t_{off}) or *reverse time*, the target is left at floating potential or is fed by small positive potential. This type of power feeding causes higher sputtering by neutralizing the charge of poisoned spots during t_{off} and subsequently, better target cleaning with presenting more effective power during t_{on}. Since the discharge is frequently switched between *on* and *off* modes, the plasma electrons have a chance to reach to the target and discharge the ions on the poisoned area during the reverse time [30]. Then in the next t_{on} period the high energetic ions, provided by compressed power, can sputter off the formed poisoned species on the target surface and increase the sputtering rate considerably.

The frequency of the pulse and the ratio of the t_{on} to the t_{off} (duty cycle) are crucial parameters in this technique. The frequency and duty cycle should be adjusted in a way that the electrons can neutral the total charge on the target. Furthermore, the strength of the delivering power at t_{on} period should be sufficient to remove the poisoned area on the target. For working in the *arc free* regime, using short t_{on} and long t_{off} is needed to avoid breakdown resulted by highly charged surface. Observing these conditions causes to neutral

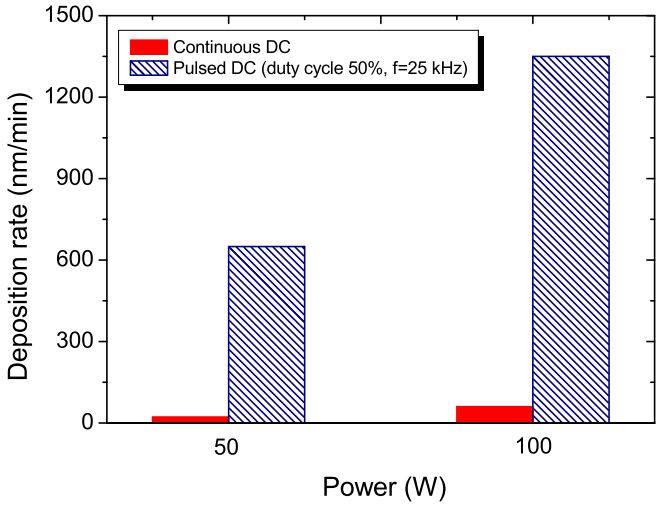

Figure 1.8: *The deposition rate of TiO_x NPs generated by a GAS in combination with continuous DC magnetron sputtering (solid fill) or pulsed DC magnetron sputtering (textured fill) systems. Measurements were performed for different powers (50 W and 100 W), while the argon pressure was fixed at 200 Pa with the optimal low amount of oxygen admixture [13].*

the surface charges and to prevent the charge accumulation after several periods [30].

In this dissertation, the magnetron discharge in pulsed DC regime was ignited by the DC power supply (MDX500) supported by a self-constructed pulsing unit employing a power MOSFET, powered by a function generator (PeakTech 4025). The magnetron was equipped with a Ti target and installed in the GAS. A small amount of oxygen admixture, as a reactive gas, was added to the GAS while argon was used as the working gas. The applied frequency was tuned in the range of 25 – 60 kHz and the duty cycle was adjusted in the range of 30 – 90 percent.

Preliminary experiments have shown very interesting results with a huge increase in the NP generation in comparison to the conventional DC sputtering [13]. In Figure 1.8, the maximum D.R.s of TiO_x NPs achieved by using a DC magnetron discharge (solid fill) and pulsed discharge (texture fill) are presented for two different powers (50W and 100 W). The frequency and the duty cycle of the pulsed DC power were fixed at 25 kHz and 50% respectively. For getting comparable results, the target was cleaned in argon discharge prior to each experiment. It is clear from Figure 1.8 that the difference in the rate of NP generation by two techniques is more than one order of magnitude.

Forming sub-oxide compounds on the target during the t_{off} periods and sputtering during the t_{on} periods can explain above observation. With this scheme the NP generation is accelerated because the sputtered compounds can directly participate in the nucleation and growth processes of NPs, while in the DC regime, the sputtered pure Ti atoms should be initially oxidized in the volume and then serve as seeds. Varying the t_{off} at constant t_{on} by playing with duty cycle and frequency and also study the evolution of the D.R. of NPs by

effective power at different oxygen admixtures demonstrated that the NP formation at the pulsed DC regime strongly depends on the pulsing parameters and the content of reactive admixture [13].

The stabilized NP formation at the pulsed DC regime is another challenge which is not considered in preliminary experiments, but will be discussed in chapter 3. There, it will be seen that the stabilized NP generation can be achieved only at certain values of the pulsing parameters at fixed operation conditions.

1.9 Hollow electrode plasma for material processing

Next part of this dissertation is devoted to processing metal NPs by an RF discharge. Since the employed hollow electrode discharge reveals the hollow cathode effect at RF regime (see chapter 4), it will be instructive to review the concepts of the hollow cathode discharge. Furthermore, to understand the observed phenomena at such an environment and also to investigate the mutual interaction between the RF plasma and NPs, it is helpful to look at the plasma characterization techniques in the RF regime. In the following, we briefly review the hollow cathode effect and some aspects of characterizations of the RF discharge.

1.9.1 Hollow cathode discharge

The name of *hollow cathode discharge* (HCD) usually refers to any discharge in a cathode with cavity geometry. In such a system the discharge is mostly bounded by the walls at the cathode potential. The HCD develops as the distance between the cathode surfaces is reduced at constant gas pressure and power. Due to the geometry of the HCD, the loss of electrons is dramatically reduced. Furthermore, in the HCD the negative glow region can occupy most of the interior volume of the cathode, in which the concentration of fast electrons is much higher than that of lasers [31]. Owing to this unique intrinsic advantage, a great deal of time and effort has been expended on the study of DC hollow cathode discharges. Expansion of the negative glow causes the plasma current increases by a factor 100 to 1000 at same plasma voltage. In general, the hollow cathode systems can be classified as the hot and cold cathode versions [32]. A hot cathode surface in contact with the plasma can provide a very important source of electrons (via thermal-field emission) and strongly influences the characteristics of the plasma.

As using the magnetic fields in a magnetron discharge system results in an increase in the plasma density [33], the electron trapping by the geometry of the cathode discharge also causes a higher plasma density in a hollow cathode system [34]. The HCD effect is well interpreted by the presence of high energy pendulum electrons in the discharge volume. These electrons are reflected from the sheaths of the cathode. The long path of each trapped electron is known to generate a large number of secondary electrons, which resulting to the high electron density and high plasma current. Furthermore, the electrons can escape from the plasma only along the axis of the cathode. Thus, the electron loss rate in an HCD is

less than for an equivalent parallel plate discharge which enhances the plasma density in an HCD.

Low electron energy loss during elastic collisions between electrons and ions (or neutrals) is another advantage of the hollow cathode configuration. During the elastic collisions between electrons and ions (or neutrals), the change of electron momentum is often large. In HCDs, the average electron energy is in the range of 1-5 eV. This range of electron energy introduces a high electron–ion collision cross section. Furthermore, when the degree of ionization is rather high (more than 10%), the interactions between electrons and ions is the dominant mechanism of the elastic collision processes. As has been shown in Ref. [33], at typical conditions, the average energy loss of an electron in an elastic collision with an ion (or neutral) is in order 10^{-4} of the electron energy which is negligible. More information on the physics of HCD and the applications of HCD systems in different fields can be found in a comprehensive review, which has been recently published by Muhl and Peretz [32].

F. Paschen reported in 1916 [35] on a hallow cathode configuration which was capable to produce a discharge with high electron density and low ion (and neutral) temperature. Later on, the RF glow discharge technology, has been developed to meet various requirements of industrial applications as well as scientific researches [31, 32]. Boswell in 1984 [36], by developing a method has shown that in a typical RF glow discharge an ionization close to 100% is achievable at very low power flux. Exciting hollow discharge in the radio frequency regime, offers an interesting and versatile system for a wide range of materials (included polymers) processing and deposition [37, 38] as well as large area surface treatment [39]. It also provides a suitable environment for deposition semiconductor functional films [40].

1.9.2 Plasma characterization at RF regime

Generation of several harmonics of the original frequency in the discharge is one of the difficulties for plasmas driven at RF regime which results in nonlinearity in characterizations. However, even more important is that the RF oscillations across the sheath of Langmuir probe disturb the obtained characteristics by shifting the I-V trace negatively [41]. Eliminating these fluctuations by using a passive probe [42], which is a single probe supported by an external circuit including several chokes (LC filters), is a beneficial solution. As well, compensation of distortions by applying an active probe [43], is another technical possibility to avoid this problem. In an active probe, the probe is connected to an RF signal matched to the plasma oscillations (in amplitude and phase), preferably including the harmonic oscillations.

Using electronegative constituent, e.g. oxygen, changes the plasma parameters by introducing negative ions to the electropositive plasma. These reactive species can be used as a controlling factor of the plasma parameters. The negative ions in the discharge not only can change the plasma potential and plasma density, but also influence on the energy dissipation process in plasma by launching new mechanisms through interaction with other plasma species. For instance, in the etching process by CF_4, scaling the added oxygen controls the releasing fluorine atoms and then the rate of silicon etching as well [44]. Furthermore, in

plasma polymerization, the vital role of electronegative constituents to remove undesired components and radicals from the plasma environment has been proven [45].

As will be discussed in chapter 4, a small hollow electrode with special geometry was constructed to support our aim to modify the metal NPs at the low pressures regime. To characterize the ignited plasma, a passive probe technique with four chokes is used to remove the first two harmonics. As well, a conventional Langmuir probe is also employed to get plasma parameters from electrostatic characterization. Our findings demonstrate that the potential oscillations of the plasma at RF regime are negligible in comparison to the electron thermal energy.

1.9.3 Charging nanoparticles in plasma

The charge of a dust grain in plasma and fluxes of plasma species onto the particle have been the subject of investigation in the context of rapidly developing dusty plasma research [46]. However, in the case of a nanometer sized particle in plasma, it is necessary to take into account some specifications. The electron and ion capture cross sections of a charged grain with a size less than the Debye length differ from its geometrical cross section. Furthermore, grains in a hot plasma intensely evaporate; however, in contrast to dust grains, NPs are not screened by the vapor because their dimensions are smaller than the electron and ion mean free path lengths. Additionally, the thermionic current from a hot NP is not limited by the space charge of electron flows, as is in the case of dust grains [47, 48].

To study the properties of NPs in plasma, it is necessary to self consistently calculate the energy and charge fluxes onto NP. Note that the particle charge is determined not only by the rate of absorbed charged species by the grain, but also those emitted from it [27, 47, 49]. Charge fluxes from a grain can be caused by secondary electron emission, ion induced electron emission, photoemission, and thermionic emission [49]. As Martynenko et al. [50] have shown, thermal radiation from a grain with a size less than 100 nm is negligible. Hence, thermal radiation from NP can be ignored.

Due to the high mobility of electrons and slower energy exchange with ions and atoms, the electron temperature (T_e) is higher than the ion temperature, so that electrons can heat NPs more effectively. If NP is heated to the temperature at which thermionic emission comes into play, then the NP potential, which is negative in the absence of thermionic emission, begins to grow and may become positive. This leads to an additional electron flux toward the NP and its extra heating. This process can explain the phase transition of NPs from amorphous to fully crystalline when the residence time in the plasma volume is sufficiently high [51].

As will be demonstrated in chapter 5, at low power discharge, most of the silver NPs are negatively charged by collecting electrons from the hollow electrode plasma. Elevating the electron temperature by power, leads to more positively charged NPs which indicates more effective thermionic emission from NPs at higher electron temperature.

1.10 Semiconductor nanoparticles by nonthermal plasmas

Nonthermal plasmas are typical discharges characterized by hot electrons and low temperature ions. The electron temperature in these plasmas is in the range of 20000 to 50 000 K (2-5 eV) while the temperatures of ions and neutrals remain around the room temperature [14]. Nonthermal plasmas can host the synthesis of crystal NPs. In this application, energetic electrons can effectively dissociate the molecules of a precursor and produce the seeds for the nucleation and growth of NPs in the plasma environment. This technique is much interested to form NCs from non-toxic elements whose have high crystallization temperatures such as group IV elements (particularly Silicon (Si) and Germanium (Ge)). The crystalline structure of NPs is indispensable for application in optical and electronic devices because the high density of defects in amorphous particles creates high charge trap states which are harmful for desired properties of nanomaterials [52].

The size of semiconductor NCs is almost considered as a vital parameter which influences on optical band gap [15], melting point temperature [53], crystallinity point temperature [54] and hardness [55] of NCs.

Semiconductor nanocrystals have received significant attention in recent years due to their size-dependent optical and electronic properties. Most of the attention given to Si NCs, due to their efficient and tunable light emission [56, 57]. However, Ge NCs may be more interesting than Si NCs for device applications that require a small band gap material, a material that exhibits stronger quantum confinement than Si, or a material that absorbs light better than Si.

The governing mechanisms of the NP generation in nonthermal plasma are very different from those in supersaturation vapor technique. As already shown, the classical homogeneous nucleation theory strongly depends on forming supersaturated vapor from the NP seeds, while in nonthermal plasmas, the chemical clustering process is dominant. The reaction between chemical species is the key point in this technique. Since the species in the volume are different for different materials, a general statement about the NP synthesis in plasmas is difficult [14]. Synthesis of Si NP is the most widely investigated system in nonthermal discharges. In spite of presenting several models for Si NP formation, the corresponding mechanisms are not completely understood because the applied operation conditions such as pressure and discharge power play important roles in the nucleation and growth processes. As well, the utilized gases and precursor have outstanding roles in the dominant mechanisms of the synthesis process. Looking at the reported works which concerned the Si NP generation, might be instructive to get better insight about the clustering process in nonthermal plasmas.

Silane (SiH_4) is almost the favor precursor used to form Si NPs in plasma [14]. According to the model presented by Howling and co-authors [58, 59], small silane clusters (Si_nH_m) play a significant role in the NP growth process. These small particles have positive electron affinities and thus can be negatively charged by collecting electrons from the nonthermal

plasma [60]. As they have shown by mass spectroscopy measurements, negative clusters can be trapped in the bulk plasma and act as nucleation centers, while the positive species and neutrals diffuse to the walls. Therefore, only the trapped anionic particles have big chance to grow in the plasma volume and have a main contribution in the Si NP formation. Later, Gallagher et al. [61,62] by developing a model for clustering in plasma, demonstrated that forming negative silyl radicals through electron attachment to SiH_3 is one of the main factors for the cluster nucleation in plasma. Considering several hundreds of possible chemical reactions in a silane plasma by presenting a chemical kinetics model [63, 64] revealed that negative silyl (Si_nH_{2n+1}) and negative silylene (Si_nH_{2n}) species provide two channels for Si clustering. Watanabe [65] in a comprehensive report has shown that the governing mechanism of the NP growth process depends on the time scale of the particle growth and the residence time. If the residence time of neutrals is longer than the cluster growth time scale, the negative species have no important role in the clustering process and the dominant growth mechanism is determined by short time radicals generated by neutral species in plasma. When the time scale of the cluster growth is longer than the residence time of neutrals, the negative species have the most important role in the clustering process.

In spite of lacking a general model for clustering in nonthermal plasmas, this technique is frequently applied to generate NPs for using in advanced materials because nonthermal plasmas provide unique environments to produce NCs with precisely defined properties. Particles can be unipolarly charged in a nonthermal plasma volume. The existence of the hot electrons with much more mobility in comparison to the slow species causes the NPs to be negatively charged with collecting electrons from the discharge [66]. The unipolar NPs decelerate agglomeration and flocculation processes in the plasma volume [67]. Consequently, a very narrow size distribution of the NPs can be obtained by this technique. Additionally, fast diffusion of the hot electrons towards plasma walls creates a strong ambipolar potential in the discharge. This can confine the negatively charged particles in the plasma and increase the material yield by reducing diffusion losses of the NPs. Furthermore, the high rate of electron-ion recombinations on the surface of the NPs in a nonthermal plasma accelerates the particle heating process. This elevates the NPs temperature to considerably higher temperatures than background gas, which can cause a phase change in NPs, from amorphous to crystal structure [14, 68].

Finding of precursors to grow compound NCs is a challenge of this technique due to generation unwanted byproducts. Also, the collected NCs as powder do not disperse into solution as produced, because the van der Waals attraction causes agglomeration and flocculation. This problem can be solved by attaching long alkyl groups to the surface of NCs [57,69]. Furthermore, indirect band gaps of semiconductor NCs require that photon emission and absorption processes involve a momentum balancing phonon (lattice vibration), a fact that puts these processes at a disadvantage compared to their nonradiative competition and disqualifies bulk semiconductors as suitable materials for host of optoelectronic devices [16]. A variety of strategies were developed to remediate this deficiency, including doping, alloying, and hybrid structures with other direct band gap semiconductors [70].

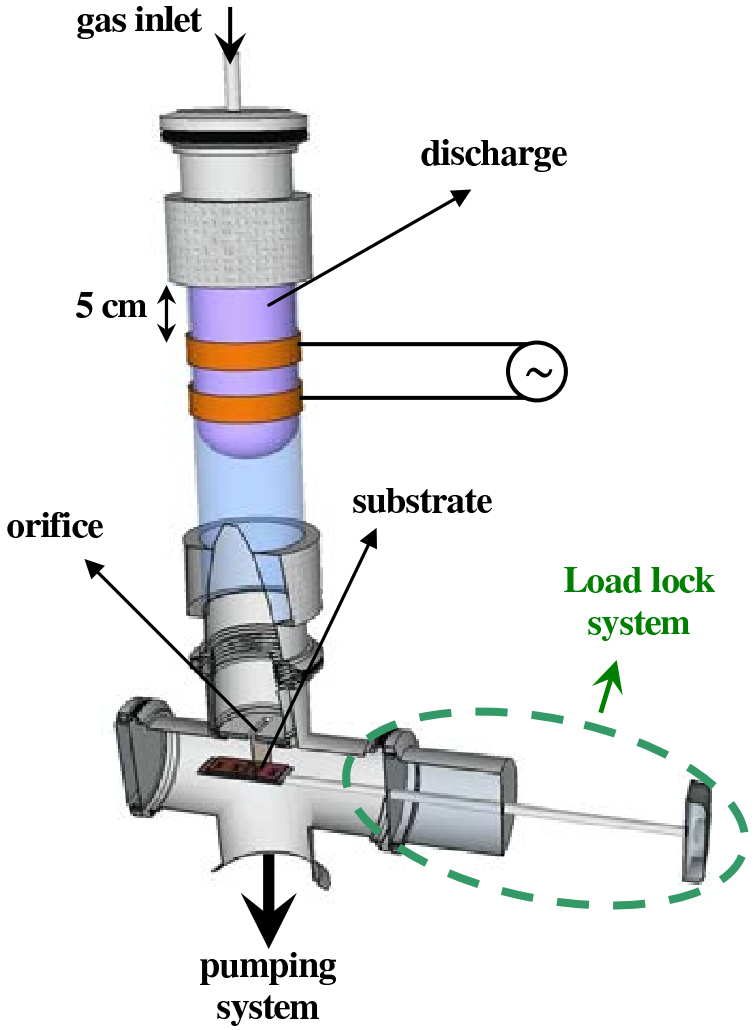

Figure 1.9: *Scheme of the used experimental setup for Ge NPs production by nonthermal plasma technique.*

In this dissertation, nonthermal plasmas are employed to produce freestanding Ge NPs. We used germanium tetrachloride ($GeCl_4$) as precursor to synthesize the Ge NPs in the argon – hydrogen discharges. The applied setup is sketched in Figure 1.9. The mixture of gases and precursor inject to a quartz plasma reactor from top inlet. The nonthermal plasma was ignited by two wrapped copper rings powered by an RF power supply through a matching network. The synthesized Ge NPs are collected in downstream and transfer to the oxygen free glove box for further characterizations by a load lock system. In principle, hydrogen admixture is used to scavenge the free chlorine in the plasma volume, which are released during dissociation of $GeCl_4$ by energetic electrons. As will be discussed in chapter 6, the content of hydrogen admixture also plays a very important role in the NP synthesis process by adjusting the plasma chemistry. We demonstrate that the physical properties and surface chemistry of NPs can be tuned by controlling the hydrogen concentration in the plasma volume.

1.11 Characterization methods

1.11.1 X-Ray diffraction (XRD)

To identify the crystal status of materials, using *X-ray diffraction* (XRD) method is known as a powerful technique for a wide range of materials. An XRD device is working based on interference laws of diffracted X-ray waves from the materials. In most cases, the specimen is irradiated by a specific X-ray while the incidence angle is fixed. An interference pattern can be produced by recording the intensity of diffracted beams in any directions. In crystal materials the diffracted beams coming from the ordered atomic planes create special interference patterns. One can deduce the crystal structure of the sample by analysis the obtained interference pattern based on Bragg equation [71]. Furthermore, the size of NCs can be extracted from the obtained data by using the *Scherrer* equation to fit the diffracted pattern [72]. The Scherrer equation relates the size of NC to the broadening of a peak in XRD pattern. It is formulated as below:

$$d = \frac{K\lambda}{\beta \cos\theta} \tag{1.8}$$

Where d in the left side of equation shows the size of NC. λ denotes the X-ray wavelength and β is the FWHM (Full Width of Half Maximum). Furthermore, θ is the Bragg angle and K shows a dimensionless shape factor. Using this equation is limited to the crystal particles smaller than 200 nm size.

In this thesis for the study of the crystallinity of NPs, a thick layer of NPs deposited on a glass substrate was investigated using a Bruker–AXS microdiffractometer with a 2.2 kW sealed Cu X-ray source. Furthermore, the sizes of NPs calculated by Scherrer equation using Jade 8.0 software, are well corroborated with the sizes obtained by TEM measurements.

1.11.2 X-ray photoelectron spectroscopy (XPS)

X-ray photoelectron spectroscopy (XPS) is a technique which has been used here to characterize the chemical composition of NPs films. This technique is applied to determine the elemental composition, empirical formula and chemical oxidation state of the elements in a sample. The XPS instruments work based on measuring the kinetic energy of electrons emitted from material by a characteristic X-ray irradiation. The obtained data allow to determine the characteristic of binding energies. This method can provide the information from top surface chemistry of materials (up to 10 nm in depth) because only the photo emitted electrons originated from that region can leave the material without energy loss due to inelastic collisions. Furthermore, XPS measurements must be performed under ultra high vacuum (UHV) conditions because electron detectors are far away from the material irradiated with X-rays.

In this research, an Omicron XPS operating with an Al anode at a power of 240 W was used to measure the chemical composition of TiO_x NPs thin film directly after preparation. To this aim, the GAS was connected to the transfer chamber of the XPS apparatus. The TiO_x NPs were deposited on a carbon coated silicon substrate and subsequently the sample was transferred to the real site for in-situ measurement.

1.11.3 Quartz crystal microbalance (QCM)

A *quartz crystal microbalance* (QCM) is a powerful in-situ measuring tool to monitor the thickness of deposit material. It consists of a quartz crystal which follows the piezoelectric behavior. It can measure mass per unit area by varying the frequency of the quartz crystal resonator. The oscillation frequency of the used crystal depends to its thickness. Therefore, material deposition on the quartz crystal decreases its oscillation frequency. When the deposited mass is small in comparison to the quartz plate mass, one can precisely find the content of the deposited mass from the frequency change, applying the Sauerbrey equation [73].

According to the Sauerbrey equation, the frequency change Δf (Hz) of a piezoelectric due to mass change of Δm (gr) can be calculated as:

$$\Delta f = -\Delta m(\frac{2f_0^2}{A\sqrt{\rho_q \mu_q}}) \tag{1.9}$$

Where f_0 and A denote the resonant frequency and active crystal area, respectively. ρ_q is the density of quartz (ρ_q= 2.648 g/cm^3) and μ_q is the shear modulus of quartz for AT-cut crystal (μ_q= $2.947\times10^{11} g/cms^2$).

In this work, we utilized a STM-100 / MF QCM to monitor the deposition rate of NP beams. The initial resonant frequency of the applied quartz crystal was 5 MHz. Due to the thermal sensitivity of the quartz frequency, the unit was equipped with a water cooling system to keep the working temperature constant [22].

1.11.4 Transmission Electron Microscope (TEM)

Transmission Electron Microscope (TEM) is an important instrument for exploring quantitative structural and crystallographic information of materials. Herein, for analysis the morphology and crystal status of the NPs, we prepared sub-monolayer samples by collecting particles on carbon coated copper grids. Then the films were transferred to the TEM apparatus for imaging.

Two types of TEM devices at different resolutions were employed to study the prepared specimens of this work: A FEI Tecnai F30 G2 (FEG, 300 kV) operating in scanning mode with a high-angle annular dark-field detector (HAADF-STEM) was used by

Dr.U.Schürmann, from the chair of synthesis and real structure. Furthermore, a JEM-2100 (JEOL, 200 kV, LaB6) operating in the bright field mode was utilized by A. Hinz, from the chair of Multicomponent materials, to make images. In the last step, the resulted images were manually analyzed using Solarius software to deduce the size distribution of the NPs.

1.11.5 Scanning Electron Microscope (SEM)

To study the topography of the materials the electron microscopy is a versatile technique which employs electron beams to probe the surfaces. A *scanning electron microscope* (SEM) is a kind of electron microscope, which frequently used to investigate the morphology and topography of the samples.

In the current, work a Supra 55VP SEM, provided by Zeiss company, was used to study the morphology of the TiO_x NPs film. For this aim, a sub-monolayer of NPs was collected on a silicon substrate at desired conditions. Then the SEM images of the prepared sample were taken by Dr. Vladimir Zaporojtchenko from the chair of multicomponent materials. Eventually, the size distribution of the NPs was extracted by analysis the images using Solarius software.

1.11.6 Quadrupole Mass Spectrometer (QMS)

Quadrupole mass spectrometer (QMS) is a typical mass analyzer. We used a Balzers Prisma QMS-QME200 which consists of a cathode, a quadrupole and a detector. The quadrupole includes four aligned metal rods with square cross section while the opposing rods are electrically connected together. The quadrupole responses to filter the passing ions according to their mass to charge ratio. The incoming species are ionized with a hot cathode placed before the quadrupole. This apparatus is also equipped with a Channeltron/Faraday detector positioned beyond the quadrupole to count arriving species.

Since the QMS works at lower pressure regime compared with our operating pressures, it was installed in a separate chamber to allow differential pumping by a turbo molecular pump (Pfeiffer HiPace80). The chamber of the QMS was connected to the main chamber via a tube and a variable valve to control the incoming particle concentration and survive the right pressure in the QMS chamber. The employed QMS works in the range of $0 - 100$ amu, hence, we had no chance to test the concentration of NPs. However, as will be discussed in chapter 2 and chapter 3, the QMS was adjusted to measure the concentration of oxygen (32 amu) and argon (40 amu) during our experiments.

1.11.7 Fourier Transform Infrared Spectroscopy (FTIR)

Fourier transform infrared spectroscopy (FTIR) is a powerful technique to study the chemical structure of material at different phases based on interferometry concepts. The Michelson

interferometer is used in such apparatus to produce various patterns from sample at different wavelengths in the IR regime. In principal, the obtained raw data need to be converted to the actual spectrum by using the Fourier transform. This conversion is usually performed by applying a proper software. Therefore, the real spectrum with different band peaks corresponding to the various vibrational bonds will be presented by the applied software.

In this dissertation, we applied a Bruker Alpha FTIR spectrometer operated in the reflectance mode. For data analysis OPUS software was used. Furthermore, the spectra were collected by averaging 20 scans at 2 cm^{-1} resolution. To avoid any changes in the chemical surface structure of NPs, this device was installed in a N_2 purged glove box.

1.11.8 Langmuir probe

A *Langmuir probe* is a tool to determine the basic properties of plasmas such as the electron temperature, the electron density and the plasma potential. Due to simplicity, cheapness, adaptability to any systems and also the possibility of spatially resolved measurement of plasma parameters with good resolution in the wide rage of plasma density, it is frequently employed to characterize different discharge configurations [74]. There are so many types of Langmuir probe, which are improved for different plasmas with typical specifications. A single Langmuir probe consists a small tip (mostly a piece of tungsten wire) connected to a power supply and an external circuit, is the simplest form of the probe.

A Langmuir probe works by immersing its tip, as an electrode, into a discharge volume. Then a tunable electric potential is applied between the probe electrode and the surrounding vessel by the power supply. By measuring the current of probe at different potentials, the I–V characteristic is obtained. The shape of the characteristic depends on the probe shape. The plasma parameters can be extracted from the I–V characteristic after some mathematical calculations.

The I–V characteristic for a typical Langmuir probe measurement is shown in Figure 1.10. The plasma potential (V_P) is the fundamental quantity of interest in defining the nature of the plasma with respect to the bounding surfaces. By definition, when the probe is at V_P, it is at the same potential as the surrounding plasma so there is neither a retarding nor an accelerating field acting on the ions or electrons in the vicinity of the probe. The current to the probe is then determined by the capture cross section (or geometric cross section) of the probe and the random flux of particles incident on the probe [75].

When the bias voltage to the probe is sufficiently large negative, all of the plasma electrons will be repelled by the probe tip while the ions can gain enough energy to satisfy the Bohm sheath criterion and reach to the probe tip to make a current. Thus, at the high negative biased probe, the detected current is merely due to plasma ions which is called *ion saturation current*. At sufficiently high positive potential for probe (higher than the plasma potential), no ion can reach to probe tip and hence *electron saturation current* is detected which resulted in collecting all random thermal flux of the electrons. Increasing the probe potential in this regime results a slow growth of current due to the sheath expansion. These

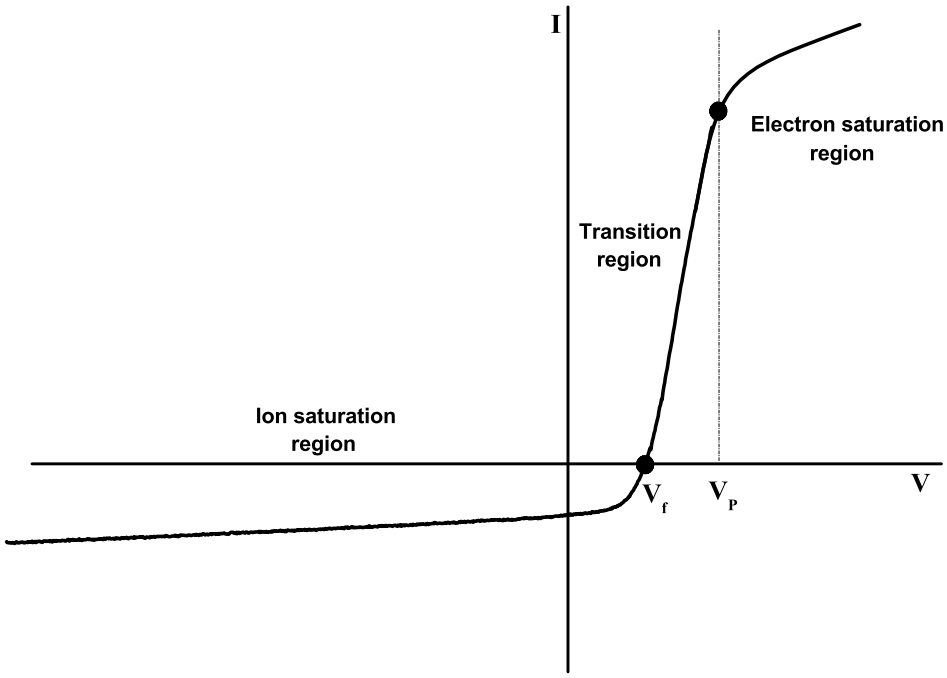

Figure 1.10: *Schematic of I–V characteristic with distinct regions. V_P and V_f show the plasma potential and floating potential respectively*

two regimes are connected by a *transition regime*. The plasma density and the electron temperature can be deduced by analyzing the transition region. The electron current is increased by decreasing the strength of negative voltage of the probe while the ion current is decreased. Then one can easily suppose that at a certain bias voltage, which called *floating potential* (V_f), the net current becomes zero (Figure 1.10). The plasma electrons are partially repelled in this regime while the ion current is almost negligible [75, 76].

In a Maxwellian plasma, the transition part of the characteristic is exponential. However, in practical situations, collisions and magnetic fields restrict the exponential part to a few KT_e. In such cases the interpretation of I–V curve is difficult. For extracting the plasma parameters, the recorded data in exponential part (transition regime) of the current–voltage characteristic should be plotted in a semi-log coordinates. The slope of the obtained straight line (ln(I)–V) is proportional to the inverse of electron temperature. Using the second derivative of current respect potential, calculated at the plasma potential, one can obtain the electron density of a Maxwellian plasma [75, 77]. In this work, a proper Matlab code was written to evaluate the characteristics obtained by Langmuir probe measurements. As will be explained in chapter 4, we used two kinds of probes for plasma characterization: a simple probe and an RF compensated probe with four LC chokes to block the RF fluctuations. Furthermore, the tips of probes were placed in the effluent plasma to avoid any plasma disturbance.

Chapter 2

Role of oxygen admixture in stabilizing TiO_x nanoparticle deposition from a gas aggregation source

Amir Mohammad Ahadi, Vladimir Zaporojtchenko, Tilo Peter, Oleksandr Polonskyi, Thomas Strunskus, and Franz Faupel

Chair for Multicomponent Materials, Institute for Materials Science, University of Kiel, 24143 Kiel, Germany

2.1 Abstract

For the use of a gas aggregation cluster source a high and stable deposition rate is desired. For many metals, nanoparticle formation is enhanced by admixture of reactive gases. Here, the role of reactive gas admixtures on the nanoparticle deposition rates is investigated for the case of reactive direct current magnetron sputtering of Ti in a gas aggregation chamber. The results show that, at low working gas (argon) pressures, stable cluster deposition at high rates can only be achieved for admixtures with a very narrow oxygen flow range. At higher pressures, stable deposition can be observed only after an intermediate maximum rate has been crossed or a stable deposition rate is not reached at all. For the different sputtering conditions, the partial pressure of oxygen was monitored with a mass spectrometer. The results are explained in terms of the competing roles of oxygen in cluster nucleation as well as in target poisoning. The cluster size distributions for different conditions were characterized by scanning electron microscopy.

2.2 Introduction

Since many years, nanocluster research has evolved as a new and interesting field in nanoscience [14, 78–80] particularly due to the exclusive features of clusters and their role in the transition from atomic scale to bulk material. Metal clusters as one of most investigated class of clusters show interesting physical [81–83] and chemical [80, 84] properties. They also play an important role in the fabrication of new nanocomposite materials and in adjusting the properties of these materials [1, 2]. The formation processes and applications of this type of clusters [4, 27] are, therefore, an attractive field of research for many researchers from different magnetron sputtering combined with a gas aggregation chamber, introduced by Haberland et al. [9], is an attractive method for metal cluster production. For this method, several theoretical [25, 26] and experimental [85–87] studies were concerned with the effect of sputtering parameters and environmental conditions on cluster formation. For some chemical elements, especially for highly reactive metal atoms which have low dimer binding energy, conventional direct current (DC) magnetron sputtering in combination with pure argon aggregation gas is not able to create stable cluster nuclei. Adding a small amount of reactive gas to the working gas is a typical solution for these elements. This method increases the probability of nucleation (and cluster growth) in collisions by production of compound molecules [10]. Many investigations [2, 88, 89] considered cluster formation from reactive magnetron sputtering in the gas aggregation cluster source, but most of them focused on the properties of the deposited films (nanocomposite thin films as well as pure cluster films) and their applications. Drabik et al. [88,89] studied the morphology and structure of Ti clusters films prepared by the Haberland method. The aging effect of samples produced at different magnetron currents and different pressures was also considered. They found [88, 89] that when as prepared titanium cluster films are exposed to the air atmosphere, the deposited clusters oxidize immediately (and prepared films turn to transparent). However, they did not study the role of impurities (reactive gas) on cluster formation. Recently, few studies tried to explain the role of reactive gas in cluster formation and seeding processes. Marek et al. [11] investigated the effect of changing oxygen admixture (as a reactive gas) on cluster production at constant argon aggregation pressure and found that adding a small amount of oxygen can improve cluster generation dramatically. In a previous study [10] we analyzed the influence of the reactive gas on the formation process of transition metal clusters in a gas aggregation chamber. It was found that at each operation condition, cluster generation can only take place within a specific concentration range of reactive gas. Outside this range, no cluster formation takes place, since a reactive gas flow below the minimum of the range cannot promote cluster nucleation, and a reactive gas flow higher than the maximum of the range leads to target poisoning, which decreases sputtering and thus makes cluster production impossible. Stable cluster production at different conditions is important for technical applications. However, due to high reactivity of Ti and other reactive metal atoms, the stabilization of cluster deposition is very difficult. Furthermore, several complex processes, such as resputtering and oxide molecules formation in the volume and on the surfaces, influence the clustering processes in reactive sputtering and make stabilization of deposition quite complicated. To date, the influence of reactive gases on the stabilization of cluster production in a gas aggregation chamber has not studied for Ti or other metals, although,

understanding of the underlying mechanisms is crucial to control the physical and chemical processes in the aggregation chamber during cluster formation, and hence the properties of deposited cluster films. When reactive gas is added to the aggregation chamber, several processes can occur. The reactive gas can promote cluster nucleation by binding to the sputtered metal atoms and creation of compounds. These molecules have a much higher binding energy in comparison with binding between pure metal atoms and can accelerate the cluster nucleation process (and also cluster growth) in collisions [10]. The reactive gas can also cause poisoning of the target surface [90]. This takes place in two ways: The first one is diffusion or flow of reactive gas into the aggregation chamber. Thus, reactive gas molecules can arrive on the target directly and react with surface atoms and produce dielectric compounds on it. The second poisoning mechanism is that some oxidized metal atoms arrive on the target from the gas phase and are incorporated into the growing oxide. Other possible scenarios for oxygen molecules are sticking to the chamber walls and escaping from aggregation chamber via the orifice. It is well–known [91] that the number of sputtered atoms decreases strongly upon increasing fraction of poisoned active target surface. The number of sputtered atoms in turn and its affecting parameters (such as erosion area, power, and pressure) control the amount of reactive gas consumed in the different processes. In other words, the number of accessible sputtered atoms in the aggregation chamber determines the quantity of reactive species consumed for compounds generation. Hence, by varying the working pressure not only the number of sputtered atoms, but also the number of molecules returning to the target can be changed. This means that just by adjusting the working pressure, the consumption rate of reactive atoms as well as the rate of surface poisoning can be tuned. Thus, we expect the deposition rate (D.R.) evolution and also the clustering processes to vary markedly with pressure. According to the theoretical models [25, 27], cluster production (and growth) take place in three steps:

1. Cluster nucleation via three body collisions.

2. Cluster growth by binding of single atoms.

3. Clusters coalescence.

During each reaction, some thermal energy is released and dissipated by the working gas particles. If they cannot transfer the released reaction energy completely, the remaining thermal energy can dissociate particles from the cluster. The final clusters size depends on the particle densities of the different species which contribute in the nucleation and growth processes, the cluster residence time in the aggregation chamber, and the temperature. The residence time is affected by the length of aggregation chamber, the working pressure, and the gas flow [5]. In the present work, we considered the various processes discussed above and analyzed several possibilities for stabilization of TiO_x cluster formation in DC magnetron sputtering from a pure titanium target in a gas aggregation cluster source. Using oxygen, we investigated the role of reactive gas flow in the different processes and studied its role in stabilizing cluster formation. We show that the stability of cluster deposition under different conditions depends strongly on the amount of reactive gas and the dominant mechanism, and we report the specific optimal conditions which lead to highly stable cluster formation.

2.3 Experimental Setup

The planar magnetron was installed in a self–constructed gas aggregation chamber [92]. It equipped with a 2 inch round titanium target (99.99 percent purity) with 6 mm thickness. For TiO_x cluster generation, argon and small amount of oxygen were used as working gas and reactive gas, respectively. The aggregation chamber was connected to the main chamber (deposition chamber) via an orifice with 3 mm in diameter. The pressure in the aggregation source was set between 50 and 200 Pa and measured by a MKS Baratron. A MKS mass flow controller (200.0 sccm) and Apex mass flow controller (1.000 sccm) were applied to control the argon and oxygen flow, respectively. The Argon flow rate was in the range of 25 – 110 sccm, and the range of applied oxygen flow was between 0.010 and 0.140 sccm. The magnetron was connected to a DC power supply (MDX 500, Advanced Energy). In the present work, the used power was in the range of 30 – 100 W. The D.R. in each step was monitored by quartz crystal microbalance (QCM), which was placed in the deposition chamber, 6 cm away from the orifice of aggregation source. Evolution of cluster deposition was monitored for 25 – 45 min to observe a distinct trend in the evolution. A turbo molecular pump (TMP) (Pfeiffer TMU 261) supported by a scroll pump (SP) (Varian SH 110) was linked to the deposition chamber for pumping down to about 10^{-5} Pa as background pressure before each experiment. For monitoring the signal of the oxygen molecules escaped from the aggregation chamber, a quadrupole mass spectrometer (QMS) (Balzers Prisma QMS – QME200) equipped by a channeltron/Faraday detector was used. It was located in a tube attached to the main chamber separated by a variable valve to allow differential pumping by a turbo pump (Pfeiffer HiPace80). During the experiments, the mass spectrometer was adjusted to monitor only the oxygen (32 amu) and the Argon (40 amu) concentrations. The chamber of the mass spectrometer was pumped down by a turbo pump (Pfeiffer HiPace80) to 10^{-7} Pa base pressure. The mass spectrometer chamber also was connected to the deposition chamber by a tube and variable valve. For cluster size evaluation, samples were prepared at the position of the QCM on silicon substrates. These samples were then analyzed by a SEM (Zeiss – Supra 55VP). Figure 2.1 shows our setup schematically.

2.4 Measurements and discussion

The effect of oxygen as an impurity species on cluster formation and cluster deposition from the gas aggregation cluster source was investigated at different pressures. In all experiments, initially the target surface was cleaned by pure argon discharge. Depending on the target history, the time of the cleaning process was different. Directly after cleaning, no cluster deposition was detected as observed before [10]. Afterward, oxygen as a reactive gas was added to the argon working gas in the aggregation chamber, and the D.R. was measured with a QCM monitor placed in the main chamber. The first experiment was performed at 50 Pa by injecting 25 sccm argon into the aggregation chamber. The discharge was run at 50 W, and different concentrations of oxygen were used. Some minutes after starting the oxygen flow, the D.R. increased dramatically and reached a knee as shown in Figure 2.2.

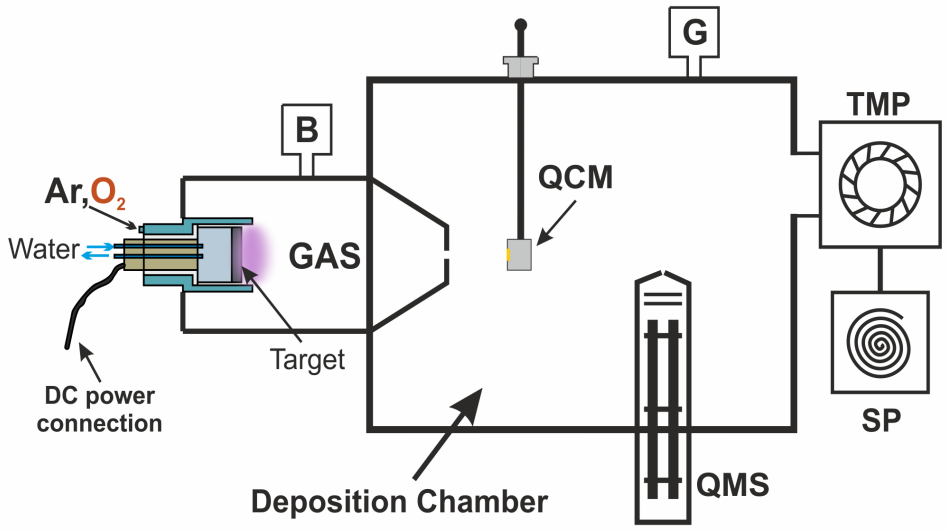

Figure 2.1: *Schematic of the experimental setup. A magnetron source is mounted in the GAS. A QCM and a QMS are used for recording cluster D.R. and the amount of oxygen molecules escaping from aggregation source, respectively. The system is evacuated by a TMP supported by a SP. A gauge (G) and a baratron (B) are used for measuring the pressure in the main chamber and aggregation chamber, respectively*

For 0.080 sccm, the D.R. was highly stable after the initial increase. Apparently at the beginning, after adding oxygen to the gas aggregation chamber, sticking to the chamber walls, and surface target poisoning are dominant processes for oxygen consumption, while the oxidation of sputtered atoms in the gas volume is of minor importance. Therefore, a delay in deposition is observed which depends on the applied oxygen flow. After this primarily step, metal atom oxidation is the main process in the gas volume. When the number of oxide molecules becomes high enough, the cluster nucleation process and in the next step the growing process is started. These processes will continue until equilibrium between sputtering rate and cluster formation is established and the knee is reached in the D.R. curve. Afterward changes in the local poisoning area on the target control the D.R. evolution. If the oxygen flow is equal to the amount which is needed for stabilization, the poisoned region will remain constant. Under this condition, the sputtering rate is also constant, and cluster formation as well as the D.R. is stable. Here, the rate of enlarging the poisoned regions on the target by the poisoning processes discussed above and the rate of surface cleaning by impact of ions are in equilibrium. The evolution of bias voltage during cluster deposition (Figure 2.2, left) also confirms that the fraction of poisoned regions on the target is stable.

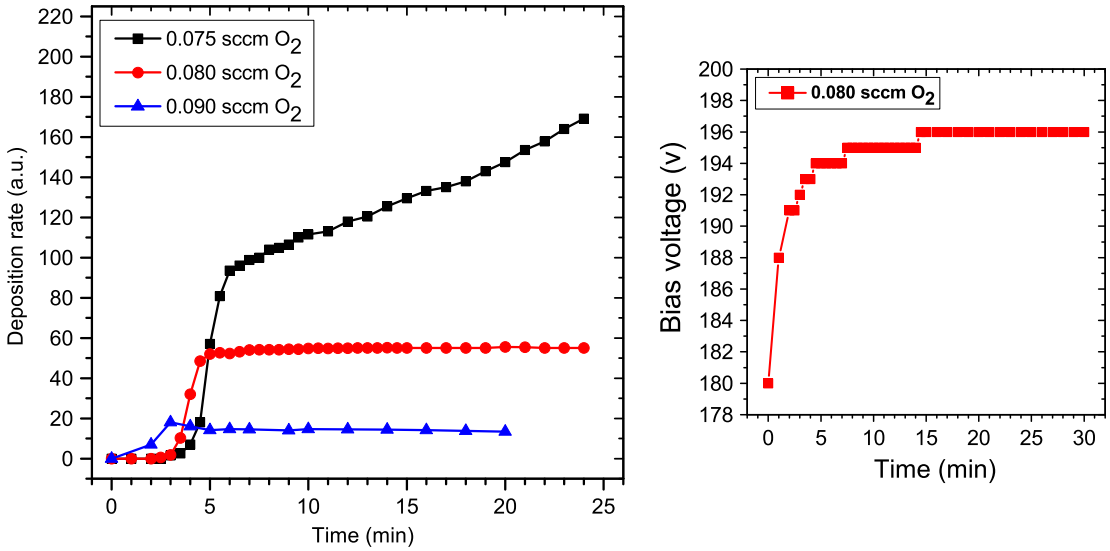

Figure 2.2: *Cluster D.R. evolution (left) at 50 Pa of argon pressure in the gas aggregation chamber and different oxygen flows. In all experiments, the magnetron power was 50 W. One notes that a change in oxygen flow strongly affects the D.R. curves. A highly stable D.R. for long time is only achieved for one oxygen flow. The magnetron bias voltage evolution during deposition for this stable case is shown on right.*

In other cases, where the oxygen flow is lower or higher than the optimum flow, the equilibrium between poisoning and cleaning on the target surface cannot be established completely, and variations in the poisoned area lead to a drift in the D.R. (Figure 2.2). We note that, when the cluster formation processes sets in, less amount of oxygen in comparison with the initial steps is available for poisoning because some oxygen is consumed for cluster production. Thus, at the oxygen flows lower than required for the stable case, the poisoned areas start to shrink because the cleaning process by impacting argon ions is stronger than target poisoning processes, and consequently, the target surface will be cleaned gently. Enlarging the cleaned area enhances the sputtering rate of metal atoms which leads to more cluster nucleation. Therefore, an increase in cluster generation is recorded (Figure 2.2). We expect that, after a long time, a constant D.R. might even be established in this case. In the opposite case, by increasing the oxygen flow rate above the optimum value, the rate of target poisoning gets higher than the rate of the cleaning process by incoming argon ions. Then, due to enlargement of the poisoned area, the sputtering rate and subsequently the cluster formation will diminish gradually. We mention that beside cluster seeding by sputtered off pure metal atoms, direct sputtering of oxide molecules (TiO_x) from the surface target can also contribute to the clustering processes. These TiO_x molecules can be produced on some clean parts of the target by binding of arriving oxygen atoms with surface titanium atoms if they will be sputtered off by impacting argon ions immediately after creation. It is important to note that, at low pressure in the aggregation chamber (50 Pa), due to the long mean free

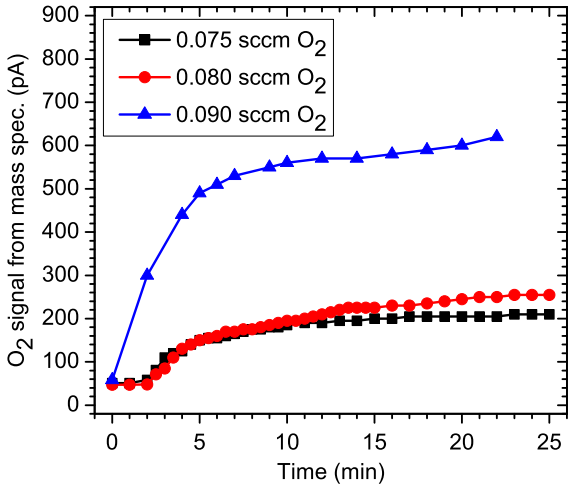

Figure 2.3: *Mass spectrometer signal evolutions for different oxygen flows at constant argon pressure (50 Pa). The amount of escaped oxygen particles strongly depends on the oxygen flow as well as the dominant poisoning mechanisms in each condition*

path, the contribution of returning oxidized atoms in surface poisoning is expected to be weak because they have only a low probability to collide with other particles and return to surface. Thus, direct diffusion or flow of oxygen to the target is the dominant mechanisms for surface poisoning. To study the role of the oxygen concentration in clustering and in poisoning of the surface in more details, a mass spectrometer was installed and linked to the main chamber in order to monitor the oxygen molecules which escaped from the aggregation chamber. For the stable case (0.080 sccm), the O_2 signal does not change in the first $2-3$ min (Figure 2.3), indicating that in this period (as discussed above), the oxygen is consumed mainly by the available sputtered metal atoms on the aggregation chamber walls (which were produced during the cleaning process), and by the poisoning process on the target surface. After these preliminary processes, oxidation of sputtered metal atoms in the gas volume is dominant. Consequently, clustering processes are initiated, and then the residual oxygen molecules escape from the cluster source and the spectrometer signal increases. When a relative equilibrium among sputter rate, cluster formation, and surface poisoning is established after the knee region in Figure 2.2, the oxygen signal increases very gently. This trend of the oxygen signal can be explained by saturation of the adsorption of oxygen molecules on the aggregation chamber walls. When the number of oxygen molecules arriving at the walls reaches to the saturation value, more oxygen molecules can escape from the aggregation chamber and increase the signal of oxygen molecules. For other oxygen flows, the plateau of the oxygen signal emerges at different times (Figure 2.3).

It is clear that the oxygen signal is affected not only by the absolute value of oxygen flow, but also by the clustering and poisoning process under each condition. The plateau of the oxygen signal for 0.090 sccm is nearly 2.5 times higher than the plateau for the stabilized case (0.080 sccm of oxygen flow). The higher oxidation rates of the target and

lower sputtering rate at 0.090 sccm oxygen flow lead to an escape of a high amount of oxygen from the aggregation chamber after the initial stages. In contrast, in the case of 0.075 sccm oxygen flow, the oxygen signal after an initial increase shows only a small difference in comparison with the signal for the stabilized case. The absolute amount of oxygen flow is the main factor for this difference. As we discussed before, at 0.075 sccm, the consumption of oxygen for the poisoning process is lower than for the stable case, but at the same time, due to the higher sputtering rate, more oxygen is consumed in clustering. Therefore, the higher consumption rate of oxygen for clustering can compensate the lower rate which is used for poisoning, and thus the oxygen signal is mostly flat after the initial increase.

In a next step, we studied the effect of magnetron power on cluster deposition. As shown in Figure 2.4, the stable part of the deposition curve strongly depends to the magnetron power. Since the number of sputtered atoms strongly depends on the applied power, higher cluster nucleation rates can be achieved by increasing magnetron power. We noted that in the investigated range from 30 to 100 W, the oxygen flow required to obtain stable cluster deposition depends almost linearly on the magnetron power (Figure 2.4).

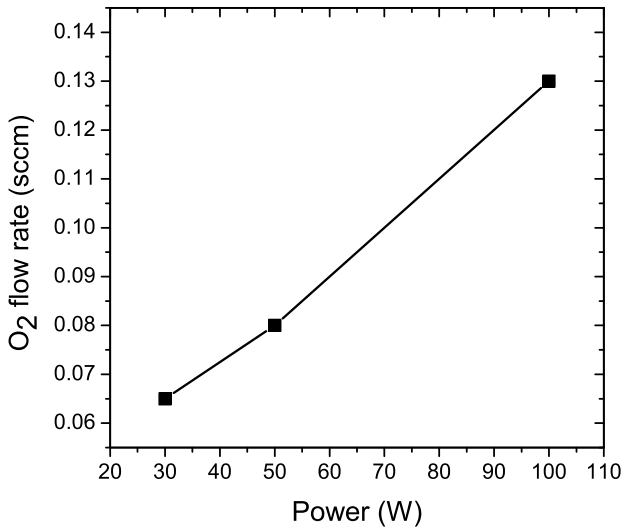

Figure 2.4: *Necessary oxygen flow for stabilization of cluster formation at different powers. The oxygen flow was changed for each feeding power to find the flow for stabilized cluster formation. One notes an almost linear relationship between power and optimum oxygen flow at constant argon pressure (50 Pa).*

Cases of stable operation are shown in Figure 2.5(a) for 30 and 50 W applied power. Due to higher sputtering rate at higher power, the stable part is shifted to higher D.R.s. The results obtained for the evolutions of the D.R. at 100 W (Figure 2.5(b)) are mostly similar to the behavior at lower powers, but they also show some specific trends not seen in at lower power. A longer delay in cluster formation and a shift of the knee in the D.R. curve are the first difference. This delay was observed for all investigated oxygen concentrations. The

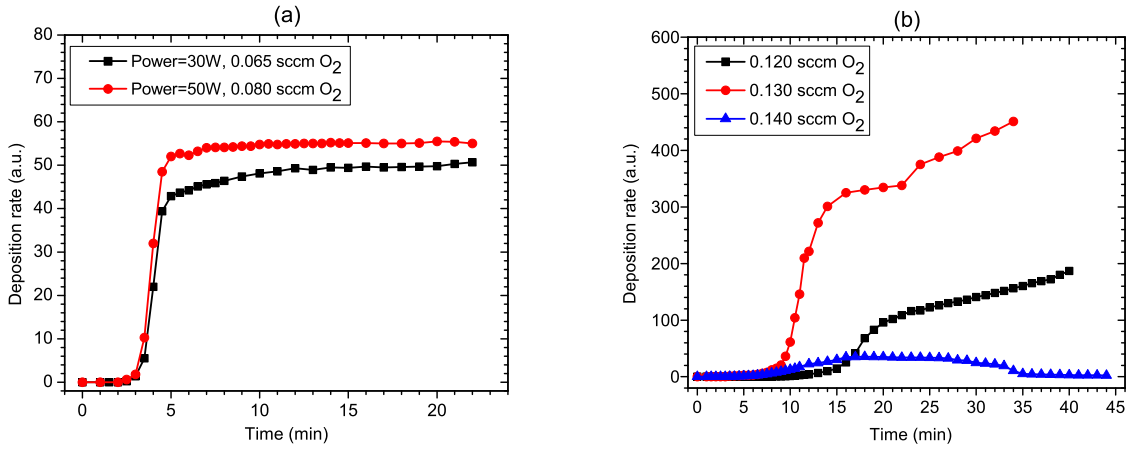

Figure 2.5: *(a) Examples of stable cluster deposition for operation at low magnetron powers. (b) Evolution of the D.R. for different oxygen concentrations at 100 W. Here stable deposition is not observed within the experimental observation time. All experiments were carried out at 50 Pa of argon, and the oxygen flow was varied to obtain stable deposition.*

other difference was observed for the specific oxygen flow of 0.130 sccm. According to the results obtained in the experiments for lower powers, it was expected to achieve a highly stable cluster D.R. for 100 W power at an oxygen admixture around 0.130 sccm. While at this conditions, the D.R. curve shows a first knee before the expected knee point, then remains stable as expected, but for just 8 – 10 min, and subsequently starts to increase again (Figure 2.5(b)). It seems, that more investigations are required to clarify this behavior at high power. The drop of the D.R. at the higher oxygen flow of 0.140 sccm at longer times is attributed to target poisoning.

At higher feeding power, the number of accessible Ti atoms in the aggregation chamber increases, which should lead to the formation of larger clusters. Similar studies on Ni [85] and Ag [5] also showed bigger clusters at higher magnetron power. To test the effect of magnetron power on the particle size distribution for Ti, we took SEM pictures of the deposited clusters prepared under stable conditions. One sees in Figure 2.6 that the mean particles size is the same for different magnetron powers. However, the amount of deposited clusters increases with feeding power.

It seems that cluster growth is reduced at higher power in the present case. To find the reason for this unexpected observation, the temperature evolution of the aggregation chamber was monitored during deposition as temperature is known to affect particle size [87]. For both conditions of lower power (30 and 50 W), the temperature of the aggregation chamber walls (outside) was constant and its value remained at the initial temperature throughout of deposition process. In contrast, at the same time at 100 W, the temperature increased by 8 – 10 K.

It is clear that the temperature increase of the inner chamber walls was considerably higher than measured from outside of chamber. Processes such as transfer of thermal energy

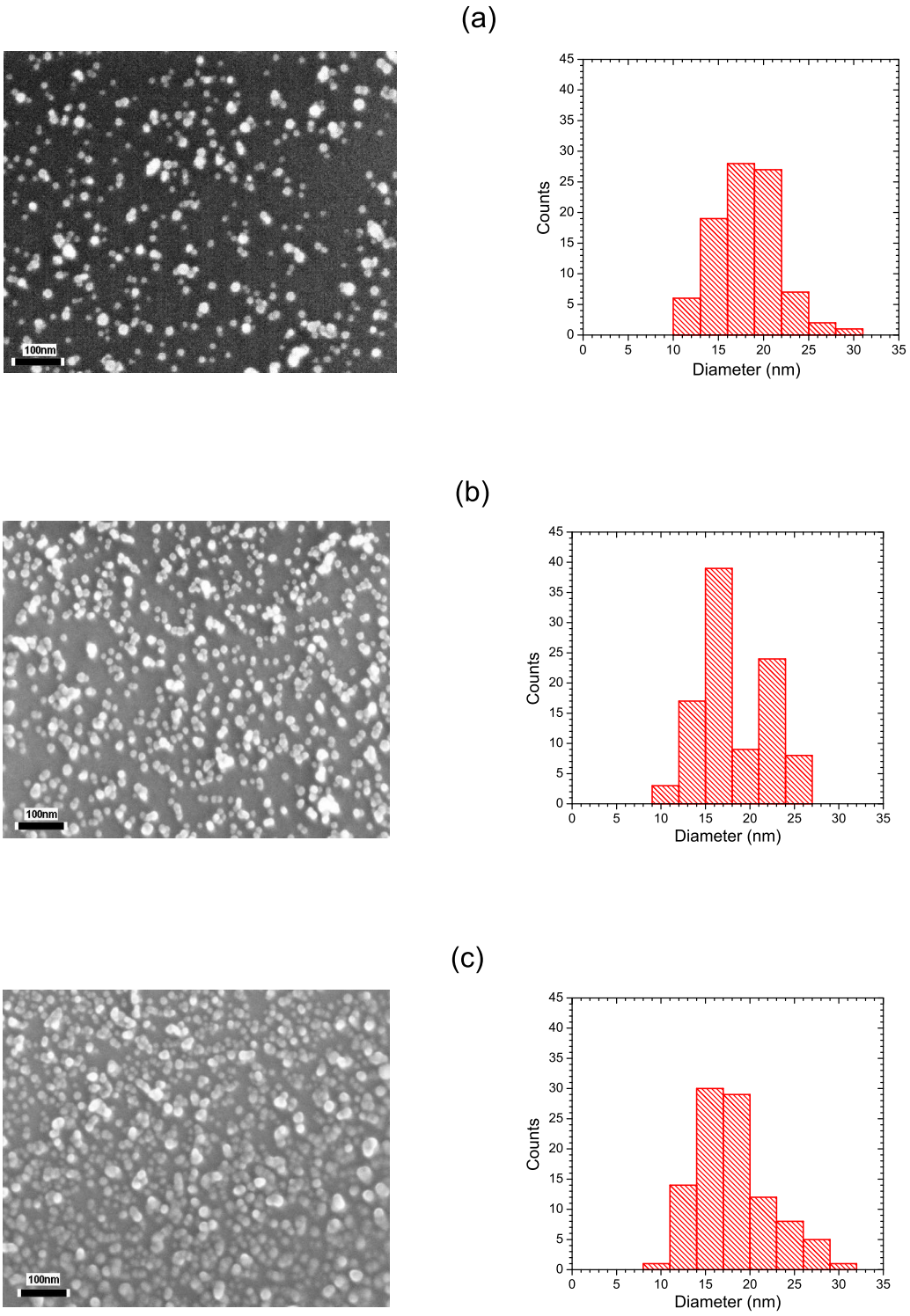

Figure 2.6: *SEM images (left) and corresponding histograms (right) of the samples prepared under conditions of stable D.R. with different powers and constant argon pressure (50 Pa). (a) Power = 30 W and O_2 flow = 0.065 sccm (b) Power = 50 W and O_2 flow = 0.080 sccm (c) Power = 100 W and O_2 flow = 0.130 sccm. In all cases, the mean particle size is around 18 nm.*

from the magnetron to the gas volume by argon and sputtered atoms [93], oxidation and clustering processes in the gas volume, and also recombination of charged particles are noticeable factors for elevating the temperature in the gas aggregation cluster source. Although, the role of the individual mechanisms is not well–known yet, and further investigations are needed to clarify this subject, the increase in the temperature of the inner chamber walls can well explain the absence of cluster growth at higher magnetron power.

To determine whether a stabilization of the deposition process is also possible at other argon pressures, we analyzed the deposition at different pressures and with different oxygen concentrations. At 100 Pa, corresponding to 51 sccm argon flux into the gas aggregation source (GAS), the trend of the initial stage for evolution of the D.R. was identical to that at 50 Pa, but when the deposition curve reached to the knee, the D.R. started to drop and after some minutes reached zero (Figure 2.7(a)). By varying in oxygen flow we did not reach to a long-term stabilization of the D.R. Changing the oxygen amount only leads to a change in the time of the appearance of the peak and in the width of the maximum, but not to stable deposition. Higher oxygen flows lead to earlier peaks due to faster oxidation of available sputtered atoms in the volume and also faster oxidation of the target surface. The highest full width at half maximum (FWHM) of the deposition at 100 Pa was obtained for 0.040 sccm oxygen flow. At oxygen concentrations above or below this value, the FWHM was reduced (about 35 percent for both cases), indicating that further changes in oxygen flow will not result in stable deposition (Figure 2.7(a)). The observation that stable deposition cannot be achieved at 100 Pa pressure in the above oxygen concentration range can be explained by the fact that the number of metal-oxide molecules returning to the target under this condition is quite high. The returning oxidized atoms expand the poisoned region and decrease the sputtering rate quickly and impacting argon ions are not able to provide a large clean area on the target. Thus, the sputter rate will not be sufficient for cluster nucleation. The evolution of bias voltage (Figure 2.7(a)) shows a continuous growth which is due to the continuous enlargement of the poisoned regions on the target.

The oxygen signal evolutions in the mass spectrometer for different concentrations of oxygen is in agreement with this notion (Figure 2.7(b)). After an initial period, where all oxygen particles are consumed for target poisoning, sticking to chamber walls, and clustering, the signals grows continuously. The increasing poisoned region on the target and the drop of cluster formation leads to an escape the most of the free oxygen molecules from the aggregation chamber, and hence to an increasing oxygen signal in the mass spectrometer.

Finally, we studied the clustering process and the effect of oxygen at 200 Pa by applying 107 sccm argon flow to the GAS. At this pressure the D.R. shows a maximum similar as at 100 Pa. However, at 200 Pa, the D.R. does not fall to zero, but to a constant, stable value (Figure 2.8(a)), while the oxygen signal evolutions for different oxygen flows are similar to the behavior at 100 Pa. This indicates that the underlying processes at both pressures are almost the same. As seen in Figure 2.8(a), the stable part for different oxygen flows has the same absolute amount. A possible explanation for this behavior could be the high number of argon ions impacting on the target at 200 Pa. These ions can apparently sputter off enough TiO_x molecules from the target surface to enable cluster formation in the gas volume. At constant power and constant pressure, the impingement rate of argon ions on

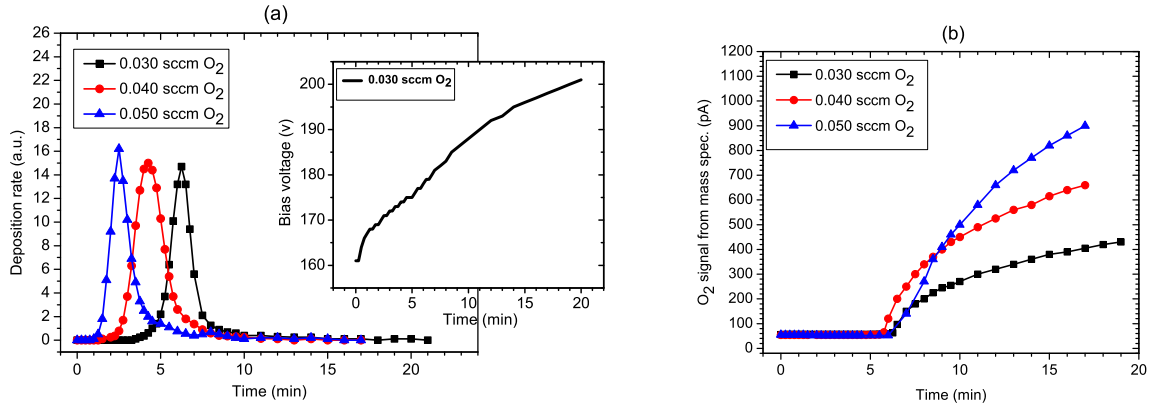

Figure 2.7: *(a) Cluster D.R. and bias voltage evolution for different oxygen flows during deposition at a higher argon pressure of 100 Pa. (b) Evolution of the mass spectrometer signal for escaped oxygen molecules (mass = 32 amu) from the aggregation chamber during cluster deposition. Measurements were done at a constant power of 50 W. Different oxygen flows only change the time of the peak appearance and the width of the peak, but a non-zero stable deposition is not reached.*

the target surface is almost constant, therefore, cluster seeding is similar for the different applied oxygen concentrations.

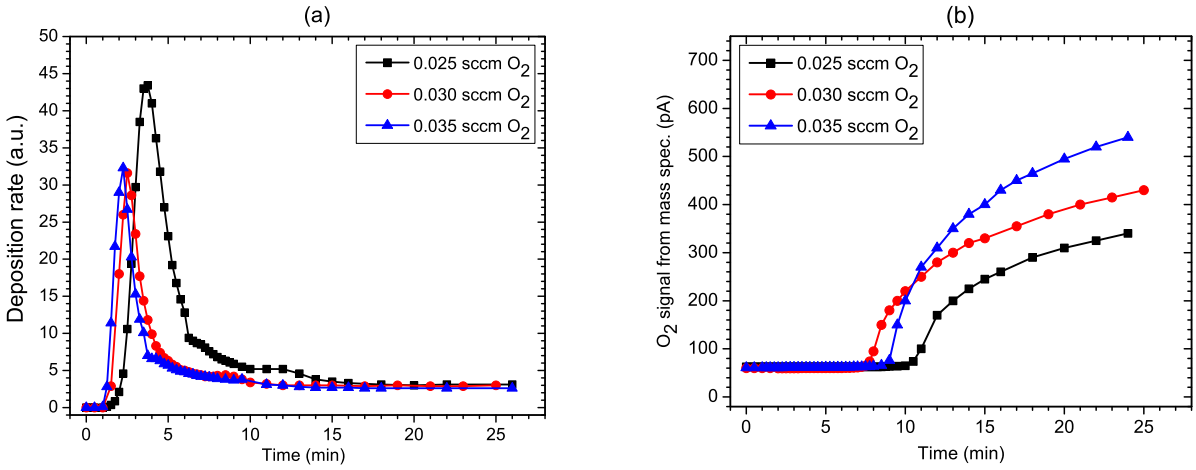

Figure 2.8: *(a) Evolution of the cluster D.R. at 200 Pa argon pressure. An identical stable non-zero plateau is reached after a maximum for all oxygen flows. (b) Evolution of the mass spectrometer signal for the oxygen molecules (mass = 32 amu) escaped from the aggregation chamber during cluster deposition.*

As for an argon pressure of 100 Pa, the peak in the D.R. curve shifts to later times with decreasing oxygen flow (Figure 2.8(a)). Additionally, at this pressure the cluster deposition for the lowest oxygen flow (0.025 sccm) shows a higher peak and also a higher total amount

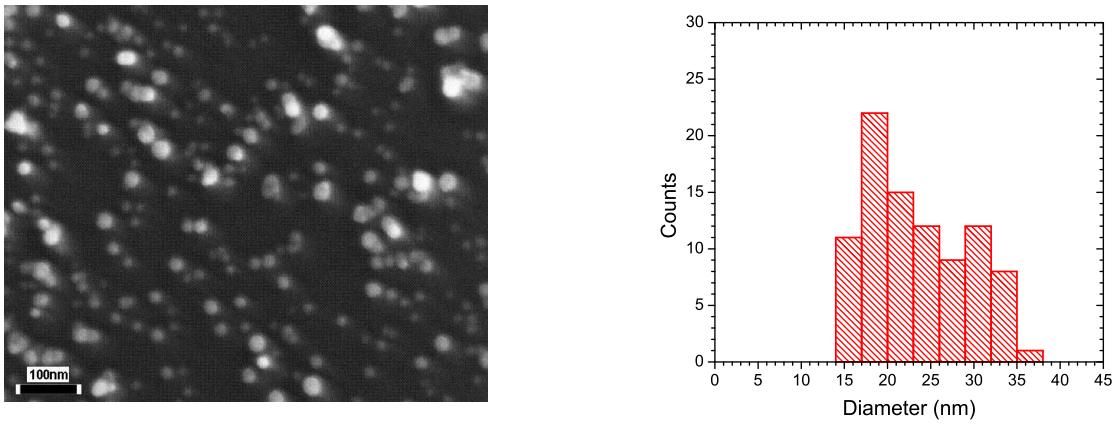

Figure 2.9: *SEM image (left) and corresponding histogram (right) of a sample prepared in the stable part of D.R. curve at 200 Pa. The oxygen flow rate was 0.030 sccm, and the magnetron power was 50 W. The mean clusters size is about 23 nm.*

of deposited material than for other oxygen flows (Figure 2.8(a)). It seems that the lower amount of oxygen arriving at the target surface provides a larger clean area on the target surface during the initial stage. Thus, a higher sputtering rate provides higher cluster seeding in this regime. For the same reason, the oxidation of sputtered atoms in the gas volume is initially decreased. Consequently, the starting time of cluster deposition, the appearance of the peak, and also the time for reaching the stable part are delayed. At oxygen flows lower than 0.025 sccm, no cluster deposition was recorded by QCM. Due to different oxygen consumption in the aggregation chamber for different oxygen flows, the onset of the oxygen signal for 200 Pa (Figure 2.8(b)) depends on the absolute oxygen amount. The size distribution of the clusters formed in the stable part at 200 Pa and its related histogram is shown in Figure 2.9. At high pressure, the small mean free path and the resulting high collision frequency leads to the formation of large clusters.

2.5 Conclusions

Using Ti and oxygen as examples, we studied the influence of reactive gas admixtures on the formation of TiO_x clusters during reactive DC magnetron sputtering in a gas aggregation chamber and explored regimes of stable cluster formation. We could stabilize TiO_x cluster formation by adjusting the oxygen flow at an argon pressure of 50 Pa. The range of oxygen flow for stable operation is very narrow and depends strongly on the magnetron power. At an argon pressure of 200 Pa, stable cluster formation is obtained after going through a maximum. The stable rate turned out to be independent of the oxygen flow in the investigated range. At 100 Pa, the D.R. also goes through a maximum, but subsequently drops down to zero. The crucial role of oxygen is also confirmed by mass spectrometry. The results are

explained by a competition between oxygen induced cluster nucleation and target poisoning.

2.6 Acknowledgements

This work was supported by the German Research Foundation (DFG) within the framework of the Collaborative Research Center SFB TR 24, subproject B13. One of us (A. M. Ahadi) is grateful to the Iran Ministry of Science for financial support. We would also like to thank Stefan Rehders for the technical construction of the cluster source, Rainer Kloth for technical support, and C. Sch utte for her comments.

Chapter 3

Stable production of TiO_x nanoparticles with narrow size distribution by reactive pulsed DC magnetron sputtering

Amir Mohammad Ahadi,[1] Oleksandr Polonskyi,[1] Ulrich Schürmann,[2] Thomas Strunskus,[1] and Franz Faupel[1]

[1]Institute for Materials Science – Multicomponent Materials, University of Kiel, 24143 Kiel, Germany

[2]Institute for Materials Science – Synthesis and Real Structure, Kiel University, 24143 Kiel, Germany

3.1 Abstract

The pulsed DC magnetron technique was used for generating TiO_x nanoparticles by sputtering from a titanium target in a gas aggregation source. It was observed that the deposition rate (D.R.) of nanoparticles shows a peak followed by a broad tail, even for constant operation conditions. As a key finding of the present investigation, we show that nanoparticle deposition can be stabilized at nonzero D.R. for the pulsed power regime. Monitoring the oxygen concentration by mass spectrometry provides insight into nanoparticle generation in different processes. Characterization of the nanoparticle film morphology based on transmission electron microscopy reveals a very narrow size distribution. Furthermore the oxygen admixture has a significant influence on the size distribution and also on the mean size of the formed nanoparticles. In-situ analysis the chemical composition of the deposited films directly after preparation by X-ray photoelectron spectroscopy shows a major contribution

of sub–oxide titanium compounds to nanoparticle production.

3.2 Introduction

TiO_x nanoparticles not only exhibit intriguing properties such as photocatalytic activity [94], wettability [95] and magnetism [96] with hosts of applications as free particles but are also interesting for the fabrication of functional nanocomposites [94, 97]. Nanocomposites containing nanoparticles, particularly metals/oxide and metal nanoparticles have been studied intensively during the last decade [2, 98]. Chemical and physical properties of different species, their relative densities as well as the size distribution of the nanoparticles are crucial parameters in adjusting different properties of the resulting nanocomposite materials [2,99].

There are several methods based on physical vapour deposition (PVD), such as laser ablation, ion beam sputtering and evaporation [3] which can be used for metal cluster and nanoparticle production. Also a supersonic cluster beam deposition using a pulsed microplasma cluster source has been successfully applied to produce many different types of nanoparticles including titania nanoparticles [100]. Magnetron sputtering combined with a gas aggregation source (GAS) is a very interesting method and frequently used, especially for nanoparticle generation of metals and their related compounds in nanotechnology [4]. The properties of the nanoparticles formed by this method can be tuned easily by varying the operation parameters. Recent results also showed that by applying pulsed power for reactive species, a huge increase in nanoparticle deposition rate can be achieved [5], which suggests this method as a good candidate for industrial application.

A wide size distribution and time instability are the main practical difficulties for nanoparticle production by a GAS. Therefore the fabrication of nanocomposites with certain optical and chemical properties is rather complicated using this method. For nanoparticle formation from reactive metal atoms typically a reactive gas as a minor admixture is necessary [10, 11, 101]. In our previous work, we successfully stabilized TiO_x nanoparticle production by GAS at continuous DC power regime, but only for certain operation conditions [12]. However, at intermediate pressure (100 Pa) due to dominant resputtering of oxide components, stabilization was not achieved [12]. On the other hand, our recent work on pulsed DC sputtering shows that the governing mechanisms in the pulsed power mode show some differences compared to the continuous DC mode which leads to an enhanced rate of nanoparticle deposition [13]. So far the influence of continuous stream of reactive gas and particularly the conditions for stabilized nanoparticle production were not considered. In the pulsed power regime the complete fed in energy is delivered in a desired much shorter period (which is tuned by duty cycle and repetition frequency). This allows that with a reactive oxygen gas admixture in the plasma on period more TiO_x compounds are sputtered off from the Ti target rather than pure Ti atoms [13]. These off sputtered compounds enhance the density of the stable nucleation centres in the GAS volume [13]. Furthermore, the impact of highly energetic ions at a short period of *time on* (t_{on}) provides a higher sputtering rate. Both facts lead to more efficient nanoparticle generation. It is noticeable that target oxidation is a continuous process which depends on oxygen flow and diffusion as well as on

the clustering process in the GAS. In principle, the rates of the target oxidation at t_{on} and *time off* (t_{off}) intervals should be identical. The most important difference is that the oxide components which are formed at t_{on} are sputtered off immediately after their creation on the target by the highly energetic impacting ions. While at t_{off}, due to absence of highly energetic ions, they remain on the target and lead to formation and growth of poisoned spots on the Ti target, at least, up to next t_{on} period. Therefore the poisoning process and the total amount of oxide material on the target surface increase with t_{off}.

In this work, we consider the effect of the operation conditions on TiO_x nanoparticle production in the pulsed power regime when a steady stream of oxygen is added as a minor species to the GAS atmosphere. The governing mechanisms for nanoparticle generation are addressed and we demonstrate stable nanoparticle formation at intermediate pressure (100 Pa) in the GAS which was not achieved in the continuous DC regime [12]. The results indicate that by using pulsed power not only higher total deposition rate can be achieved [13] but also stable nanoparticle formation will be reached at certain operating parameters. We also present an in-depth study of the effect of pulsing parameters and amount of the admixed oxygen in a continuous gas stream. Based on TEM images the particle size distribution of samples prepared at stable D.R. were analysed. In contrast to broad size distributions observed in the continuous DC regime [12], nanoparticles prepared in a pulsed regime show very narrow size distributions. Furthermore, the average size of the TiO_x nanoparticles becomes larger with increasing the amount of admixed oxygen. Therefore the nanoparticle size can be controlled in the pulsed DC regime just by changing the oxygen admixture at typical operating conditions. The chemical composition of the prepared nanoparticle films was examined by X-ray photoelectron spectroscopy (XPS). Previously, Drabik et al. reported the morphology and chemical composition of TiO_x nanoparticle films prepared in a continuous DC regime without oxygen stream and after aging in air [88, 89]. In the present work the composition of the prepared nanoparticle films was measured directly after deposition without exposure to ambient. The results provide clear evidence for the contribution of sub–oxidized (TiO_x) compounds in the nanoparticle formation process. After air exposure for several days, the nanoparticles films are mostly fully oxidized to TiO_2.

3.3 Experimental

A two inch balanced planar magnetron with a Ti target (99.99% purity, 50 mm diameter and 6 mm thickness) was installed in a home-made gas aggregation cluster source (GAS) described elsewhere [92]. The water cooled magnetron was fed by a DC power supply (MDX 500, Advanced Energy) via a self-constructed pulsing box employing a power MOSFET (HTS-31, Behlke Electronic GmbH). Furthermore a signal generator (peak Teck 4025) was connected to the pulsing box directly to obtain the desired pulsed DC power. Argon as a working gas and oxygen as an admixed reactive gas were used for sputtering and the aggregation processes in the GAS. The flow of argon and oxygen were controlled by a MKS Mass flow controller (200.0 standard-state cubic centimetres per minute (sccm)) and an Apex fine mass flow controller (1.000 sccm) respectively. The GAS was connected to the

deposition (main) chamber through an orifice with 3 mm in diameter. The whole system was pumped down to $10^{-}5$ Pa as a base pressure by a turbo molecular pump (Pfeiffer TMU 261) supported by a scroll pump (Varian SH 110). A separate pumping system was not used for the present GAS. In this study, the pressure in the GAS was fixed at 100 Pa by adding 51 sccm argon flow to the aggregation chamber. An MKS Baratron (200 Pa) was used for monitoring pressure. The oxygen admixed in different steps was in the range of 0.010 to 0.060 sccm. A quartz crystal microbalance (QCM) was used for measuring the deposition rate during nanoparticle generation. It was placed in the main chamber, 6 cm away from the orifice of the GAS. For monitoring the oxygen concentration in the main chamber, a quadrupole mass spectrometer (Balzers Prisma QMS – QME200) was installed in a separate chamber differentially pumped by a turbo pump (Pfeiffer HiPace80) and connected to the main chamber via a tube and a variable valve. More details and the schematic sketch of the setup can be found in our previous paper [12]. To determine the size distribution of the TiO_x nanoparticles the transmission electron microscopy (TEM) using a FEI Tecnai F30 G2 (FEG, 300 kV) in scanning mode with a high-angle annular dark field detector (HAADF-STEM) was applied. The particles were deposited onto carbon coated copper grids. The chemical composition of the nanoparticle films has been investigated using a full lab XPS instrument manufactured by Omicron Nanotechnology GmbH operated with an Al anode at a power of 240 W.

3.4 Results and discussion

All experiments were started by running the magnetron discharge in a pure argon atmosphere for surface target pre-cleaning. After the cleaning process, a small amount of oxygen was added into the GAS and the deposition rate was recorded. In all cases due to the pre-cleaned target one observes initially a zero nanoparticle deposition rate. According to our previous works [10, 12], after a pre-cleaning procedure with pure argon, there is a completely clean target surface and also a Ti atoms are deposited on the walls. They will exhibit a large gettering effect. Thus not sufficient seeds for nanoparticle formation are formed and the deposition rate will be zero. After some time the Ti at the walls will be partially oxidized and TiO_x species will be formed on the target. Sputtering of the oxide components (TiO_x) formed on the target surface then provides the necessary seeds for the formation of TiO_x nanoparticles. Since the Ti target at this stage shows very little poisoning the sputter rate will be high allowing the nanoparticle rate to rise to an initial maximum. By subsequent formation and enlargement of poisoned areas on the target surface the number of sputtered Ti atoms and thus the rate of nanoparticle formation will descend. Thus, the deposition rate decreases after the maximum. In the first series of experiments the influence of the pulsing parameters (frequency and duty cycle) on TiO_x nanoparticle generation was studied while other parameters (such as pressure, power and admixed oxygen) were kept constant. The oxygen admixture and duty cycle are fixed at 0.055 sccm and 50%, respectively and three different frequencies are applied. For comparison, the t_{off} and the effective power through t_{on} are shown in Table 1, for the different examined repetition frequencies.

Table 3.1: *t_{off} and real effective power at t_{on} for different frequencies and stability of nanoparticle deposition at constant duty cycle and feeding DC power of 50% and 50 W, respectively. Stable conditions could only be reached at a certain repetition frequency.*

DC Power = 50 W, Duty Cycle = 50%

f(kHz)	t_{off}**(s)**	P_{eff}**(W)**	**Stable**
30	16.7	100	No
40	12.5	100	Yes
50	10	100	No

The results displayed in Figure 1. show some common features and some differences for the different frequencies. According to the results the nanoparticle production arrives at a stable region only by tuning the repetition frequency to 40 kHz. At lower frequency (30 kHz) one observes a steady increase of the deposition rate after having reached a maximum and a decay in between and at higher frequency (50 kHz) the deposition rate also increases up to a maximum but falls subsequently to 0. This indicates that just by applying the right frequency stable nanoparticle formation can be achieved.

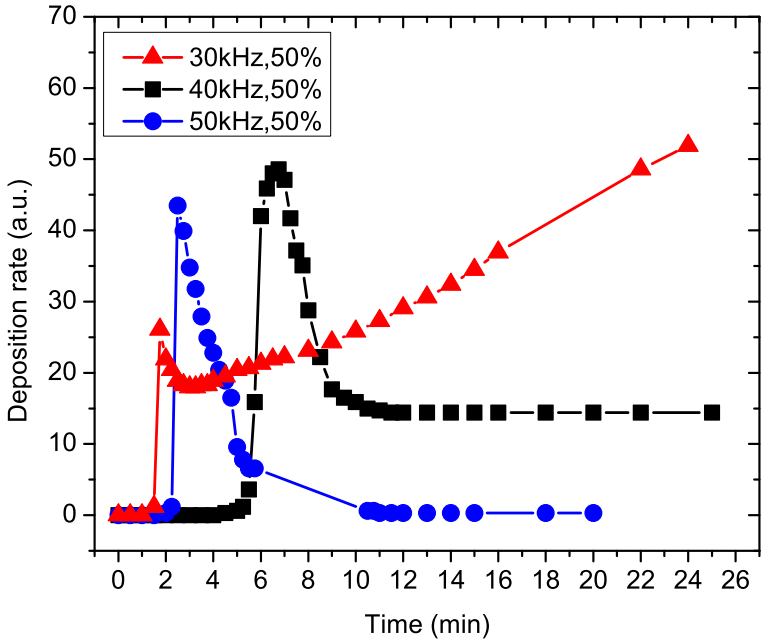

Figure 3.1: *Evolution of nanoparticle deposition at different frequency when the duty cycle as well as other operation parameters are kept constant (DC power = 50 W, F_{rmO_2} = 0.055 sccm, and duty cycle = 50%). Just at a certain repetition frequency (40 kHz) stable nanoparticle formation is achieved.*

Table 3.2: *Values of t_{off}, real effective power at t_{on} for different duty cycles and status of stabilization of nanoparticle deposition. The repetition frequency was 40 kHz, the input DC power and pressure were kept constant at 50 W and 100 Pa, respectively. At constant conditions, small changes (less than 10%) in duty cycle preserve the stable status, while a large variation leads to unstable deposition by disturbing the balance between poisoning and sputtering processes.*

DC Power = 50 W, f = 40 kHz

Duty cycle(%)	t_{off}**(s)**	P_{eff}**(W)**	**Stable**
40	15.00	125	No
45	13.75	111.1	Yes
50	12.50	100	Yes
55	11.25	90.9	Yes
60	10.00	83.3	No

At the lowest frequency (30 kHz) the time t_{off} will be longer (see Table 1) leading to a larger oxide area (and more oxide material is formed) on the target surface. In addition more material will be sputtered off at the also longer time t_{on}. This enhances the seeding process and nanoparticle generation in the next steps leading finally to the highest observed deposition rates of the three investigated frequencies. In addition the long t_{on} is sufficient to sputter not only away the oxide produced at last t_{off} but also to sputter from already cleaned parts of the target. While the clean sputtered Ti atoms act as getters for oxygen the subsequent oxidation process of the target will be less effective. Therefore the target surface will be increasingly cleaned with time. A cleaner Ti target leads to an increased amount of sputtered-off material which can enhance the growth process of the nanoparticles. As a consequence, the deposition rate continues to rise (Figure 1) but does not reach to a stable zone. At longer time, by providing an equilibrium between poisoning and sputtering processes a stable deposition will be expected.

When the applied frequency is set to 50 kHz the deposition rate increases first, but after reaching a maximum it falls to zero. At this frequency the t_{on} and t_{off} are quite short (Table 1) and apparently t_{on} is not long enough to completely sputter off the oxide components which were generated during the previous t_{off} on the target. Therefore after some cycles, the growing poisoned regions on the target decrease the sputtering yield and finally the rate of nanoparticle formation reaches zero due to dominant target poisoning. The continuous growing of magnetron bias voltage and then, after some minutes, the gradual blackout of the discharge confirm further this model.

In the next step, the effect of duty cycle on deposition rate was considered. Here the frequency was fixed at a value of 40 kHz where a stable deposition rate was found in the previous experiment. The values for t_{off} and the effective power during t_{on}, as well as the status of deposition rate stability for different duty cycles at fixed other experimental parameters (DC Power 50 W, repetition frequency 40 kHz, Ar pressure 100 Pa) are shown in the Table 2.

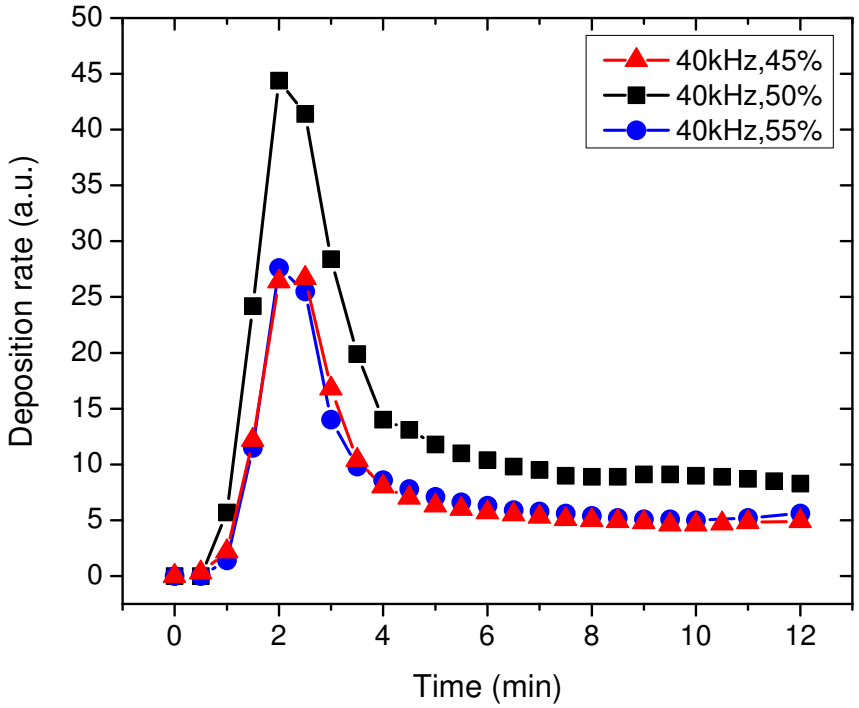

Figure 3.2: *Evolution of nanoparticle deposition for different duty cycles close to 50% at constant operation conditions (DC power = 50 W, P = 100 Pa, F_{O_2} = 0.055 sccm and frequency = 40 kHz). Small changes in the duty cycle lead to stable but always lower deposition rates compared to the optimum at 50% duty cycle.*

Large variations of the duty cycle will move the nanoparticle generation out of stable conditions for the same reasons as discussed before for the variation of frequencies. Again a non-equilibrium between the poisoning process and the sputtering process at t_{on} , causes unstable nanoparticle formation. Thus smaller variations of the duty cycle were tested and the results are displayed in Figure 3.2.

Small changes in duty cycle, in both directions away from 50%, lead to stable deposition but with a lower deposition rate. When the applied duty cycle is lower than 50%, the longer t_{off} enhanced target oxidation and results in components with a higher average oxidation state (higher average x values of TiO_x components). Simultaneously the energy density at t_{on} (Table 2) increases but remains low enough to provide a constant number of nanoparticle seeds originating from the more oxidized target. As will be discussed later, the consumed power for sputtering off the sub–oxide components from the target is increased by the increased target oxidation status. Therefore the lower number of available seeds reduces the nanoparticle formation rate to a lower value.

In opposite direction when the duty cycle is increased to 55% the shorter t_{off} decreases the adequately oxidized area on the target surface, while the higher duty cycle causes lower energy density at t_{on} (See Table 2). These factors also decrease the nanoparticle seed density not only by decreasing the sputtering yield due to lower effective power, but also by reducing

the ability of the impacting ions to convert a higher oxidized area to the optimum sub–oxide area on the target (this will be discussed in the next sections). Hence the nanoparticles deposition rate is again shifted to a lower value. In summary, at constant pulse period (constant frequency), small changes in duty cycle do not affect the stabilization status, but lead to lower stabilized deposition rates (Figure 3.2).

Since the deposition rate is measured by a QCM in terms of mass, higher deposition rates at 50% duty cycle (Figure 3.2) could be caused by formation of bigger nanoparticles and/or higher number of TiO_x nanoparticles. To clarify this issue TEM analysis of samples with collected nanoparticles were performed. The results showed that small changes in duty cycle did not influence the mean size of the nanoparticle distribution significantly. Thus, the small deviations in t_{on} and t_{off} do not affect the nanoparticle size. Furthermore higher deposition rates in the stable region at 50% duty cycle (for our present conditions) must be due to a higher number of nanoparticles caused by more intensive sputtering and thus more nucleation centres in the GAS.

The results of the next set of experiments on the evolution of the deposition rates at different oxygen concentrations are shown in Figure 3.3. A similar trend for all different used oxygen admixtures is observed where a broad tail appears after a sharp maximum. Again the maximum appears in some minutes after oxygen injection and subsequently the deposition rate arrives at the typical stable area (after about 15 min) where it remains relatively constant for quite long time.

As can be seen from Figure 3.3 increasing the oxygen flow leads to an appearance of the maximum of the deposition rate at earlier time. The same trend was found for conventional DC magnetron sputtering [12]. Furthermore in the pulsed power regime the amount of deposited material in the stable part also depends on the oxygen flow. Increasing the oxygen flow rate leads to a higher oxygen concentration in the GAS, hence more oxide compounds can be formed on the target. Subsequently, more material will be sputtered off at t_{on} and nanoparticle generation is enhanced by providing more seeds. Again, since the QCM measures only the mass of deposited material, the cause of the increased deposition rate is not exactly known, either it is due to an increased average size of the nanoparticle or to an increase of the number of nanoparticles. In later sections, we will reconsider this subject by a detailed analysis of the morphology of the prepared films. In Figure 3.4, the time evolution of nanoparticle deposition for two different discharge regimes (conventional DC and pulsed DC) are compared while the operation conditions are similar. As can be seen, there are two prominent advantages in the pulsed regime. While for conventional DC sputtering, the deposition rate descends to zero shortly after the maximum, it arrives at a non-zero stable part for the pulsed power and remains constant for a long time. Furthermore, a much higher deposition rate is obtained in the pulsed power regime. Understanding of these facts is possible by considering the TiO_x sputtering process and also the pulse signal characters. According to reported works [91, 102], a completely oxidized TiO_2 layer has the tendency to release oxygen under energetic ion bombardment and convert to a titanium sub–oxide layer. Therefore, because the applied energy is concentrated in a short time (t_{on}) in the pulsed power mode, not only the ion concentration is increased but also the ions can get higher acceleration and gain more energy in order to release more oxygen from the poisoned

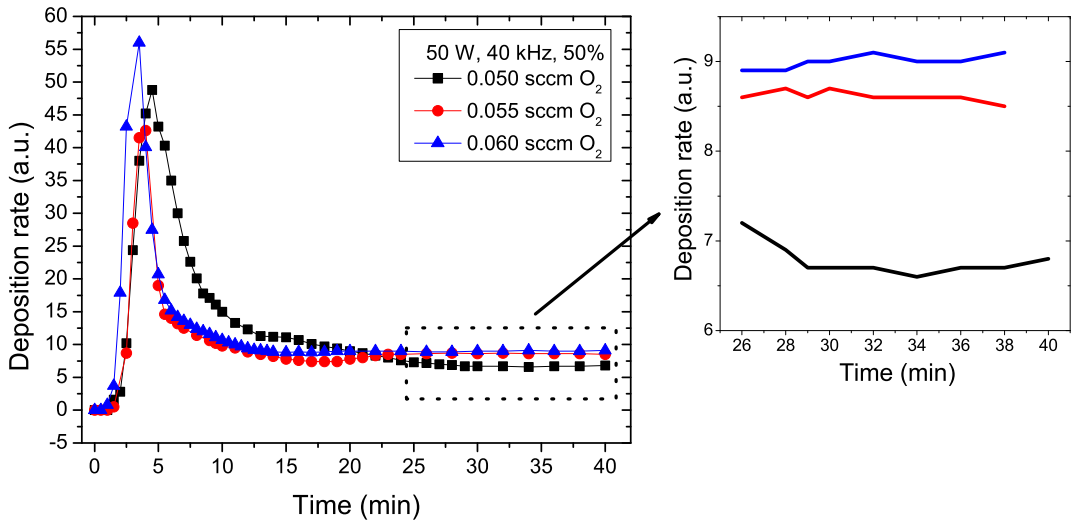

Figure 3.3: *Effect of different oxygen admixtures on nanoparticle formation at constant condition (power = 50 W, P = 100 Pa, frequency = 40 kHz and duty cycle = 50%). As can be seen from the right part (focused on stable regions), increasing the oxygen admixture enhances the nanoparticle deposition. Furthermore, due to accelerated poisoning of the target and of the Ti on the GAS walls the maximum of the deposition rate shifts to earlier time with increasing oxygen flow.*

regions of the target surface. Consequently, the sputtering rate will be enhanced in next steps. Hence in pulsed DC compared to conventional DC fully poisoned areas on the target surface have less chance to form or to remain there for a long time. More sputtered material provides more seeds components which enhance the clustering process in the GAS.

During the experiments, the escaped oxygen molecules (32 amu) from the aggregation chamber were monitored by a mass spectrometer. The signal of oxygen molecules confirms the oxygen consumption in the various stages of deposition (Figure 3.5). At the initial step of nanoparticle deposition, the oxygen signal does not show any variation, since all of the oxygen is consumed by metal atoms on the target surface, on the walls of GAS and also by off-sputtered metal atoms in the volume [12]. After the maximum of the deposition rate, but with a delay of some minutes, the O_2 signal starts to rise up while the deposition rate decreases. It seems that this delay is caused mainly by oxygen consumption at the target surface and at the GAS walls (gettering processes). Yet, after arriving at a stable deposition rate the O_2 signal continues to rise and finally saturates, indicating a constant oxygen consumption rate in the GAS (Figure 3.5). Apparently, in this region the oxygen attachment rate to the walls of the GAS decreases, because the oxygen density on the GAS walls gradually reaches a saturation condition, and then extra escaped oxygen from the GAS is detected by mass spectrometer [12].

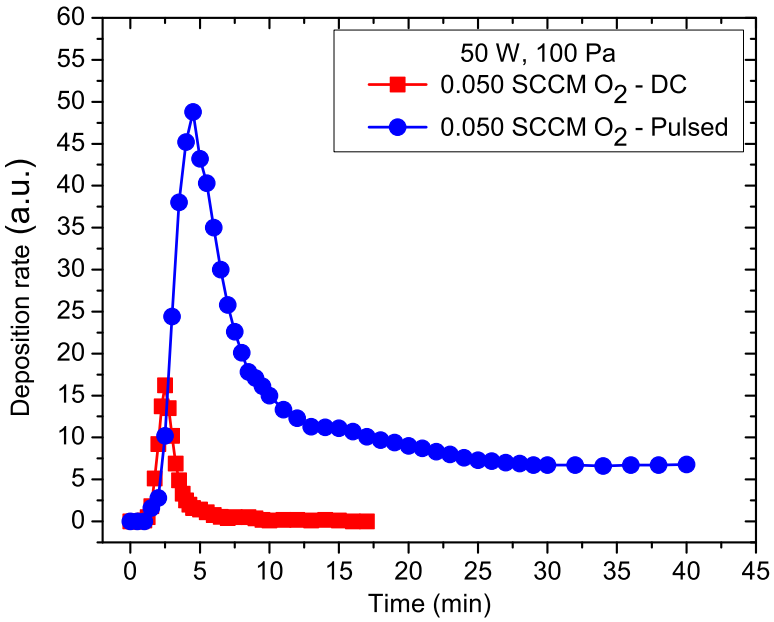

Figure 3.4: *Comparison of nanoparticle deposition rate evolution in the DC and pulsed DC regimes at similar operation conditions ($P = 100$ Pa, power $= 50$ W and $F_{O_2} = 0.050$ sccm, frequency $= 40$ kHz, duty cycle $= 50\%$)). The pulsed DC mode exhibits higher deposition rate and also quite stable nanoparticle production for a long time.*

For studying the processes in more detail, also the bias voltage of the magnetron was recorded. After oxygen injection the bias voltage rises but after a few minutes it levels off to a saturation value (see Figure 3.5). Afterwards it only shows a small increase. The increasing concentration of an oxygen which can absorb free electrons of the discharge as well as increase of target poisoning contribute to the bias voltage raise in the initial step [11]. Then by establishing a steady state of the nanoparticle formation process, the fraction of the poisoned area on the target will remain constant. Furthermore the feeding oxygen stream is fixed during experiment, therefore the bias voltage stays at an almost constant level (it only slightly increase due to the decrease of oxygen gettering processes at the GAS walls as discussed for the raise of the oxygen signal above).

XPS measurements were applied to determine the chemical composition of the nanoparticles formed in the GAS. To avoid exposure to atmosphere and subsequent oxidation of the nanoparticles the GAS was linked to the transfer chamber of the XPS device. This allows a sample transfer to the measurement chamber under UHV conditions. The nanoparticles were deposited onto a carbon coated silicon substrate. The prepared film was measured directly after deposition and transfer to the analysis chamber. Close analyses and deconvolution of the doublet Ti2p core level spectra (Figure 3.6 - left), show that the nanoparticles mainly (47%) consists of stoichiometric titanium dioxide, TiO_2 (459.0 eV) and the rest (47%) is assigned to TiO_x (457.2 eV, x $<$ 2) and TiC (455.2 eV) compounds. Around 6% is assigned

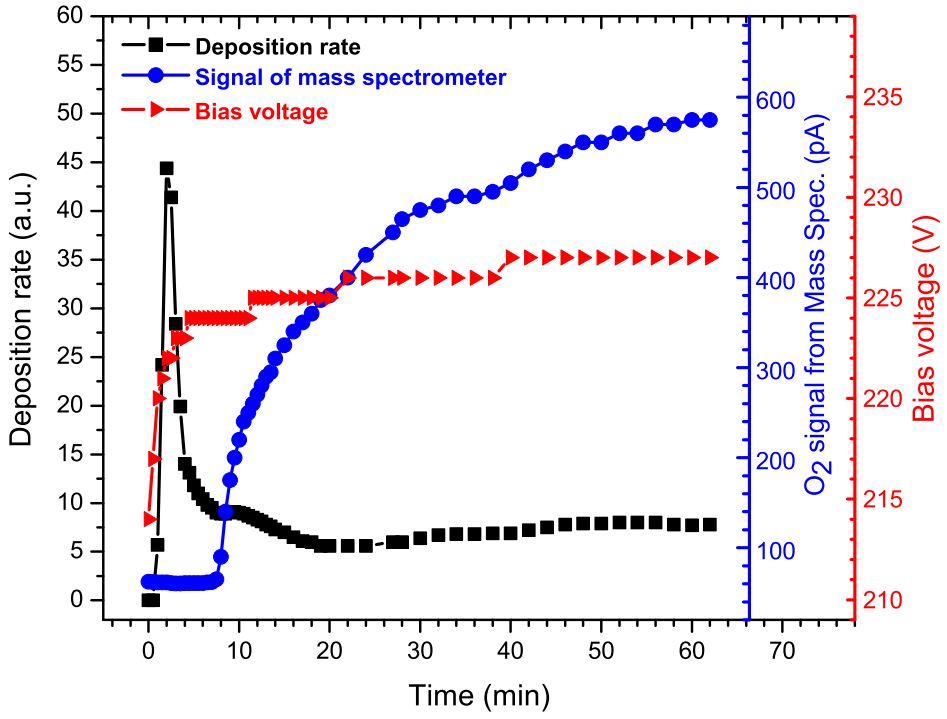

Figure 3.5: *Time evolution of the magnetron bias voltage as well as the oxygen molecule (32 amu) signal during nanoparticle deposition in the pulsed regime at constant oxygen flow (F_{O_2} = 0.055 sccm). Both parameters reach saturated values after an initial increase. The operating parameters were fixed as: P=100 Pa, DC power = 50 W, frequency = 40 kHz and duty cycle = 50%.*

to elemental Ti (454.1 eV), indicating that the admixed oxygen is not sufficient to completely oxidize all sputtered Ti atoms. It should be noted that after exposure to the open air the nanoparticles are mostly fully oxidized (around 90% of TiO_2) (See Figure 3.6 - right), what could be expected for small nanoparticles and was also observed by other researchers [103]. These results suggest that for pulsed magnetron sputtering sub–oxidized components (TiO_x) have the main contributions to Ti-based nanoparticle generation in the GAS. The influence of different oxygen admixtures and also pulsing parameters on the exact chemical composition of the nanoparticles will be an interesting topic for future investigations. Please, note that all XPS spectra were charge referenced to the aliphatic carbon at 285.0 eV and peak deconvolution is in agreement with the literature [103].

The nanoparticle size distribution for different oxygen admixtures was studied by TEM measurements, where the nanoparticles have been collected at the stable parts of the deposition rates. After analysis of the obtained TEM images two remarkable points could be found for the pulsed power regime. First, the nanoparticles show very narrow size distribution, especially at stable production conditions, with small standard deviation (less than

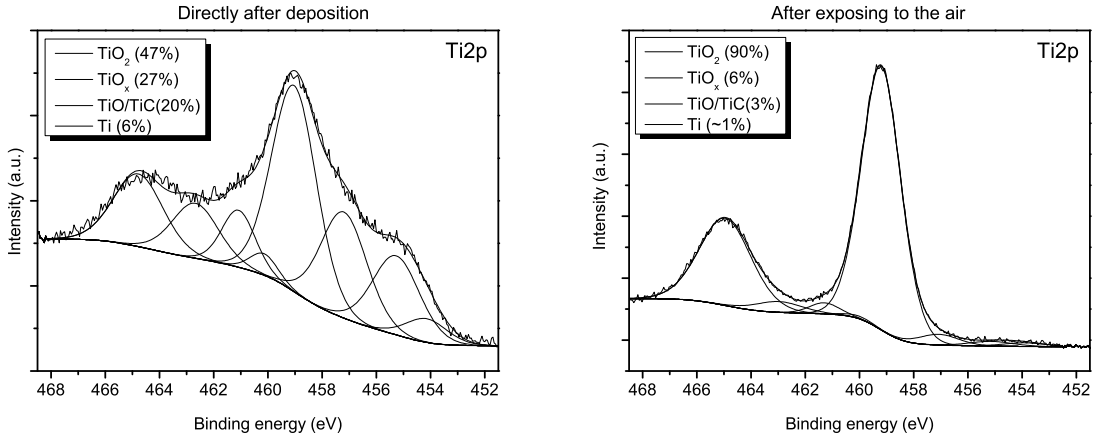

Figure 3.6: *High resolution Ti2p XPS spectra of TiO_x nanoparticle film prepared by GAS source connected to a dedicated chamber linked to the XPS transfer chamber. The samples were measured immediately after deposition without exposure to the open atmosphere (left) and after long time aging in the air (right).*

0.6 nm for an average size of 6.9 nm). It seems, that at the stable condition, due to the established stationary state between the various processes, the nucleation process for most of the nanoparticles starts from a small region close to the target and the particles pass a similar evolution in the GAS. Thus they can produce a quite narrow distribution.

The crucial influence of oxygen concentration on the size of the nanoparticles is the second point. As can be seen from Figure 3.7 , the mean size of the nanoparticles increases by increasing the admixed oxygen flow. This means that, by this approach, the size of the nanoparticles can be controlled by tuning the oxygen admixture at typical conditions. This observation can be explained by the role of oxygen in the surface oxidation process at steady state conditions. An increased oxygen concentration causes oxidation of more material on the target (not only the covered area but also the depth of oxide layer on the target increases) at t_{off}. Subsequently at t_{on}, more oxide components, which play the main role in the clustering processes, can be sputtered off, creating more seeds and accelerating the cluster growth process. Furthermore, by increasing the binding energy of the obtained compounds reaction with Ti atoms is much enhanced [10, 11]. Thus oxygen containing species can enhance the cluster nucleation and growth process. The contribution of each process is not clear yet and more investigations are necessary.

To analyse the size change of the nanoparticles during the time evolution of the deposition rate one TEM sample was prepared near the initial maximum of the deposition rate (Figure 3.7(c)). The size distribution of the nanoparticles at this condition is broader than in the stable part (See Figure 3.7(b)) but the mean size is similar. At this condition, due to the pre-cleaning process several forms of sputtered Ti atoms and compounds are available in the volume which have potential for cluster nucleation after reaction with oxygen. Therefore

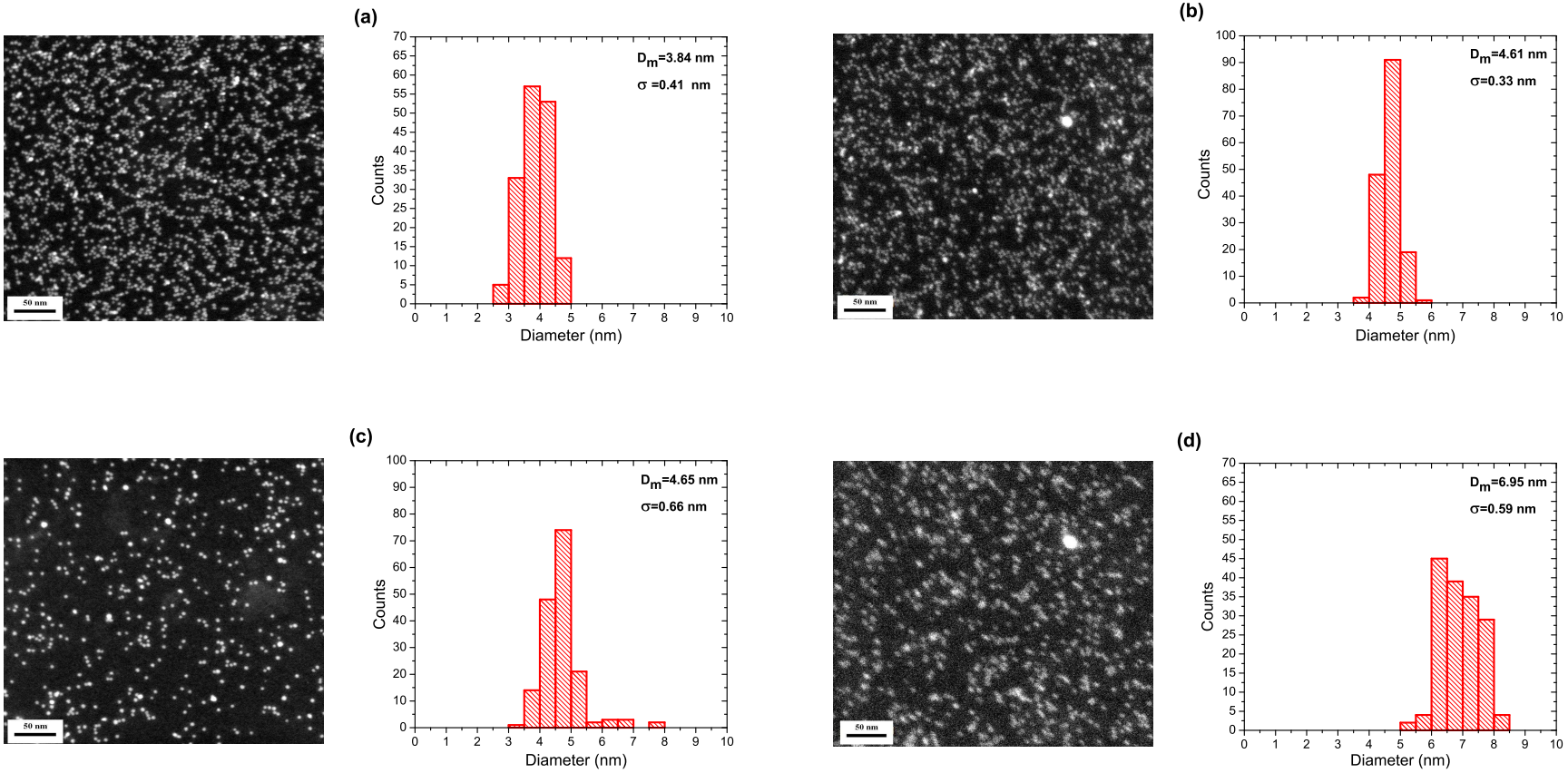

Figure 3.7: *TEM images and size distributions with standard deviations showing a narrow size distribution of TiO_x nanoparticles deposited on carbon coated copper grids in the stable part of the deposition rate for different oxygen admixtures. a) F_{O_2} = 0.050 sccm, b) F_{O_2} = 0.055 sccm (in stable part), c) F_{O_2} = 0.055 sccm (at maximum), d) F_{O_2} = 0.060 sccm. Other operation conditions were kept constant (power = 50 W, frequency = 40 kHz, duty cycle = 50%, P =100 Pa). One notes that by increasing the amount of admixed oxygen the nanoparticle distribution shifts to the bigger sizes.*

depending on the initial position of the nucleus centres in the GAS, the residence time (and growth evolution) of the nanoparticles in the GAS are significantly dissimilar leading to a broader size distribution.

In other words, at the beginning, both nanoparticle seeding processes (volume seeding and target seeding) are important, while in the stable part (with a reduced number of seeds in the volume) seeding via the target is the dominant mechanism and volume seeding is a minor factor in cluster growth. Therefore in the stable part, the nanoparticle deposition rate is lower than at the peak but the size distribution is quite narrow.

In Figure 3.8 the variation of nanoparticle size versus admixed oxygen flow is depicted. By increasing the admixed oxygen in a very narrow oxygen flow range from 0.04 sccm to 0.06 sccm the size rises almost exponentially. A reasonable explanation for this trend which can be used for tailoring the nanoparticle size is unknown yet.

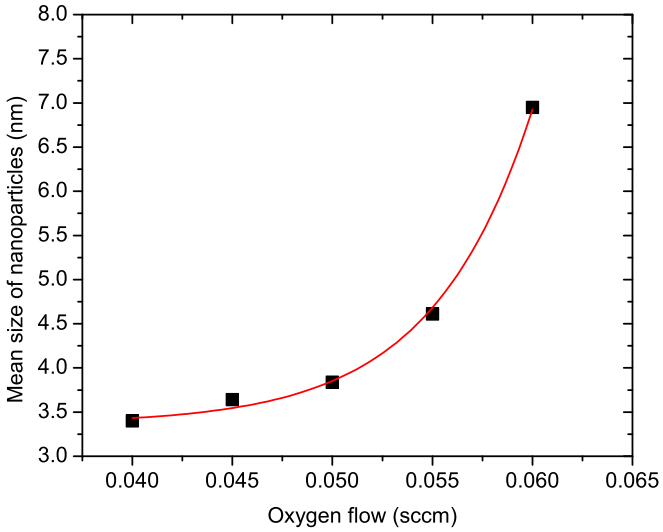

Figure 3.8: *Evolution of the nanoparticle size by oxygen admixture, fitted by an exponential curve (red), when the operation parameters were fixed (see caption of Figure 3.7). The dependence is almost exponential allowing to tailor the nanoparticle size by the oxygen flow.*

Using the mean size of the nanoparticles formed at each oxygen flow, the mean mass of the nanoparticles can be estimated easily. On the other hand, the recorded deposition rate for each oxygen admixture (Figure 3.3) is proportional to the rate of the deposited mass for all nanoparticles in the stable part. Detailed analysis shows that increasing the admixed oxygen decreases the number of nanoparticles generated by the GAS. In other words, more oxygen injected into the GAS by increasing the sputtered oxide compounds improves the agglomeration process leading to bigger nanoparticles. Higher agglomeration could be caused by a change in the composition of the nanoparticle seeds due to the larger oxygen flow and the resulting increase in the growth rate (and coalescence rate) of the nanoparticles is a possible reason for that observation. This also explains the slight increase

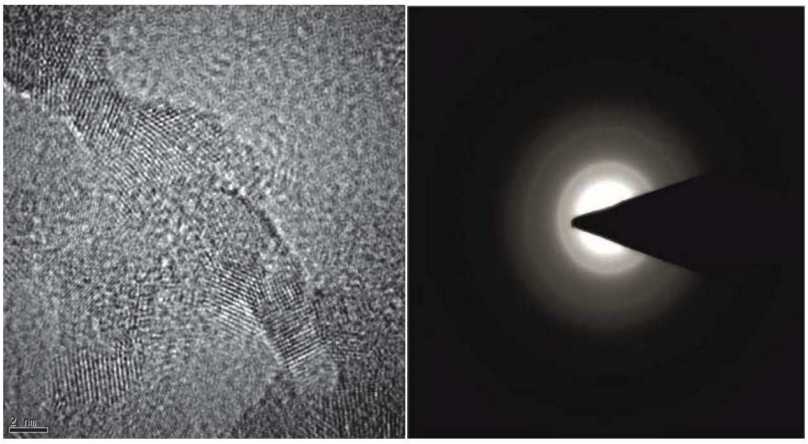

Figure 3.9: *HRTEM image (left) and electron diffraction pattern (right) of TiO_x nanoparticles deposited by GAS at typical conditions.*

of the deposition rate. To fully clarify the role of the varying reactive gas admixtures on nanoparticle formation and growth processes requires more investigations on the chemical compositions of the nanoparticles.

In order to analyse the crystallographic structure of prepared nanoparticles, high resolution transmission electron microscopy (HRTEM) was applied. HRTEM micrograph and selected area electron diffraction (SAED) pattern for TiO_x nanoparticles prepared by GAS at typical conditions are shown in Figure 3.9. The very faint diffraction rings are due to the nanocrystalline nature and the low amount of material. The positions of the rings are signs that the particles have brookite structure but we cannot exclude the presence of rutile and anatase. The coexistence of brookite, anatas and rutile in nanocrystalline material is well known and reported before in the literature [100]. So, individual nanoparticles have crystalline structure. However, XRD measurement (Figure 3.11) of TiO_x nanoparticles film, with thickness around 4.5 μm, shows the amorphous structure of the as-deposited film and only after annealing at 650 ^{0}C for 1 hour, anatase and rutile structure can be observed, further supporting the view that more than one phase is present.

As a general summary, at typical operation conditions (pressure and feeding power), the nanoparticle generation is possible only under certain windows for pulsing parameters and reactive gas admixtures (as schematically shown in Figure 3.10). Furthermore for stabilizing the nanoparticles production for long term, the pulsing parameters and reactive gas admixture should be chosen from narrow windows, as to provide (and then sustain) an equilibrium between poisoning and sputtering mechanisms.

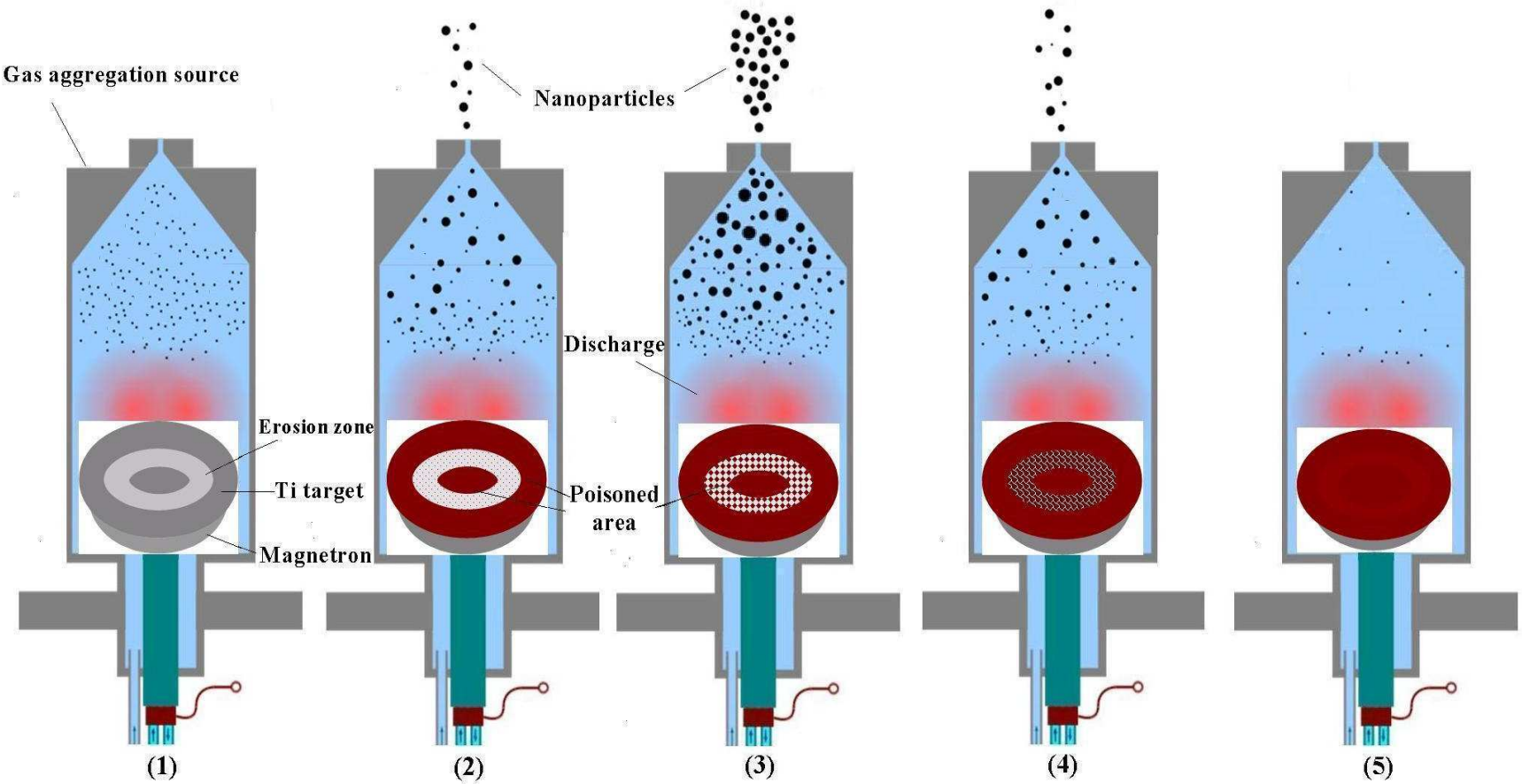

Figure 3.10: *Without reactive gas (case 1) as well as at highly poisoned target (case 5) nanoparticle formation is impossible in gas aggregation source. Only under certain parameters which lead to sub–poisoned area on active zone of the target (erosion zone) nanoparticle formation will occur (cases 2, 3 and 4). Additionally when a balance between poisoning and sputtering processes is established, a stabilized nanoparticle formation was detected with mostly monodisperse size distribution (case 3).*

3.5 Conclusions

We used pulsed DC power for generating TiO_x nanoparticles by magnetron sputtering at constant pressure (100 Pa). By applying a steady stream of admixed oxygen as a reactive gas, the different conditions for stable production of TiO_x nanoparticles from an aggregation source were investigated. The influence of the pulsing parameters (frequency and duty cycle) as well as the oxygen admixture on nanoparticle generation and the governing processes were studied in detail. Our experimental results reveal that a constant rate of stable nanoparticle production at typical operation conditions can only be achieved at certain pulsing parameters. Using pulsed DC power at these parameters does not only lead to a higher nanoparticle deposition rate compared to conventional DC power but also to stable deposition. Furthermore, the size distribution of the produced nanoparticles is remarkably narrow and affected by the reactive gas admixture in GAS. Analysis of the chemical composition of the nanoparticle films by XPS directly after deposition (without air aging) proves that sub–oxide components have the main contribution in the nanoparticle formation process in the GAS, while the film will turn to almost fully oxidized after air exposure. Considering the variation of the oxygen molecule concentration, obtained by mass spectrometry, and the evolution of the bias voltage of the magnetron confirmed our model on the dominant mechanisms of nanoparticle formation in the pulsed DC power regime.

3.6 Acknowledgements

This work has been supported by the German Research Foundation (DFG) within the framework of the Collaborative Research Center SFB TR 24, subproject B13. One of authors (A.M.Ahadi) is grateful to the Iran Ministry of Science for financial support. We would also like to thank Stefan Rehders for the technical construction of the cluster source.

3.7 Suppelmentary

TiO_x nanoparticles were deposited on Si substrate and XRD measurement was performed. The amorphous structure of the as–deposited film was observed. However, after annealing in the air at 650 ^{0}C for 1 hour, anatase and rutile structures were detected.

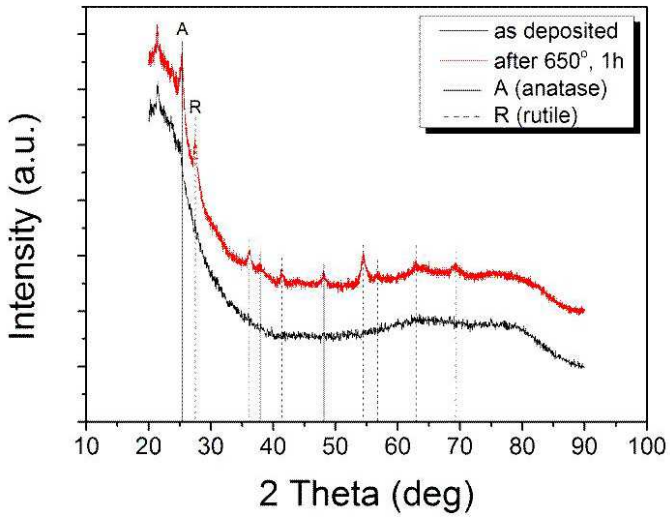

Figure 3.11: *XRD measurements TiO_x nanoparticles film prepared by gas aggregation source. The measurement was performed before and after sample annealing at 650 ^0C for 1 hour. The thickness of the film is 4.5 μm. Anatase (solid vertical lines) and rutile (dashed vertical lines) structures were observed after annealing.*

Chapter 4

Characterization of a radio frequency hollow electrode discharge at low gas pressures

Amir Mohammad Ahadi,[1] Thomas Trottenberg,[2] Stefan Rehders,[1] Thomas Strunskus,[1] Holger Kersten,[2] and Franz Faupel[1]

[1]Institute for Materials Science – Multicomponent Materials, University of Kiel, 24143 Kiel, Germany

[2]Institute of Experimental and Applied Physics, University of Kiel, 24098 Kiel, Germany

4.1 Abstract

An RF hollow discharge configuration is presented that makes use of a combination of RF plasma generation and the hollow cathode effect. The system was especially designed for the treatment of nanoparticles, plasma polymerization and nanocomposite fabrication. The process gas streams through the plasma in the inner of the cylindrical electrode system. In the here presented measurements, pure argon and argon with oxygen admixtures are exemplarily used. The discharge is characterized by probe measurements in the effluent, electrical measurements of the discharge parameters, and visual observations of the plasma glow. It is found that the RF fluctuations of the plasma potential are weak. The plasma potential resembles the one of a DC hollow cathode discharge, the RF hollow electrode acts as a cathode due to the self-bias, and a high voltage sheath forms in its inner cylinder.

4.2 Introduction

Radio frequency (RF) discharges are a common tool for materials processing, such as etching, thin film deposition, and surface modification. Due to the high voltage plasma sheath arising in RF discharges, energetic ions are created, which are important, e.g., for etching processes in the fabrication of micro chips. The robustness of RF discharges against variations in the gas composition enables an enormous freedom in the use of active chemical components and radicals, which can be created in the discharge from admixed precursors [104]. RF discharges usually apply a parallel plate setup or at least one plane electrode with the vacuum chamber as grounded counter electrode.

Hollow cathode (HC) discharges are different in many aspects. Not only are they direct current discharges (DC), but also the geometry usually is cylindrical, which is untypical for RF discharges. The first reference to a hollow cathode, at least to our knowledge, describes an experiment carried out almost a hundred years ago [35]. Paschen and Bartels observed that cylindrical cathodes can produce a very intense glow, which they were able to use for spectroscopy of a very weak helium emission line. Since those days, this kind of discharge has continuously been studied, and the hollow cathode effect with "pendulum electrons" was identified to be responsible for the high plasma densities [32, 105–108]. During the past decades, hollow cathodes became an often used technique in a wide field of applications, which can be attributed to the high plasma densities that can be achieved with this kind of discharge. Today, HC discharges are used for physical vapor deposition [109], vacuum coating [110], surface modification [111], cold cathode fluorescent lamps, e.g. display backlights, [112], electron sources [113], e.g. neutralizers in electric spacecraft propulsion [114], and ion sources [115, 116].

The utilization of the hollow cathode effect for radio frequency discharges is still uncommon. Horwitz used two electrically connected, closely spaced parallel plate RF electrodes and found that an intense discharge forms between them [117]. This setup, that was used for high-rate reactive sputter etching, provided, just like in a hollow cathode, an electrostatic mirror for pendulum electrons, which explained the high ionization rates and plasma densities. Later, Horwitz et al. used similar RF hollow electrode setups for etching and amorphous silicon deposition [118], as well as multiple deposition and etch processes with silicon, polymers and metals [38]. Lejeune et al. applied the cylindrical form of an RF hollow electrode for the plasma generation in a broad beam ion source. Actually, the powered RF electrode consisted in this case of an arrangement of 19 tubes with individual diameters of 38 mm [119]. Typical for all of these works is that the RF discharges could be operated at gas pressures significantly lower than the commonly used pressures for DC hollow cathode discharges [120]. Comprehensive reviews on RF hollow electrode discharges until the end of the 1990th were written by Bárdoš [37, 121]. Since then, a variety of discharge geometries was applied, e.g. for large area surface treatment [39].

In this work, we present an RF hollow discharge setup that was especially designed for the treatment of nanoparticles, plasma polymerization and nanocomposite fabrication. The nanoparticles are planned to be transported by a gas flow through the hollow electrode

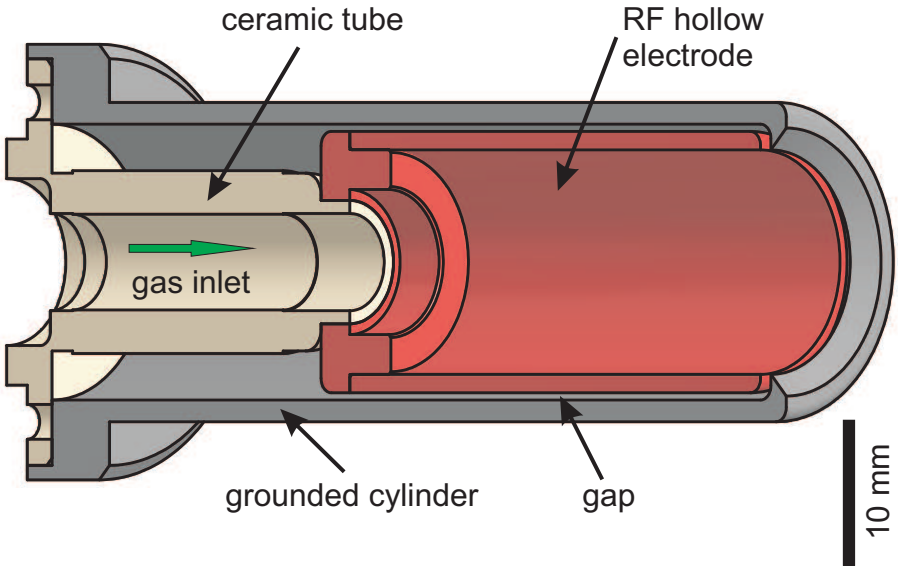

Figure 4.1: *Cutaway drawing of the hollow electrode assembly.*

in order to be treated by the plasma. Such experiments will be published in a forthcoming paper, while this article describes the setup and characterizes the discharge. For this purpose, probe measurements in the effluent of the hollow electrode and electrical measurements of the discharge parameters are performed as well as visual observations of the plasma glow. For the first investigations, pure argon plasma is used. However, since reactive gas admixtures and negative ions are expected to play an important role in our future work [12], we present first results of measurements with admixtures of oxygen, too.

4.3 Experimental Setup

The experimental setup was designed for nanoparticle processing as well as plasma polymerization and nanocomposite fabrication. For these purposes, the RF electrode system was implemented for an operation at low pressures from 1 to 20 Pa. Figure 4.1 shows the hollow electrode system. The RF electrode is a stainless steel cylinder with an inner diameter of 15.5 mm and a length of 36 mm. It has a short narrowed back end connected to a 20.5 mm long ceramic tube. This electrode and the ceramic tube are surrounded by another grounded metal cylinder. A small hole in the outer cylinder wall enables the RF feed line to be connected to the inner cylinder. The inner cylinder is separated from the outer one by a 0.5 mm gap. The front end of this grounded cylinder is bent inwards up to the inner radius of the RF electrode and is beveled at the outside. The grounded cylinder is intended to act as a counter electrode for the discharge. The electrode unit was installed in a cylindrical vacuum chamber (reactor chamber) with a diameter of 250 mm and a length of 525 mm. Before operation, the vacuum system is pumped down to a base pressure of 10^{-5} Pa.

Argon and oxygen are used as working gas and reactive admixture gas, respectively. The flow rate of argon is in the range of 70 to 116 sccm and the oxygen flow rate is in the

range of 0 to 30 sccm. Both gases are injected from behind the hollow electrode unit, so that the gas streams through the hollow electrode into the reactor chamber. The flow rates of the gases are independently controlled by a 200 sccm mass flow controller (MKS Instruments, Inc.). The experiments are performed at working pressures in the range from 1 to 20 Pa. The pressure is measured by a gas type independent capacitance manometer flange-mounted to the reactor chamber.

The RF voltage is provided by an RF generator (Cesar 136 from Dressler HF-Technik GmbH) operating at 13.56 MHz via a matching network, and the current-voltage characteristic is monitored by a voltage, current and phase angle measurement system (Octiv VI probe from Impedans Ltd.) between the vacuum feed through and the match box. This electrical setup allows to measure simultaneously the real (effective) RF power, the discharge current and voltage, the impedance of the discharge and the phase angle between voltage and current. Therefore, the RF power values given in this article are measured with the impedance measurement system instead of reading the power gauge of the RF generator.

Probe diagnostics is a challenge due to the small size of the plasma and the involved inhomogeneity. We built two different cylindrical Langmuir probes, each one has a tungsten tip with a length of 3 mm and a wire diameter of 0.1 mm at the end of a thin ceramic tube. One of the probes is equipped with an additional passive RF compensation which uses a floating pickup probe connected via a capacitor to the probe tip [42, 122, 123]. In our experiments, the pickup probe was a small elongated tungsten wire loop (about 2 cm long) at the end of another thin ceramic tube parallel to the first one (see Fig. 4.2); the loop was small enough to fit into the visible glow of the effluent plasma. The signal from the compensated probe is filtered at the RF frequency and its first harmonic. The compensated and the uncompensated probe are alternatively placed about 12 mm in front of the electrode unit at its symmetry axis. We want to point out that the measured plasma parameters refer to the effluent plasma and not to the bulk plasma in the hollow electrode, where a probe would strongly disturb the discharge.

4.4 Measurements and discussion

4.4.1 Probe measurements

The first measurements consist of a comparison between probe characteristics recorded with the uncompensated Langmuir probe and the RF compensated probe and aim at a better understanding of the hollow electrode RF discharge. In hollow cathode DC discharges, most of the discharge voltage appears as the voltage drop across the cathode fall, i.e. between the plasma bulk cylinder and the hollow cathode, and consequently the plasma potential is only a few $k_B T_e/e$ above the anode potential, where k_B is Boltzmann's constant and e is the elementary charge.

Figure 4.3 displays characteristics of alternative measurements with the two probes at the fixed pressure $p = 2\,\mathrm{Pa}$ and the fixed RF power $P_{RF} = 11\,\mathrm{W}$. The surprising result

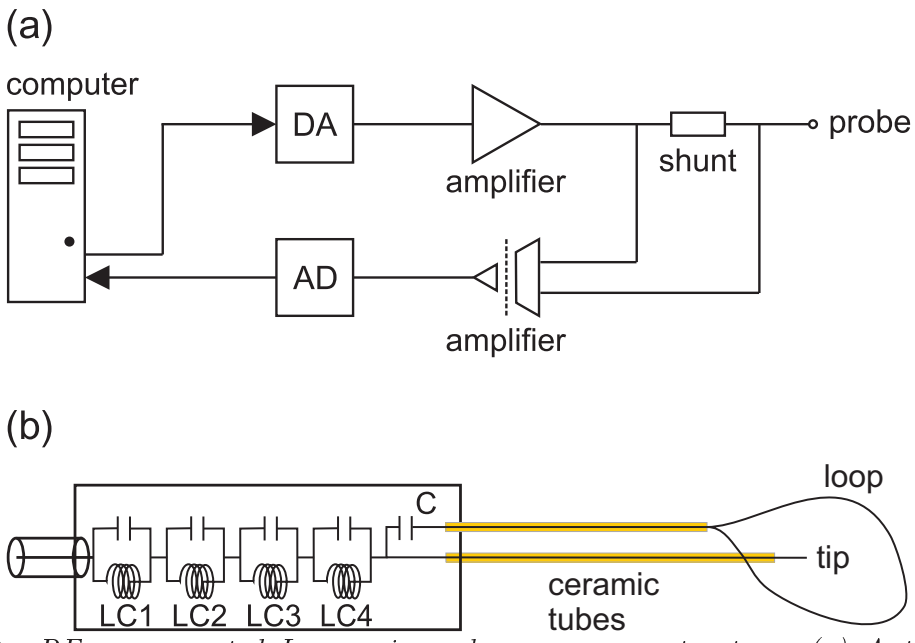

Figure 4.2: *RF compensated Langmuir probe measurement setup. (a) Automated data aquisition circuit for probe characteristics consisting of a shunt for the measurement of the probe current, amplifiers, and digital–analog conversions components (DA and AD). (b) RF compensation by means of a floating wire loop capacitively coupled (via the capacitor C) to the the probe tip and anti-resonant circuits (LC1 to LC4) for choking the RF frequency and its first harmonic.*

is that the RF compensation has not much influence on the characteristics. In plasmas with significant RF potential oscillations, one would expect a flattened characteristic in case of the uncompensated probe and apparently higher electron temperatures [41]. The evaluation of the electron temperatures from the logarithmic plots of the characteristics yields $k_\mathrm{B}T_\mathrm{e} = 3.5\,\mathrm{eV}$ for the uncompensated and $k_\mathrm{B}T_\mathrm{e} = 3.6\,\mathrm{eV}$ for the RF compensated probe, and expresses the similarity of the shapes of the two characteristics. The plasma potentials, determined as the voltages of maximum slope of the characteristics, are $\Phi_\mathrm{p} = +27.0\,\mathrm{V}$ and $\Phi_\mathrm{p} = +26.3\,\mathrm{V}$, respectively. Furthermore, the calculated densities are $n_\mathrm{e} = 5.9 \times 10^{15}\,\mathrm{m}^{-3}$ and $n_\mathrm{e} = 4.8 \times 10^{15}\,\mathrm{m}^{-3}$, respectively. The fact that the RF compensated probe measures a smaller density could be attributed to the higher disturbance due to the wire loop around the probe tip which causes plasma losses, but is anyhow within the expected error of 20 percent for the absolute value of electron density measurements.

From this finding, we conclude two important features: Firstly, the plasma potential seems to exhibit only small RF fluctuations in comparison to $k_\mathrm{B}T_\mathrm{e}/e$, which is a requirement for essentially undistorted probe characteristics [123]. Secondly, the discharge voltage drops predominantly across the sheath at the inside of the hollow RF electrode, akin the cathode fall in the DC hollow cathode discharge.

This picture agrees with the visible impression: the discharge occurs in the hollow electrode (and not around the grounded tip of the electrode assembly), which requires a high voltage RF sheath in the cylinder. In our case, direct measuring of the bias voltage showed

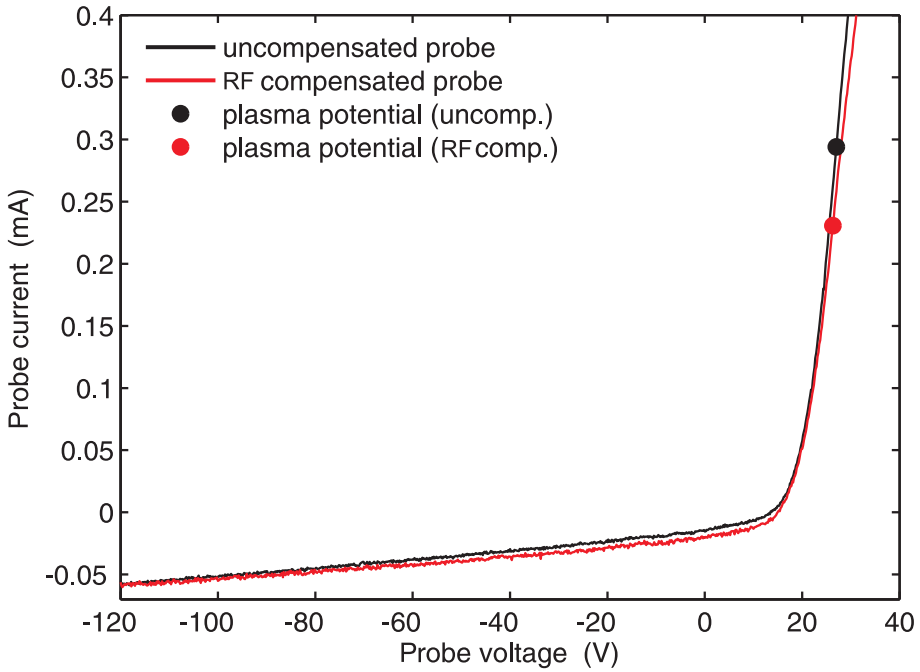

Figure 4.3: *Characteristics obtained by the uncompensated and the RF compensated Langmuir probe in the effluent plasma at RF power $P_{\mathrm{RF}} = 11\,W$ and pressure $p = 2\,Pa$. The markers show the respective inflection points, which indicate the plasma potentials.*

that the (negative) bias voltage is always 7 to 8 V smaller than the effective value of RF voltage. This indicates that the hollow electrode has a strong RF (i.e. high-voltage) sheath, where most of the discharge voltage drops. Lafleur and Boswell performed particle-in-cell simulations of similar RF discharge geometries (slab instead of cylinder) and found that only with the help of ion produced secondary electron emission the plasma penetrated deeply into the cavity [124]. These secondary electrons, which are produced by ion impacts at the inner walls of the hollow electrode, get accelerated across the sheath to very high energies, are trapped in the cavity, and provide, as pendular electrons, the necessary ionization for a high plasma density.

From these observations, we conclude that the potential resembles the one known from DC hollow cathode discharges: Here, the RF electrode acts as a cathode, the (grounded) counter electrode acts as an anode, and the major part of the discharge voltage drops at the sheath in the inner region of the "hollow cathode". These results open the opportunity to modify nanoparticles in this discharge configuration in a similar way as in DC devices [111].

Figure 4.4 compares measurements of the electron density and the electron temperature obtained with and without RF compensation at different powers. The equivalence of both techniques is confirmed within the typical accuracy of probe measurements [125]. Therefore, the use of RF compensation is dispensable, and the following probe measurements are performed with the uncompensated Langmuir probe.

By increasing the feeding power, more energy is transferred to the plasma electrons, the ionization increases [31,111], and, as a result, the production-loss balance shifts to higher

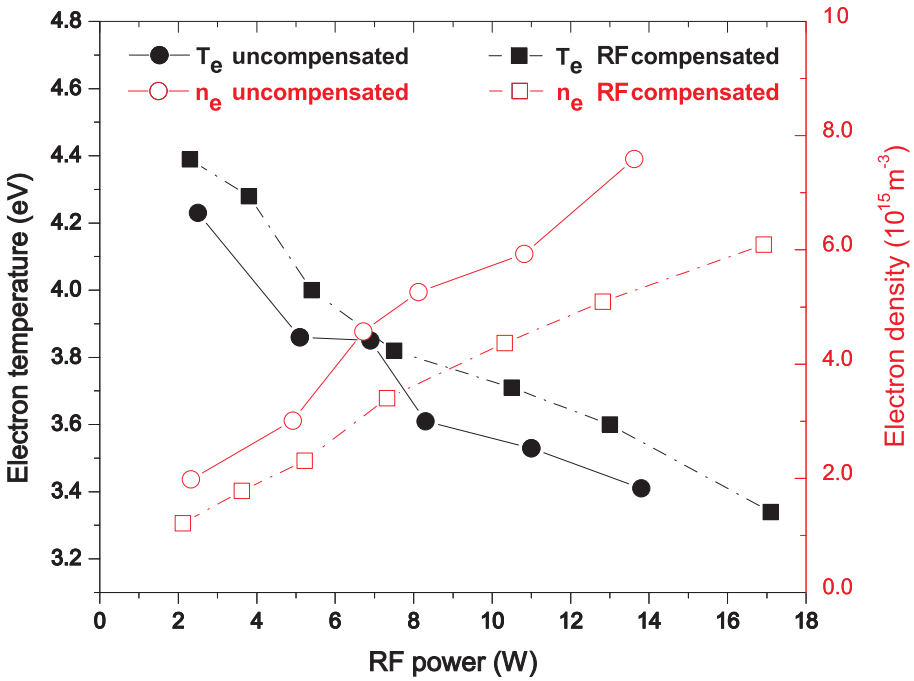

Figure 4.4: *Variation of electron temperature and density with RF power obtained by the uncompensated and the RF compensated Langmuir probes in the effluent plasma at the constant pressure $p = 2\,Pa$.*

plasma densities.

In the next step, the discharge power was fixed at $P_{\mathrm{RF}} = 7\,\mathrm{W}$, while the gas pressure is increased from $p = 1\,\mathrm{Pa}$ to $p = 15\,\mathrm{Pa}$. Figure 4.5 shows the typical behavior often found in RF discharges [123]: At higher pressures, the electron density is higher than at lower pressures. This can be understood from an enhanced ionization frequency and reduced ambipolar diffusion to the walls. At the same time, the increased electron-neutral collision frequencies at higher gas pressures reduce the electron temperature.

Concluding, we want to mention again, that the electron temperatures and densities were measured in the effluent plasma, and that the absolute values in the bulk plasma may differ from these ones.

4.4.2 Measurements of discharge parameters

In the following, measurements of voltage V and current I (effective values, i.e. roots of the mean squares), phase angle φ between voltage and current, and discharge impedance Z are presented and discussed. The power P_{RF} is calculated from the effective values and the phase angles. Figures 6(a) and 6(b) show the behavior of these quantities at a fixed pressure ($p = 2\,\mathrm{Pa}$) for the range of mean RF powers $P_{\mathrm{RF}} = (2 \ldots 16)\,\mathrm{W}$. One notices that the increase of the power by a factor of eight is not only a result of the increasing voltages and currents, but also due to the decreasing phase angles, which means that the discharge

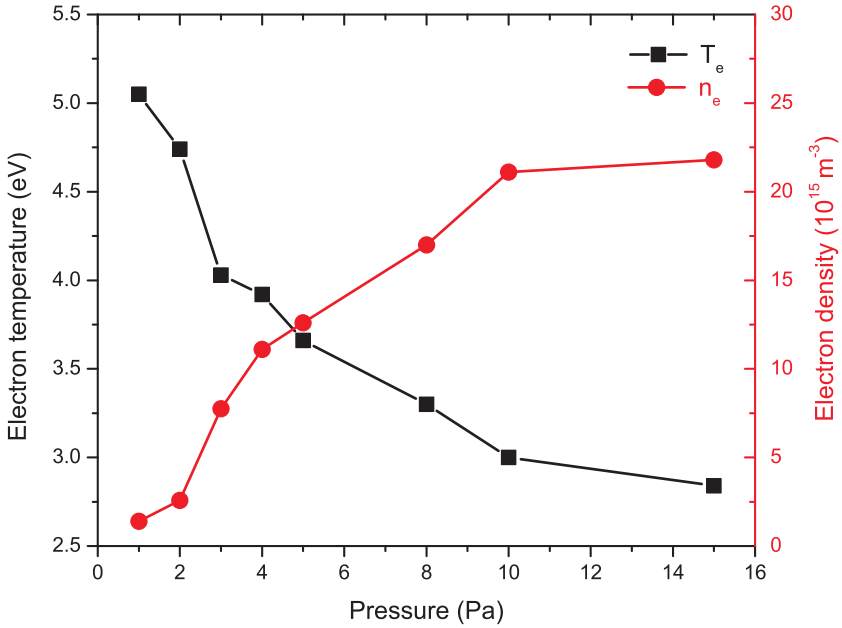

Figure 4.5: *Variation of electron temperature and density with gas pressure obtained by the uncompensated Langmuir probe in the effluent plasma at the constant RF power* $P_{\mathrm{RF}} = 7$ *W.*

becomes slightly more resistive and more power is dissipated.

The change in the power factor $\cos\varphi$ covers a range from 1.4 percent to 2.5 percent, as can be seen in Figure 4.6(c). The impedance, which is the complex sum of resistive (real) and reactive (imaginary) parts, slightly decreases as the power increases, but remains in the narrow range of $Z = (116 \ldots 119)\,\Omega$ [see Fig. 4.6(b)]. Consequently, there must be an absolute increase of the resistance as the power increases; this increase of the real part of the impedance turns the phase angle to smaller values. The physics of the increasing resistivity can be understood considering two different power dissipation channels in the discharge, following the model presented in Refs. [126, 127]: on the one hand, the collisional and stochastic electron heating in the plasma, and on the other hand, the acceleration of ions by the (time averaged) electric field in the sheath. While the electron heating is approximately proportional to the discharge current, the ionic losses in the sheath increase faster than the square of the current increases. This behavior of the resistivity becomes clear by a plotting $V\cos\varphi$, which is the ohmic (or resistive) component of the discharge voltage V, versus discharge power, shown in Figure 4.6(d): the resistance is higher for the higher RF powers and currents, it is almost proportional to the discharge power.

Also the gas pressure influences the electrical characteristics of the hollow RF discharge. Figures 7(a) and 7(b) show the measured quantities for a fixed RF power ($P_{\mathrm{RF}} = 7\,\mathrm{W}$) and the range of gas pressures $p = (1 \ldots 15)\,\mathrm{Pa}$. Also in this case, the behavior is similar to well-known RF discharges [127]. The discharge current decreases as the pressure increases due to the increasing electron-atom collision frequency. The discharge voltage varies synchronously, almost proportionally, to the discharge current, and, accordingly, the impedance remains in the narrow range of $Z = (108 \ldots 117)\,\Omega$. However, the power factor $\cos\varphi$ compensates for the decreasing product VI, as can be seen in Figure 4.7(c), and maintains the fixed power

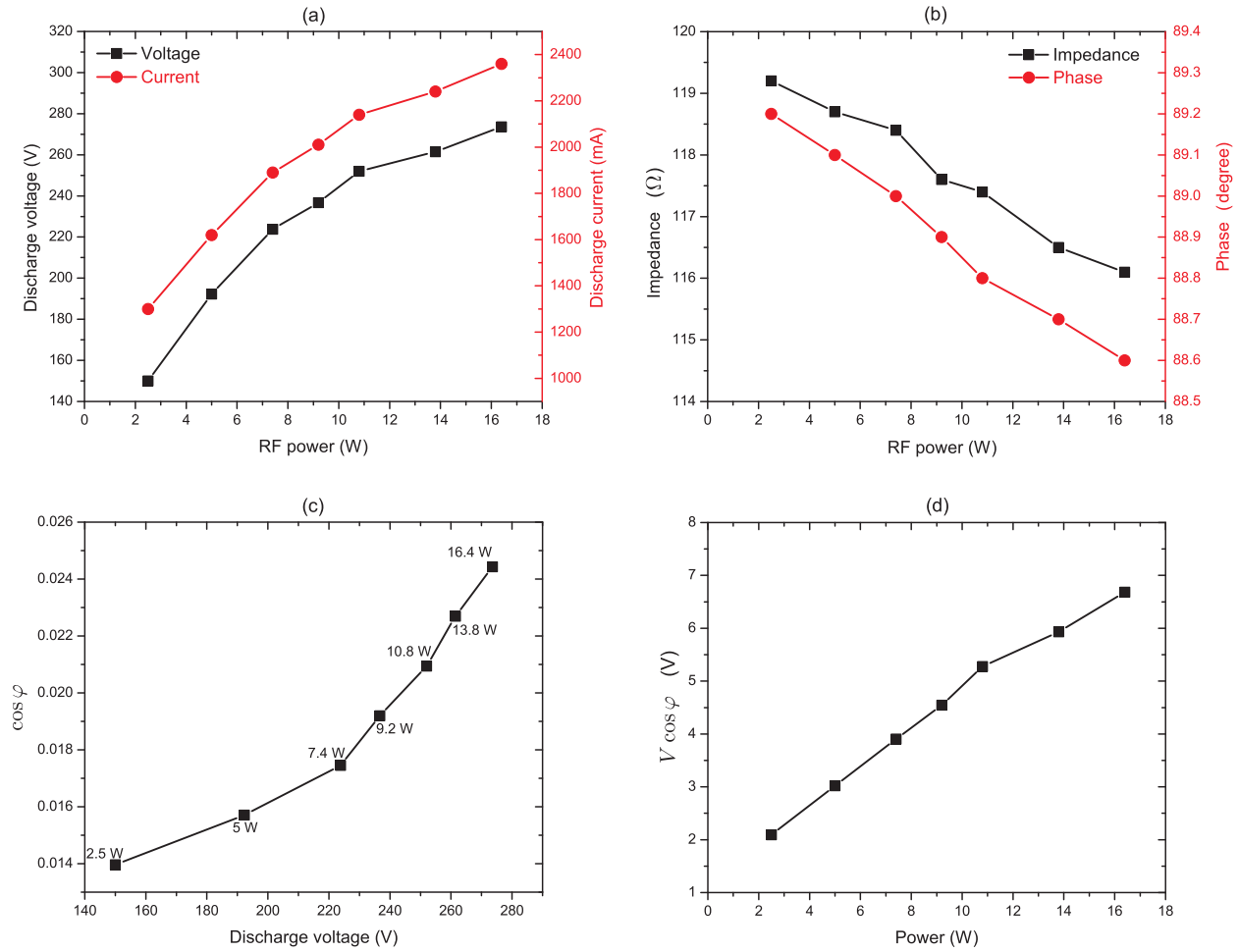

Figure 4.6: *Measured and calculated electrical characteristics of the hollow electrode RF discharge for a fixed pressure $p = 2\,Pa$. (a) Root of mean squares of discharge voltage and current, (b) impedance and phase angle, (c) power factor, (d) ohmic part of the discharge voltage.*

$P_{\mathrm{RF}} = 7\,\mathrm{W}$. The physics behind can be understood from the enhanced collisionality at higher pressures which enables a higher dissipation of the apparent power VI in the plasma. Accordingly, the ohmic component of the discharge voltage $V\cos\varphi$, plotted in Figure 4.7(d), increases as the pressure increases.

It should be noted that the RF power in our experiments is significantly smaller than in the work reported by Bárdoš et al. [120]. There, at similar electrode sizes (lengths of 50 mm and diameters of 10 mm and 20 mm), an RF power of $P_{\mathrm{RF}} = 100\,\mathrm{W}$ was applied at argon gas pressures $p \leq 0.4\,\mathrm{Pa}$. At 0.13 Pa, their 10 mm cathode became red hot. In our experiments, no thermal effects and no drifts in the discharge parameters have been observed. Ignition of the discharge reported in Ref. [120] was possible only at Ar pressures elevated to approximately 1.3 Pa. In our case, the discharge ignites usually without changing temporarily the pressure, only in the case of $p \leq 2\,\mathrm{Pa}$, it is occasionally necessary to raise the pressure by a few Pa; therefore, this behavior resembles the observation reported in Ref. [120]. However, one should bear in mind that the ignition behavior can depend critically on specifics of the

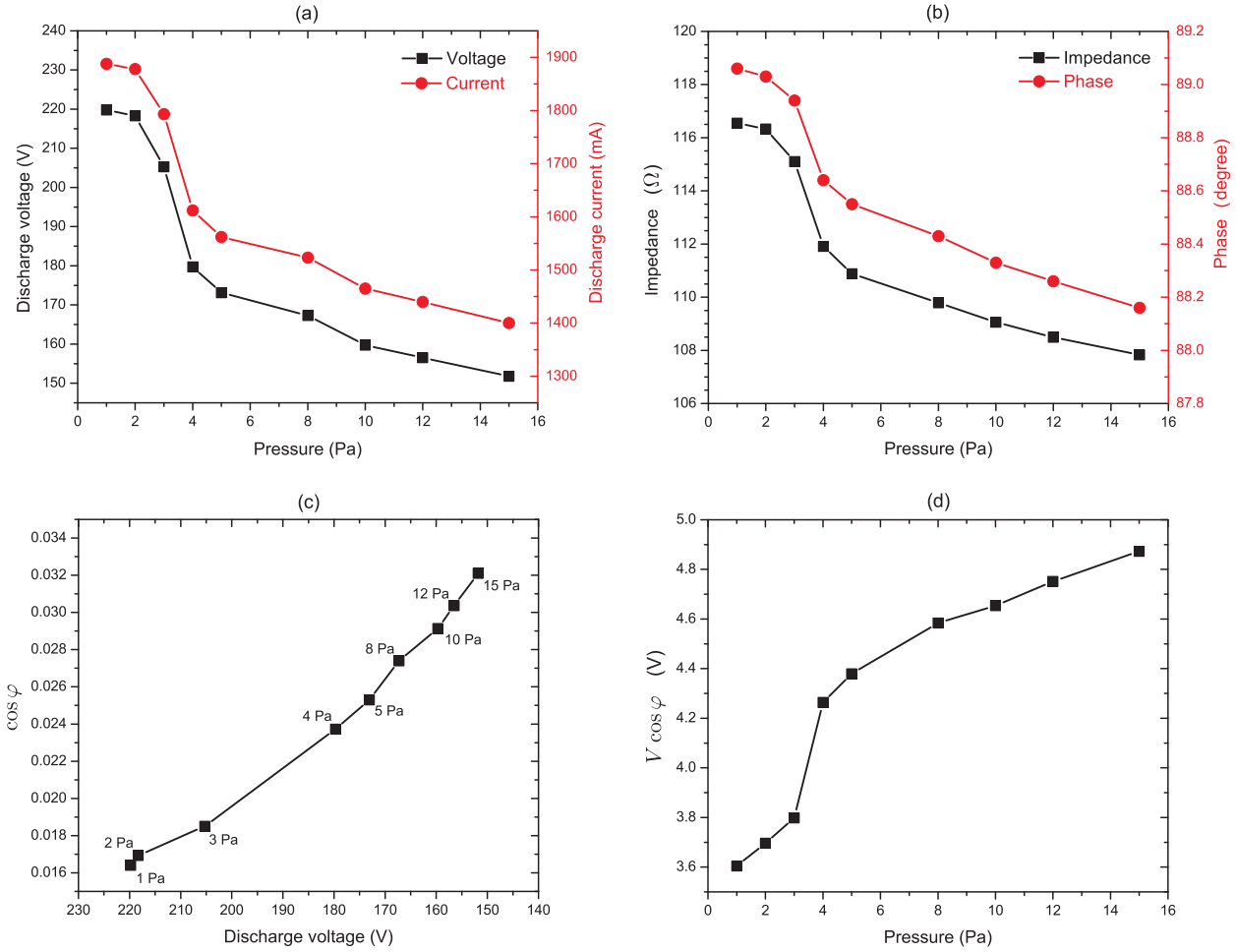

Figure 4.7: *Measured and calculated electrical characteristics of the RF hollow electrode discharge for a fixed RF power $P_{\mathrm{RF}} = 7$ W. (a) Root of mean squares of discharge voltage and current, (b) impedance and phase angle, (c) power factor, (d) ohmic part of the discharge voltage.*

setup like sharp edges with enhanced electric fields.

4.4.3 Visual observations

The variation of the plasma structures with power and pressure can be studied by visual observation. A digital camera facing the aperture of the electrode assembly observed the plasma glow in its inside through a window in the reactor chamber. Figures 4.8(a) and 4.8(b) show the widths of the dark space surrounding the plasma for different discharge conditions. The determination of the sheath width by means of a camera looking along the cylinder axis is somewhat arbitrary, even though the pictures suggest a good impression of the dark space between the electrode and the inner bright plasma [106]. For the plots in Figure 4.8, we took the position where the pixel brightness values reach 25 percent of the maximum value in the center as the sheath edge. The cautious error bars indicate, where 15 and 35 percent are

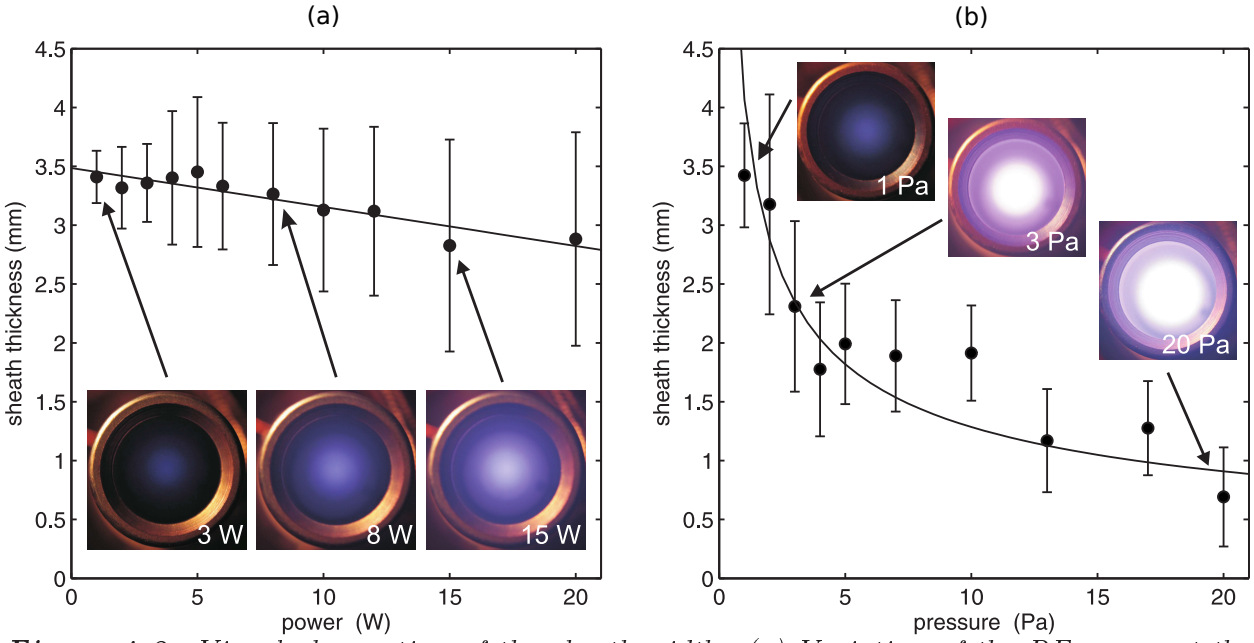

Figure 4.8: *Visual observation of the sheath width. (a) Variation of the RF power at the fixed pressure $p = 2$ Pa. (b) Variation of the pressure at the fixed RF power $P_{\mathrm{RF}} = 7$ W. The fit curve for the pressure variation is proportional to $p^{-1/2}$.*

reached. The dependence of the sheath width on the RF power is weak, as can be seen in Figure 4.8(a). The sheath width decreases very slightly (less than 20 percent) as the power is increased from 1 to 20 W. Concerning the pressure dependence, it has been reported that $p^{1/2}d$ appears to be a constant in some RF discharges, where d is the sheath width [128,129]. Therefore, we plotted a fit proportional to $p^{-1/2}$ into Figure 4.8(b), which shows that this law seems to be fulfilled in our case, too. This trend can provide an opportunity to control the film deposition process or the nanoparticle modification by RF discharges as well [130]. However, we do not want to assign further importance to this apparent functional relation, which actually depends self-consistently on the kind of collisions, the sheath potential and current density.

4.4.4 Oxygen admixture

Admixing a reactive gas is crucial in plasma based materials processing such as plasma polymerization [45] and controlled generation and modification of nanoparticles [6,12]. Since the presence of a reactive species, even as a minor component, can dramatically change the plasma parameters, understanding the role of reactive species in a given discharge configuration is a vital step for its applications.

Here, we study exemplarily the effect of variable oxygen admixtures on the discharge. The total pressure and the absorbed power are kept constant at $p = 2$ Pa and $P_{\mathrm{RF}} = 7$ W, respectively. Figure 4.9 shows the results for oxygen admixtures up to 36 percent of the total gas flow. The electron temperature is reduced by almost 1 eV and the electron density

is reduced to about one fifth when the oxygen concentration is increased to the mentioned amount.

This trend agrees with the measurements performed by Taylor et al. in an inductively coupled RF discharge at a pressure of $p = 1.3\,\mathrm{Pa}$ [130, 131], though the trend is more pronounced in our case. The same authors used a zero-dimensional particle and power balance model for an understanding of the influence of the gas composition on electron temperature and density. They concluded that a higher ionization energy results in a higher electron temperature, because the plasma needs electrons of higher energies to keep the ionization rate large enough to balance the electron losses to the walls. For a similar reason, a lower ionization energy would result in higher electron densities due to the increased ease of ionization.

The ionization energy of molecular oxygen (12.6 eV) is lower than the one of argon (15.8 eV). Taylor and Tynan argue that the threshold energy for oxygen dissociation (5.6 eV) does not affect the resulting electron temperature since it is lower than the ionization potential [131]. Following this reasoning, oxygen admixture would reduce the mean ionization energy and explain the observed trends in our RF hollow electrode discharge, too.

Additionally, the oxygen gas atoms are electronegative, i.e. they tend to form negative ions. These negative ions reduce, due to the quasi-neutrality of the plasma, the electron density with respect to the positive ion density. The influence on electron temperature and density, however, is complex and not easy to predict, since the entire discharge is affected [132]. Indeed, we observed a decrease of discharge voltage and current of about 20 percent (and consequently a change of the phase angle) for the oxygen admixture of 36 percent. The measurements with the impedance probe did not show drifts in any of the electrical paramteters over a time of continuous operation of one hour. The situation will become more complicated when (as planned in future experiments) charged nanoparticles are present in the discharge region.

4.5 Conclusions

An electrode configuration was introduced that makes use of a combination of RF plasma generation and the hollow cathode effect. The working gas streams through the hollow electrode setup into a reactor chamber. The low pressure discharge in argon was characterized by Langmuir probe measurements in the effluent plasma, electrical measurements and visual observations.

It was experimentally shown that the RF fluctuations of the plasma potential were weak and that there was no need for an RF compensation in the probe circuit. The plasma potential was in the order of magnitude of $+25\,\mathrm{V}$, and the RF powered hollow electrode attained a negative bias voltage comparable to the measured RF voltage. From these findings it was concluded that the potential of this discharge resembles the one of a DC hollow cathode discharge: The RF hollow electrode acts as a cathode, the (grounded) counter electrode acts

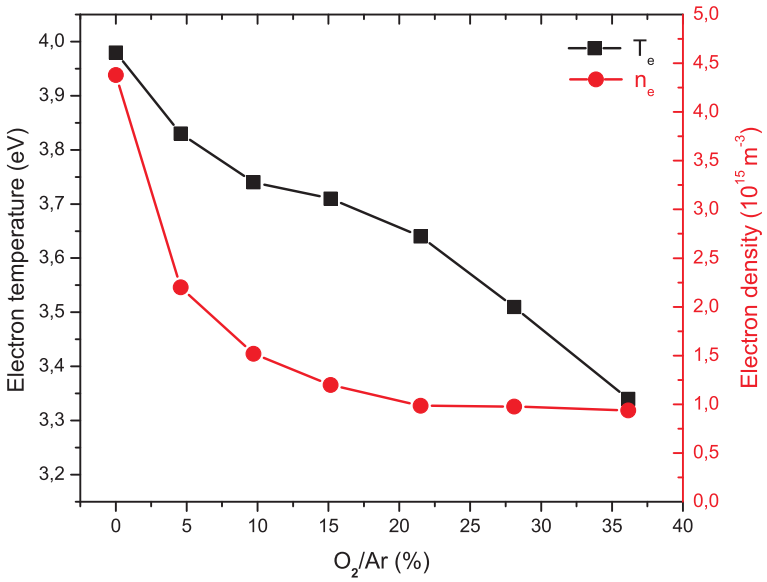

Figure 4.9: *Effect of oxygen admixture on electron density and temperature. The total gas pressure $p = 2\,Pa$ and the RF power $P_{\mathrm{RF}} = 7\,W$ are kept constant. The Langmuir probe was placed in the effluent plasma 12 mm in front of the electrode unit at its axis.*

as an anode, and there is a high voltage sheath in the inner region of the "hollow cathode". Concerning plasma density, electron temperature, and sheath width, the discharge showed the typical behavior known from RF discharges.

First experiments with admixtures of a reactive gas have also been presented. Oxygen was added up to a relative flux of 36 percent of the constant total flux. The electron temperature was reduced by approximately 1 eV and the electron density was reduced to approximately 20 percent at the maximum admixture.

In conclusion, the used electrode and discharge configuration results to be a promising tool for the treatment of nanoparticles, plasma polymerization and nanocomposite fabrication which will be addressed in a forthcoming publication.

4.6 Acknowledgements

This work was supported by the German Research Foundation (DFG) within the framework of the Collaborative Research Center SFB-TR 24, subproject B13. A. M. Ahadi is grateful to the Iran Ministry of Science for financial support. We would also like to thank Peter Sommer for technical support.

Chapter 5

Modification of a metal nanoparticle beam by a hollow electrode discharge

Amir Mohammad Ahadi[1], Alexander Hinz[1], Oleksandr Polonskyi[1], Thomas Trottenberg[2], Thomas Strunskus[1], Holger Kersten[2], and Franz Faupel

[1]Institute for Materials Science – Multicomponent Materials, University of Kiel, 24143 Kiel, Germany

[2]Institute of Experimental and Applied Physics, University of Kiel, 24098 Kiel, Germany

5.1 Abstract

Treatment of nanoparticles (NPs) in complex environments, such as plasmas, is of interest for the fabrication of advanced nanomaterials with desired properties and also from a physical point of view. Here, we investigate the mutual interaction between silver NPs and an RF plasma at different conditions by combining a cylindrical hollow electrode with a gas aggregation source. The investigation of the NP deposits and the morphology of the casted films shows that the applied RF discharge significantly changes the path of the NPs as well as the NP size distribution in the beam. Starting from a neutral NP beam, it is observed that most of the NPs leave the plasma region with negative charge(s), yet the fraction of positively charged NPs grows with power. Furthermore, the plasma characteristics are slightly influenced by the NP flux since the passing NPs collect the plasma charge carriers.

5.2 Introduction

The unique properties of nanoparticles (NPs) for many different applications have attracted much attention in the last decades [133–136]. Recently, NPs have been widely used in fabrication and adjusting properties of advanced nanocomposite materials [2, 98, 137, 138]. For better control of the NP properties it is an advantage, if the particle formation and the subsequent processing, i.e., the functionalization of the NPs or the fabrication of the nanocomposites, are performed in separate environments. In such an approach, not only the processing environments should be well matched, but also a large fraction of the generated NPs should pass well through the second atmosphere.

Among several approaches for NP generation, magnetron sputtering combined with a gas aggregation source (GAS) is a very effective method which is applicable for different types of materials [7, 139]. Control of the crucial parameters for the particle formation process is a big advantage of this technique. Concerning the gas condensation approach, many works have practically [5, 6] and theoretically [4, 25, 93] studied the NP formation processes [140] and characterized the deposited NP films [103]. By utilizing this approach for highly reactive elements like titanium, a stabilized NP generation is possible under certain operating conditions [12]. Furthermore, feeding the magnetron with pulsed power leads to a huge increase in deposition rate [6, 13] and also formation of size controlled NPs [6].

To produce nanocomposite materials containing NPs, it is necessary to combine the GAS with other deposition techniques such as a magnetron discharge [1] or evaporation [141]. In many cases, a low pressure discharge environment is required to activate the chemical components and deposit the nanocomposite materials [92,142,143]. An RF magnetron discharge is a suitable candidate towards this aim, but because of the inhomogeneously ignited discharge and the permanent magnetic field, the NPs show a complicated charging behavior. These influences can directly affect the properties of the resulting films, particularly when a magnetic material is employed for a desired nanocomposite [143].

In this work, a fairly small cylindrical hollow electrode discharge [144] is applied to create an RF plasma at low pressure and low power. The high electron density in the low pressure regime offers a well suitable environment to decompose the chemical precursors to form homogeneous films. Additionally, the highly symmetric system allows easier access and control of the plasma parameters. Therefore, this unit is suggested here as a suitable system for different processing of different materials at low pressure without the above mentioned difficulties of an RF magnetron discharge. It will be demonstrated that due to the geometry of the device and the low working pressure, this system can be well combined with a GAS. In the following, we present a detailed study of the mutual interactions between the NPs and the RF discharge, which is of high interest both from a physical and a technical point of view. To understand the plasma–NP interaction properly, the generated cluster beam is purified by a deflector (placed between the GAS and the hollow electrode discharge) removing all charged NPs coming from the GAS. It is observed that the RF discharge can dramatically change the properties of the NP beam by charging the NPs and redistributing the NPs in the beam.

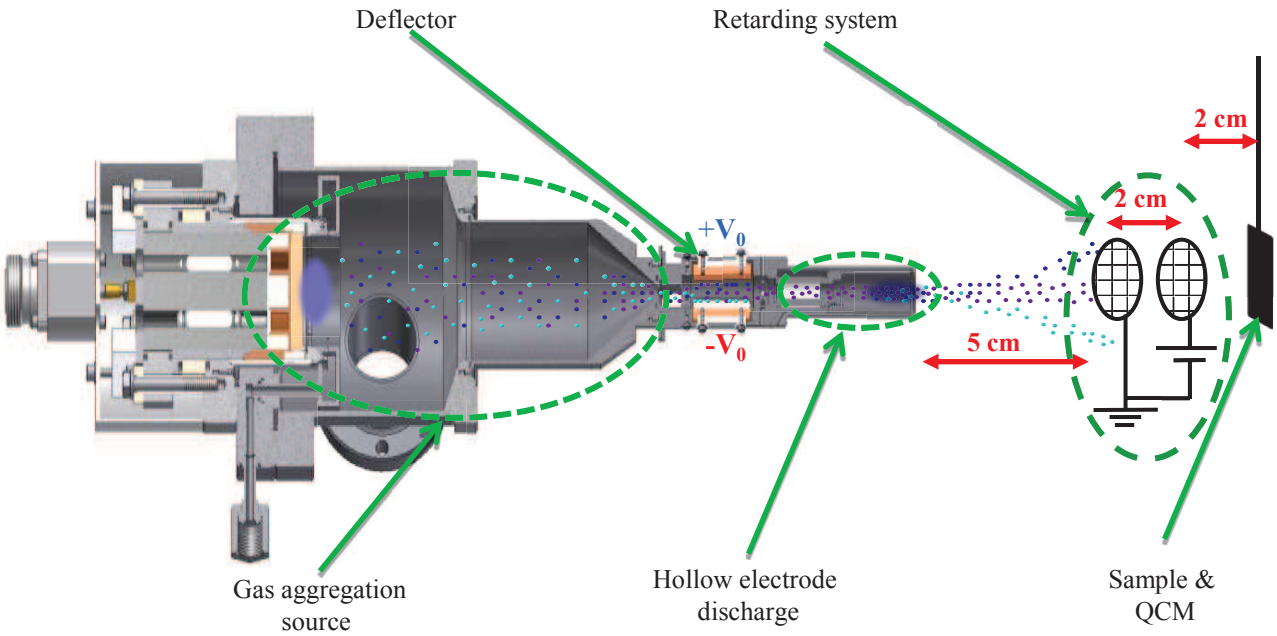

Figure 5.1: *(Color online) A scheme of the used experimental setup. All parts are installed in the main deposition chamber. The deflection of nanoparticles was performed by fixing* V_0 *at 70 V.*

5.3 Experimental

A home constructed gas aggregation cluster source equipped with a 2 in. magnetron and a 2 in. round silver target (with 6 mm thickness) was used to produce silver nanoclusters. The GAS was connected to a larger main chamber via a 3 mm diameter orifice [92]. The background pressure in the system (main chamber and GAS) was 10^{-5} Pa which has been achieved with a turbo molecular pump (Pfeiffer TMU 261) in combination with a scroll pump (Varian SH 110). The working pressure of the GAS was fixed to 200.0 Pa (measured by a MKS baratron) by injecting 115 sccm argon as working gas. The argon flow was controlled by a MKS mass flow controller (200.0 sccm). Furthermore, the working pressure in the main chamber was 2.00 Pa (measured by a MKS baratron) during the experiments.

To purify the NP beam, a deflection system was mounted in the main chamber directly after the orifice of the GAS. It simply consists of two plate electrodes connected to a tunable DC power supply. By the applied electric field, the charged NPs are eliminated from the cluster beam via rectangular slits in the electrodes.

The RF discharge was driven at 13.56 MHz by connecting a cylindrical electrode to an RF power supply (Dressler, Cesar136) via a matching box and also a postmatched V-I probe (Impedans Ltd, Octiv VI Probe) which is placed between the matching box and the vacuum feedthrough. The discharge properties of the plasma created with this cylindrical electrode configuration at different conditions has been reported previously. There, the RF plasma was there characterized by a Langmuir probe in the effluent [144].

For measuring the contribution of each charged species, a retarding system was placed 5 centimeters in front of the hollow electrode discharge. The retarding system consisted of two stacked mesh electrodes: One electrode was grounded and the other one was connected to an adjustable DC power supply allowing both polarities (Figure 5.1). It serves as a filter for the charged NPs and allows *to remove one type* of the charged species by tuning the polarity and the strength of applied voltage. One should note that we do not intend to use the retarding system like a current measuring retarding field analyzer. Therefore, not more than two grids are rquired, because a plasma electron repelling grid and a secondary electron suppressing grid are meaningless for our purpose [145]. Beyond the retarding system, a grounded Quartz Crystal Microbalance (QCM) monitor and a sample holder are mounted to collect the arriving NPs.

By collecting the NPs on carbon coated copper grids, the morphology of the deposited thin films was characterized by means of transmission electron microscopy (TEM). For this purpose a JEM-2100 (JEOL, 200 kV, LaB6) operated in bright-field mode was used. The experimental setup is sketched in Figure 5.1.

5.4 Results and Discussion

At first, the influence of the deflector on the deposition of the NPs is investigated. The silver NPs generated in the GAS at 200 Pa are transported into the main chamber by a buffer gas stream and are deposited onto the QCM after passing through the deflector. The deposition rate of the NP beam is recorded for different applied deflector voltages. The following observations are deduced from the obtained results presented in Figure 5.2(a): First, the deposition rate at the lower magnetron power reaches a stable plateau earlier than observed for the higher power. This could be explained by the increase of the NP size at higher magnetron power [5, 85]. Bigger NPs need more energy (stronger electric field, i.e, higher voltage) to be deflected from the beam, and hence the purification process is completed only at higher voltage. As the second observation, a stable deposition rate is reached at a lower level at higher applied power. This is caused by an increased charging of the NPs in the GAS at higher magnetron power (see supplementary material) which leads to a reduction of the fraction of the neutral species in the beam (Figure 5.2(a)). In the following experiments, the deflector voltage has been fixed at 140 V in order to make sure that always only neutral NPs remain in the beam at the different applied conditions.

The influence of RF power on the spatial distribution of the NPs in the beam was determined by collecting the NPs on a glass substrate. The results clearly show that the geometry of the deposited spot is significantly altered by the RF power (Figure 5.2(b)). For a nonpowered hollow electrode discharge, a very sharp spot with distinct boundary is formed. Operating the discharge at low power (2 W), the deposited spot is uniformly expanded to a larger area. Using a 10 W discharge leads to a sharp central spot surrounded by a larger diffuse shadow.

For the same conditions, also the lateral distribution of the NPs over the cross section

of the beam has been determined. In these measurements, the QCM has been masked by an aluminum foil that exhibits a 1 mm rectangular slit in the center region. Then by moving it with 1 mm steps across the cluster beam, the deposition rate is recorded at each position (Figure 5.2(b)). The results show that not only the deposition rate along the cross section is strongly influenced by the applied RF power, but also the total amount of deposited material (estimated by the area under the curve) is strongly changed as well by the applied RF power. Since the NPs mostly get negatively charged in the discharge (as will be seen later), particularly at low power, electrostatic forces dominate the NP interactions and the NPs leaving the discharge region will strongly repel each other. Therefore, an expanded spot is formed, and a significant fraction of the NPs will be deflected so much that they cannot be detected by the QCM. Furthermore, NPs can already leave the beam in the plasma region by diffusion to the walls. It is well known [146] that the negative species in the discharge volume are effectively trapped in the bulk plasma due to the negative potential of the plasma walls. Furthermore, the bias voltage of the RF hollow electrode discharge is increased with increasing RF power [144]. Thus, at higher RF power, diffusion of negative species in the volume is significantly restricted which improves the deposition yield in this regime compared to lower powers. Indeed, for low power discharges, high particle diffusion in the volume (due to a low plasma wall potential) and also high interparticle repulsion forces cause very low deposition yields.

The influence of the RF hollow electrode discharge on the size of the NPs is investigated by analyzing TEM samples obtained at different RF powers. As can be seen in Figure 5.3, the mean size of the NPs which are treated by low RF power (2 W), is almost similar (6.3 nm in mean diameter) to the untreated NPs (6.4 nm in mean diameter). At higher applied RF power (10 W), one has to consider the two different regions in the nonuniform spot (see Figure 5.2(b)). The sample obtained at the center of the spot (Figure 5.3(c)) consists of bigger clusters (9.5 nm average diameter) compared to those collected from the nontreated NP beam. The mean size of the NPs collected at the shadow zone (Figure 5.3(d)) is significantly smaller (5 nm in diameter) than the untreated ones. This means the plasma acts like a selector at this RF power regime which could be very interesting for technical applications. Again, the nanoparticle separation can be explained based on the charging processes in the volume of the RF plasma. As can be seen in Figure 5.5, a higher RF power leads to a relative decrease of negatively charged NPs and an increase of the positively charged ones. This can be explained by an increase in the plasma density. Consequently, the effect of interparticle electrical repulsion will be smaller. By using Coulomb's equation, one can calculate that, by increasing the power from 5 W to 15 W in the given conditions, the average of the interparticle repulsion force for each particle is decreased by a factor of 2 and synchronously the mean of the interparticle attraction force is increased by a factor of 2.5. Hence the total interparticle repulsion force for each NP is decreased by a factor of 5. At this condition, the deflection is negligible for the bigger NPs, while, due to the much lower mass, the trajectories of smaller NPs are much more influenced. Therefore, the bigger NPs are deposited at the center of the spot and the smaller NPs at the edge, as reflected in the obtained NP size distributions (Figure 5.3(c),(d)).

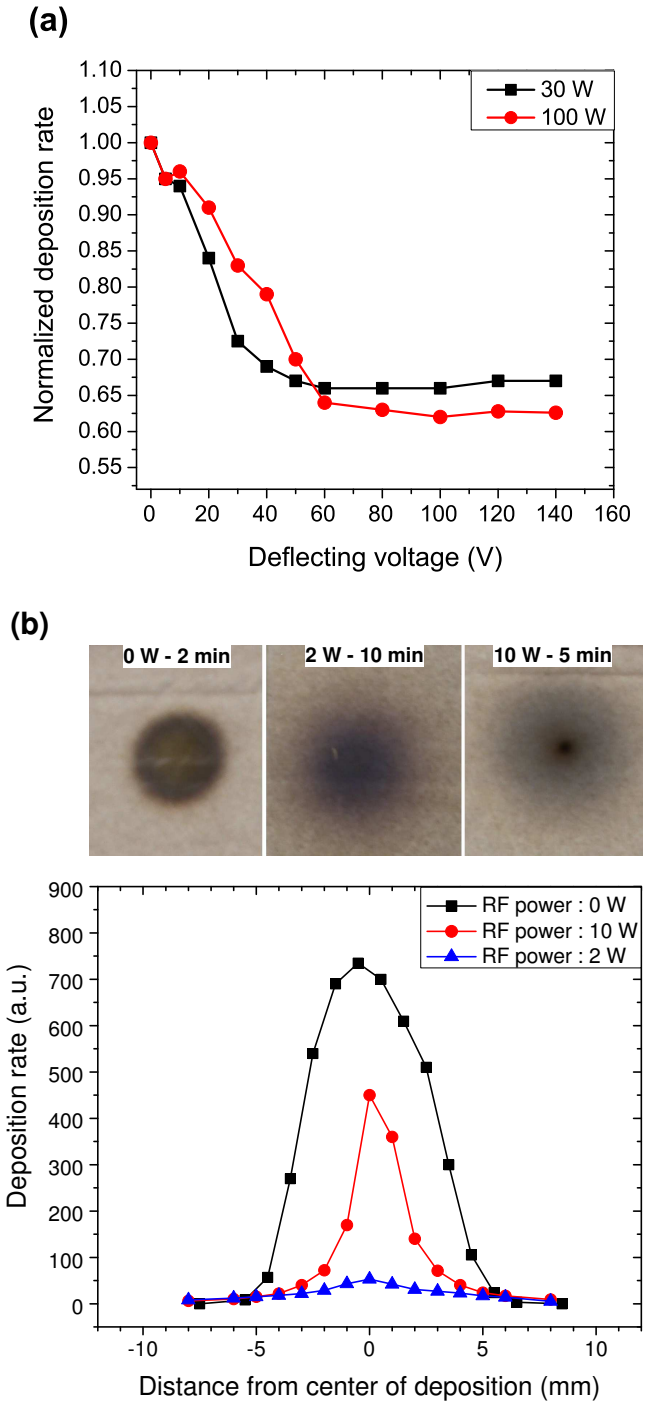

Figure 5.2: *(Color online) a) Relative NP deposition rates observed at different magnetron powers for different deflection voltages. For each applied power, the rate of NP deposition without purification was used to normalize the deposition rates. b) Images of the deposited spots prepared at different RF powers and corresponding lateral distribution of the NP deposition rate measured by the QCM. The magnetron power was fixed to 50 W.*

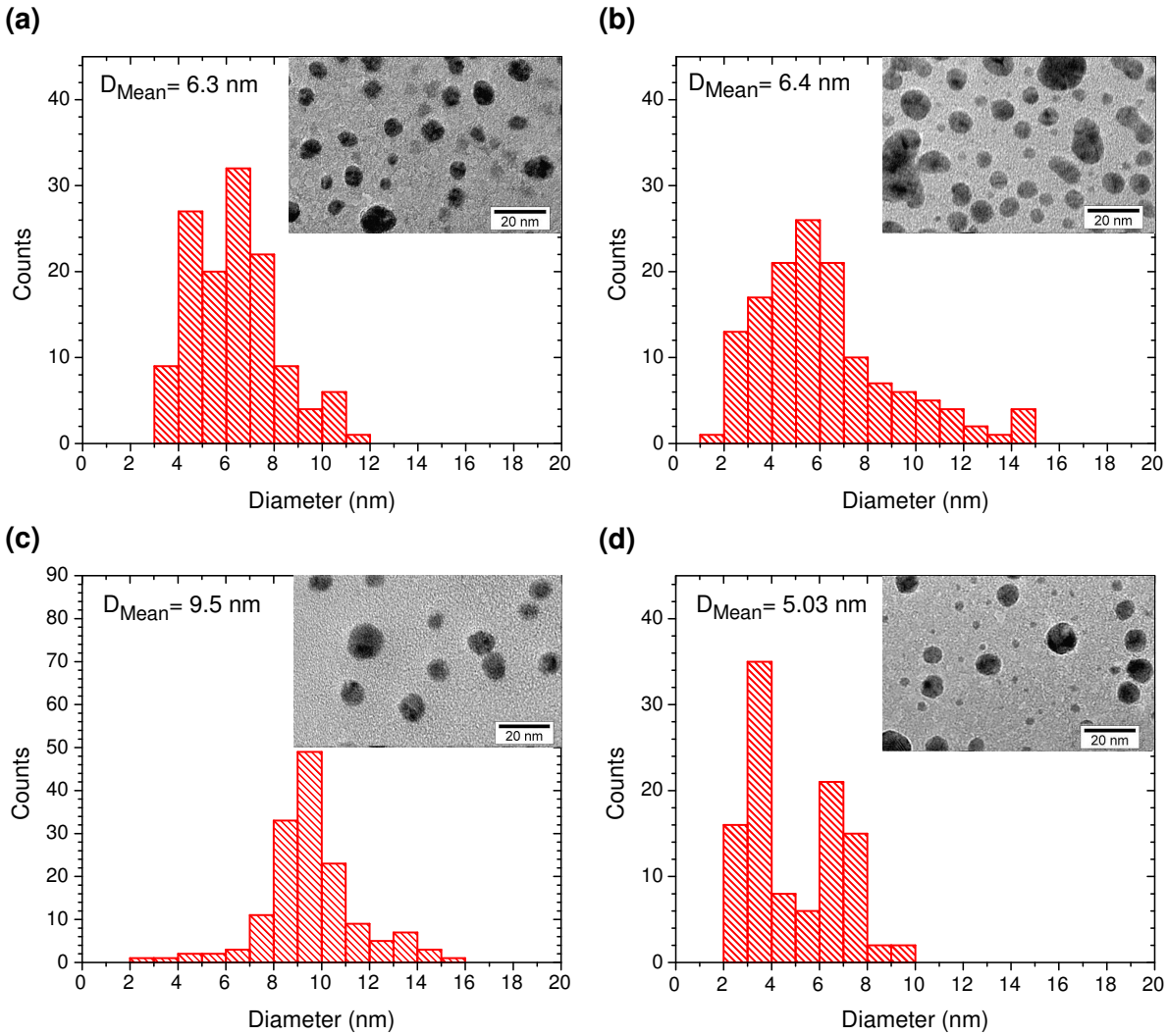

Figure 5.3: *(Color online) TEM micrographs of silver nanoparticles generated by the GAS after exposing the RF hollow electrode discharge. The DC power of the magnetron was fixed at 100 W, and the RF discharge was operated at a) 0 W, b) 2 W, c) 10 W (center of spot), d) 10 W (edge of spot).*

NPs of different sizes and/or velocities [147] can exhibit different probabilities to become charged by the RF discharge due to different cross sections and residence times. Additional information on the plasma–NPs interactions should be obtained by studying the charging mechanisms in the plasma volume and also the size distributions of the different charged species. These topics are left for future investigations, since they are beyond the scope of this study.

In the next step, the influence of the NP concentration on the characteristics of the RF discharge is studied by means of Langmuir probe measurements.The RF power (which is monitored by the post-matched V-I probe) is fixed at 7 W throughout this step. The NP concentration in the discharge volume is altered by tuning the feeding power of the magnetron discharge (Figure 5.4, dotted blue line) while the other operation conditions are

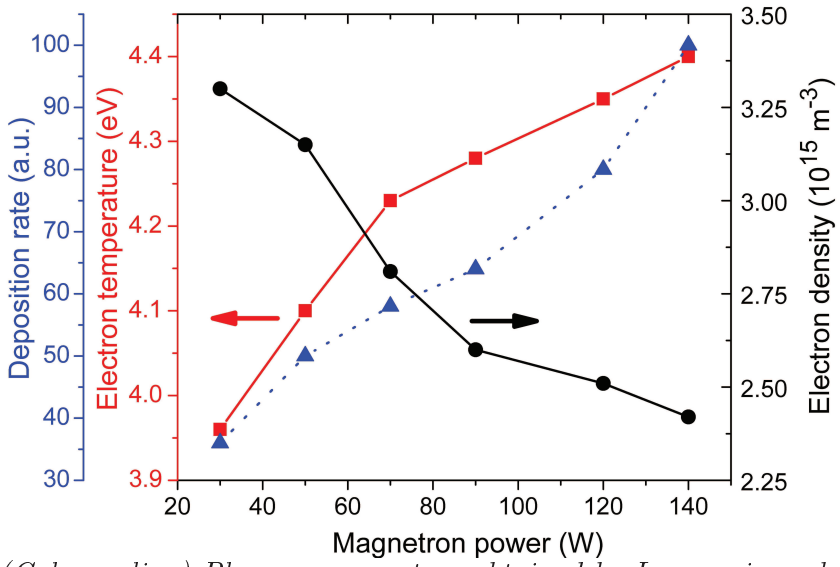

Figure 5.4: *(Color online) Plasma parameters obtained by Langmuir probe measurements in the presence of different concentrations of silver NPs. The dotted blue line indicates the deposition rate. The power of the RF discharge was fixed at 7 W.*

kept constant. The obtained results (Figure 5.4) obviously illustrate that by increasing the number of NPs in the plasma region, the electron density is decreased while the electron temperature is increased slightly. Increasing the number of silver NPs in the discharge leads to an increase in captured electrons that will be transfered out of the discharge zone which results in a lower plasma density. A similar behavior has been reported for a plasma containing micrometer sized particles [148, 149]. There, in addition to the above mentioned mechanism, neutralization of plasma charge carriers on the surface of dust grains plays an important role in the reduction of the electron density. But, due to the low surface area of the particles in the nanometer range, this process should not be much pronounced in the present system.

Finally, for demonstration of the role of the RF hollow electrode discharge on the charging of NPs, a retarding system is installed between the hollow electrode discharge and the QCM. After purification of the NP beam by the deflector, the neutral NPs pass through the RF discharge and are then filtered by the retarding system before they reach the QCM. To determine the percentage of each charge species in the NP beam, the total deposition rate (without any applied voltage on the retarding system) and the deposition rates for both polarities of the retarding system are recorded. From the obtained three deposition rates at the different retarding conditions, the contribution of each species at a certain RF power can easily be calculated. To have enough particles at the QCM position, the magnetron discharge was operated at 100 W. Furthermore, the feeding power of the hollow electrode discharge has been varied in the range of 5–15 W.

The obtained data indicate that most of the NPs leave the plasma region with negative charge(s). As we have already shown [144], in spite of the low operating pressure (2 Pa), the hollow electrode generates a discharge exhibiting a high electron density. Thus, as a direct result, the probability for charging the NPs in plasma volume is relatively high. Additionally,

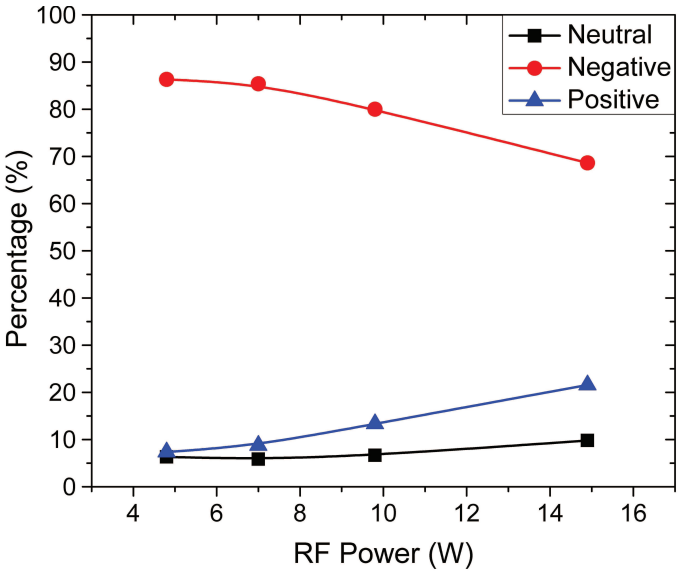

Figure 5.5: *(Color online) Variation of the charging of neutral nanoparticles for different RF discharge powers. The negatively charged nanoparticles are in the majority, but decrease with the applied RF power.*

as can be seen in Figure 5.5, increasing the RF discharge power leads to a decrease in the fraction of negatively charged particles and an increase in the fraction of positively charged species. The power increase yields a higher plasma density [144] that enhances the total energy flux to the NP surface [68]. Thus, the surface temperature is elevated due to a higher rate of the ion–electron recombinations on the surface of the NPs. Subsequently, the probability for thermoemission of electrons from the NP surface is enhanced which causes a larger fraction of positively charged NPs [27]. Under the conditions examined here, only a small portion of neutral NPs leaves the discharge as indicated by the line for the neutral particles in Figure 5.5. The contribution of neutral species is almost constant throughout the tested regime. This could indicate that this fraction of NPs passes through the discharge without significant interaction and thus remains neutral.

However, due to the high plasma density and the symmetric configuration, this system has a strong potential to be used as a versatile technique for functionalizing NPs by reactive plasmas and also for the fabrication of nanocomposite materials. Experiments testing this potential are currently in progress and will be reported in forthcoming publications.

5.5 Conclusions

The mutual interaction between silver NPs and an RF discharge at low pressure was considered by applying an RF hollow electrode discharge connected to a GAS via a deflection system. Most of the NPs become negatively charged by the RF discharge. The percentage of negative NPs decreases by increasing the RF power while the portion of positively charged NPs increases in the NP beam caused by an increased plasma density that enhances the

probability of positive charging in the plasma volume. The discharge significantly changes the lateral distribution of the NPs in the NP beam. The electrostatic repulsion between charged particles is seen as the main factor for an expanded beam. Furthermore, by increasing the RF feeding power, not only the effect of interparticle electric forces is changed due to charge variation, but also the bias voltage of the plasma walls is increased which restricts the diffusion of negative species in the plasma volume. Thus, the profile of the NP deposit is correspondingly changed. The analysis of the particle size distribution obtained from TEM images confirmed the size separation of the NPs by the RF plasma at high applied power. The plasma characterization by a Langmuir probe showed that the concentration of the NPs in the discharge region affects the discharge parameters. A discharge with lower density (and higher electron temperature) is obtained by increasing the number of NPs passing through the plasma volume due to the capture of electrons by the NPs in the plasma.

5.6 Acknowledgements

This work was supported by the German Research Foundation (DFG) within the framework of the Collaborative Research Center SFB TR 24, subproject B13. A. M. Ahadi is grateful to the Iran Ministry of Science and Shahid Chamran University of Ahvaz for financial support. We would also like to thank Stefan Rehders for the technical construction of the gas aggregation source and hollow discharge system and Peter Sommer for technical support.

5.7 Suppelmentary

The NP beam produced by the GAS is purified by passing through a deflection system while the deflector was operated at 140 V to remove all charged NPs. The contribution of neutral NPs in the NP beam is calculated by recording the deposition rate of the neutral beam and the total deposition rate without deflection. As shown in Figure 5.6, the fraction of charged NPs increases as the magnetron power increases.

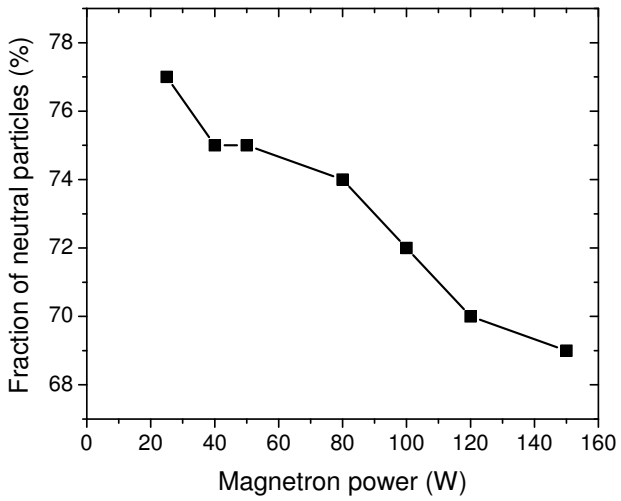

Figure 5.6: *Dependence of the fraction of neutral NPs in the beam on magnetron power. Higher power (discharge electron density) yields a higher fraction of charged clusters.*

Chapter 6

Controlled synthesis of germanium nanoparticles by nonthermal plasmas

Amir Mohammad Ahadi[1,2], Katharine I. Hunter[2], Nicolaas J. Kramer[2], Thomas Strunskus[1], Holger Kersten[3], and Franz Faupel[1], and Uwe R. Kortshagen[2]

[1] Institute for Materials Science - Multicomponent Materials, University of Kiel, 24143 Kiel, Germany

[2] Department of Mechanical Engineering, University of Minnesota Minneapolis, MN, 55455 Minneapolis, USA

[3]Institut for Experimental and Applied Physics, University of Kiel, 24098 Kiel, Germany

6.1 abstract

The size, composition, and crystallinity of plasma produced nanoparticles are crucial factors for their physical and chemical properties. Here, we investigate the role of the process gas composition, particularly the hydrogen (H_2) flow rate, on germanium (Ge) nanoparticles synthesized from a chlorinated precursor by nonthermal plasma. We demonstrate that the gas composition can significantly change the nanoparticle size and also adjust the surface chemistry by altering the dominant reaction mechanisms. A red shift of the Ge-Cl_x infrared absorptions with increasing H_2 flow indicates a weakening of the Ge-Cl_x bonds at high H_2 content. Furthermore, by changing the gas composition the nanoparticles microstructure can be controlled from mostly amorphous at high hydrogen flow to diamond cubic crystalline at low hydrogen flow.

6.2 Introduction

Fabrication of new nanocrystal-based technologies, such as solar cells [150], light emitting devices [151], next-generation transistors [152, 153] and biosensors [154] may benefit from nanocrystals (NCs) with controlled optical and electronic properties. It is well known [15,155] that the properties of NCs are dependent on their size, shape, and surface conditions which may be controlled via the synthesis process. The synthesis of group IV semiconductor NCs such as silicon (Si) and germanium (Ge), has attracted attention due to their narrow bandgaps [15] and their potential role in optoelectronic applications [156]. Several studies suggested that the bandgap of Ge NCs may be tuned from its bulk value of 0.7 eV to 2 eV for 3 nm NCs [157–159], making Ge NCs interesting candidates as active absorbers in photovoltaic devices.

As discussed by Wang et al. [160], Ge nanoparticles (NPs) require high temperatures to be crystallized due to strong covalent bonds; however, the crystallization temperature may decrease with decreasing the NP dimensions [55,160]. While there are reports of liquid phase approaches to synthesize Ge NCs with tuable bandgaps [161], nonthermal plasma synthesis is an excellent alternative for group IV semiconductors [16, 17, 162]. The hot plasma electrons dissociate precursors while the background gas remains at room temperature and NCs nucleate and grow through chemical clustering [16]. The NPs in the plasma are unipolarly charged by the mobile electrons which prevents NP agglomeration [67, 163]. By adjusting the residence time in the plasma, accurate control over Ge NC size can be achieved [17]. Furthermore, the crystallinity of particles can be adjusted by varying the applied power [17].

Controlling the surface conditions of Ge NCs is of large importance for NC luminescent properties [161, 162, 164] as incomplete surface terminations can create nonradiative trap states which quench bandgap emission. Lee *et al.* [161] reported photoluminescence (PL) in the infrared (IR) regime by passivating the Ge NCs by colloidal techniques. Recently, Wheeler *et al.* [162] reported tunable bandgap PL from plasma-synthesized Ge NCs after terminating their surface with Grignard reagents. However, the influence of the process gas composition on the surface chemistry and crystallinity of plasma produced Ge NPs remains largely unexplored [17, 69]. In this letter, we demonstrate that control over the size and the crystallinity of Ge NPs is possible by simply tuning the process gas composition while other parameters such as RF power, precursor concentration, and total pressure remain constant. Furthermore, the process gas composition also controls the surface chemistry of the synthesized Ge NPs.

6.3 Experimental

The experimental system used here was already described in previous reports [16,17]. Argon and hydrogen are used as buffer gases and germanium tetrachloride ($GeCl_4$) as precursor. The gases stream through a 22.3 mm inner diameter quartz tube. Hydrogen is used to scavenge the free chlorine that results from the decomposition of the $GeCl_4$. Two copper

rings electrodes are wrapped around the reactor tube and are connected to an RF generator via a matching box. The electrodes are fixed 5 cm away from the gas inlet. The radio frequency power, driven at 13.56 MHz, is fixed at 50 W during the experiments. The H_2 flow is altered in the range of 0 to 75 sccm (standard cubic centimeters) and the argon flow is adjusted in the range from 22 to 50 sccm to obtain a constant total pressure of 345 Pa. The $GeCl_4$ precursor is stored in a small tank at 10 kPa. Its flow rate is controlled by a fine mass flow controller to achieve a fixed partial pressure of 35 Pa (about 10 percent of the total pressure) throughout the experiments. The Ge NPs are generated by dissociation of $GeCl_4$ in the plasma and subsequent clustering of $GeCl_x$ radicals. The resulting NPs are collected downstream of the discharge on different substrates. The freshly prepared samples are transferred to a load lock system and are then moved into a N_2 purged glove box. To analyze the NP surface chemistry, NPs are deposited onto aluminum coated silicon substrates and investigated in an oxygen free dry nitrogen glove box by a Nicolet Fourier transform infrared (FTIR) spectrometer operated in the reflectance mode. The crystallinity of the Ge NPs collected onto quartz is studied by X–ray diffraction measurements using a Bruker microdiffractometer. The morphology of the Ge NPs deposited as thin films onto carbon coated copper grids is studied by transmission electron microscopy (TEM) using a JEM–2100 (JEOL, 200 kV, LaB6) operated in bright–field mode.

6.4 Results and discussion

The use of H_2 in the plasma synthesis of Ge NCs is essential, as it scavenges Cl from the $GeCl_4$ precursor. Without H_2 injection, no Ge NPs are formed in the plasma [17]. Hence we focus in this letter on the important role of the H_2 flow on the properties of the produced Ge NPs. To avoid an influence on residence time [51], the total pressure is kept constant in all experiments at 345 Pa. Furthermore, the concentration of the precursor is also held constant in order to avoid an influence of this parameter on the size and chemical composition of the resulting Ge NPs [17]. To attain a fixed pressure, only the Ar flow is altered as necessary for the different H_2 flows.

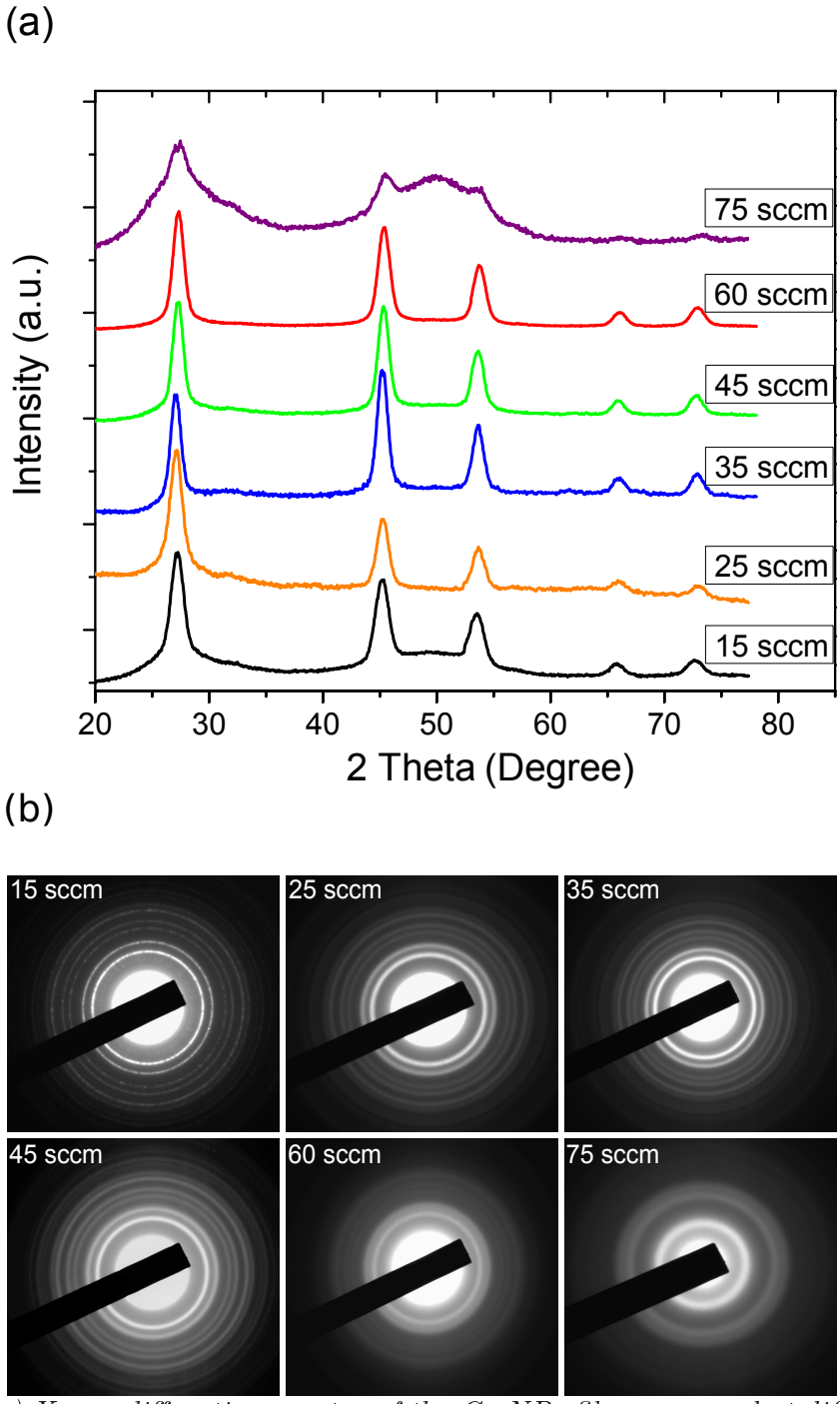

Figure 6.1: *a) X–ray diffraction spectra of the Ge NPs films prepared at different hydrogen admixtures. For clarity the spectra are normalized. b) Corresponding electron diffraction patterns.*

Initial experiments showed that no Ge NPs form at H_2 flows lower than ∼13.5 sccm. At higher H_2 concentrations Ge NPs can be synthesized. The XRD patterns displayed in Figure 6.1(a) indicate that at the highest H_2 flow the synthesized Ge NPs are mostly amorphous. The XRD spectra for crystalline samples show several characteristic peaks

corresponding to the (111), (220), (311), (400) and (331) planes of Ge crystals with a cubic diamond structure. This observation is well corroborated by electron diffraction patterns of corresponding TEM samples displayed in Figure 6.1(b). Electron diffraction indicates that the highest crystallinity (as indicated by the sharpest rings) is obtained at the lowest H_2 flows; increasing the hydrogen content gradually reduces NP crystallinity as reflected by broadening and finally disappearing of the diffraction rings.

The transition from quite crystalline Ge NPs to mostly amorphous is likely related to the variation of the plasma parameters for the different gas compositions. We hypothesize that with increasing H_2 content the plasma density decreases, leading to reduced NP heating through energetic surface reactions [51,68]. As this is the key mechanism for selective heating of NPs in nonthermal plasmas, the NP may not reach sufficiently high temperatures for crystallization.

The size evolution of the Ge NPs is investigated by transmission electron microscopy (TEM). The results are displayed in Figure 6.2. In contrast to previous suggestions [17], we observed that the Ge NP mean size does not increase continuously with the hydrogen content. We find that at low H_2 flow the NP mean size increases with the H_2 partial pressure, then, after passing through a maximum, it decreases with increasing H_2 partial pressure (Figure 6.3). A calculation of the NC sizes with the Scherrer equation (using Jade 8.0 software to fit the XRD patterns) confirms the size evolution obtained by the TEM measurements.

This behaviour may be explained as follows. In the low H_2 regime, increasing the hydrogen content leads to a more effective scavenging of chlorine species and thus an increased growth process of Ge NPs. In the high H_2 regime other factors may become more important. Numerical simulations of argon-hydrogen plasmas indicate that the effect of increasing H_2 content on electron temperature may be highly dependent on discharge conditions (e.g. pressure, applied power) [165]; however, Langmuir probe measurements of low-pressure argon plasmas, similar to synthesis conditions used in this paper, have shown that the addition of H_2 reduces the electron temperature [68]. The decreased electron temperature may reduce the $GeCl_4$ dissociation and thus the particle growth. A detailed study of the plasma chemistry in this synthesis plasma is beyond the scope of this letter.

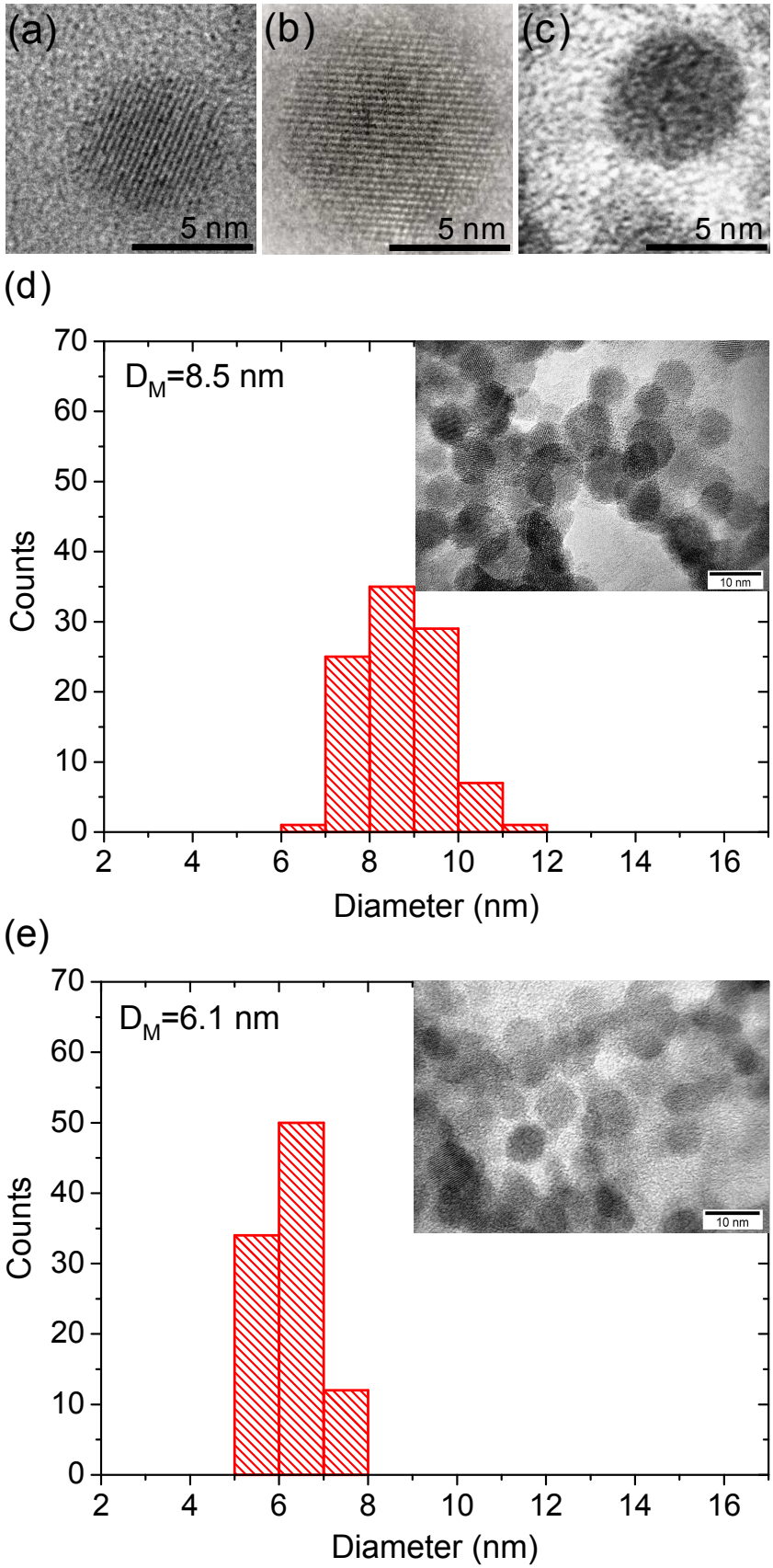

Figure 6.2: *High resolution TEM images of the Ge NPs synthesized by nonthermal plasma technique at different hydrogen concentrations: a) H_2=15 sccm, b) H_2=35 sccm and c) H_2=75 sccm and low-resolution TEM images and the coressponding size distribution at different hydrogen concentrations: d) H_2=25 sccm, e) H_2=75 sccm at constant total pressure and power.*

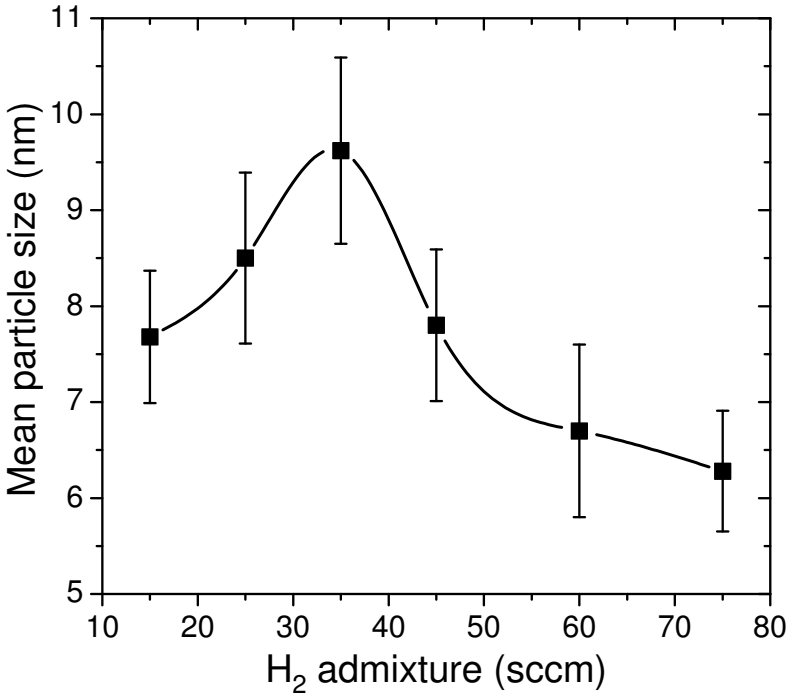

Figure 6.3: *Evolution of mean particle size of the Ge NPs by changing the hydrogen partial pressure in the discharge. The power and pressure were fixed at 50 W and 345 Pa respectively. Error bars are calculated based on standard deviation of the size distribution determined by TEM measurements. The line is just a guide to the eye.*

The FTIR spectra for different samples, shown in Figure 6.4(a), provide information about the Ge NP surface chemistry. The stretching modes of Ge–H_x bonds are located at 2100 cm^{-1}. As to be expected, at very low H_2 admixture the abundance of H_x species on the surface of the NPs is quite low since most of the created hydrogen radicals are consumed by scavenging the chlorine species in the plasma. At higher hydrogen partial pressures, one observes a significant increase of the bands originating from the Ge–H stretching modes. Close to the band of the stretching modes appears a shoulder at 1900 cm^{-1} (being more pronounced at high H_2 content) which may be attributed to Ge–H stretching vibrations in the bulk [166]. The bands appearing in the range of 500 to 1000 cm^{-1} are assigned mainly to higher order deformations of Ge in the NPs bonded to Cl_x and H_x species [162]. Additionally, according to Fang *et al.* [167], the intensity of the band at 575 cm^{-1} is proportional to the content of hydrogen in the material. As can be seen in Figure 6.4(a), this band apparently grows with the H_2 content and provides another evidence for a change of the NP surface chemistry with hydrogen partial pressure.

The FTIR measurements of the different samples show a red shift of the Ge–Cl_x vibrational band (Figure 6.4(a)). Typically, such a shift can be understood as a result of electrostatic interaction between different species which can lengthen (or contract) certain bonds in the presence of a third species. This effect is associated with a red (blue) shift in the IR because of weakening (strengthening) of the bond [168]. Here, the presence of

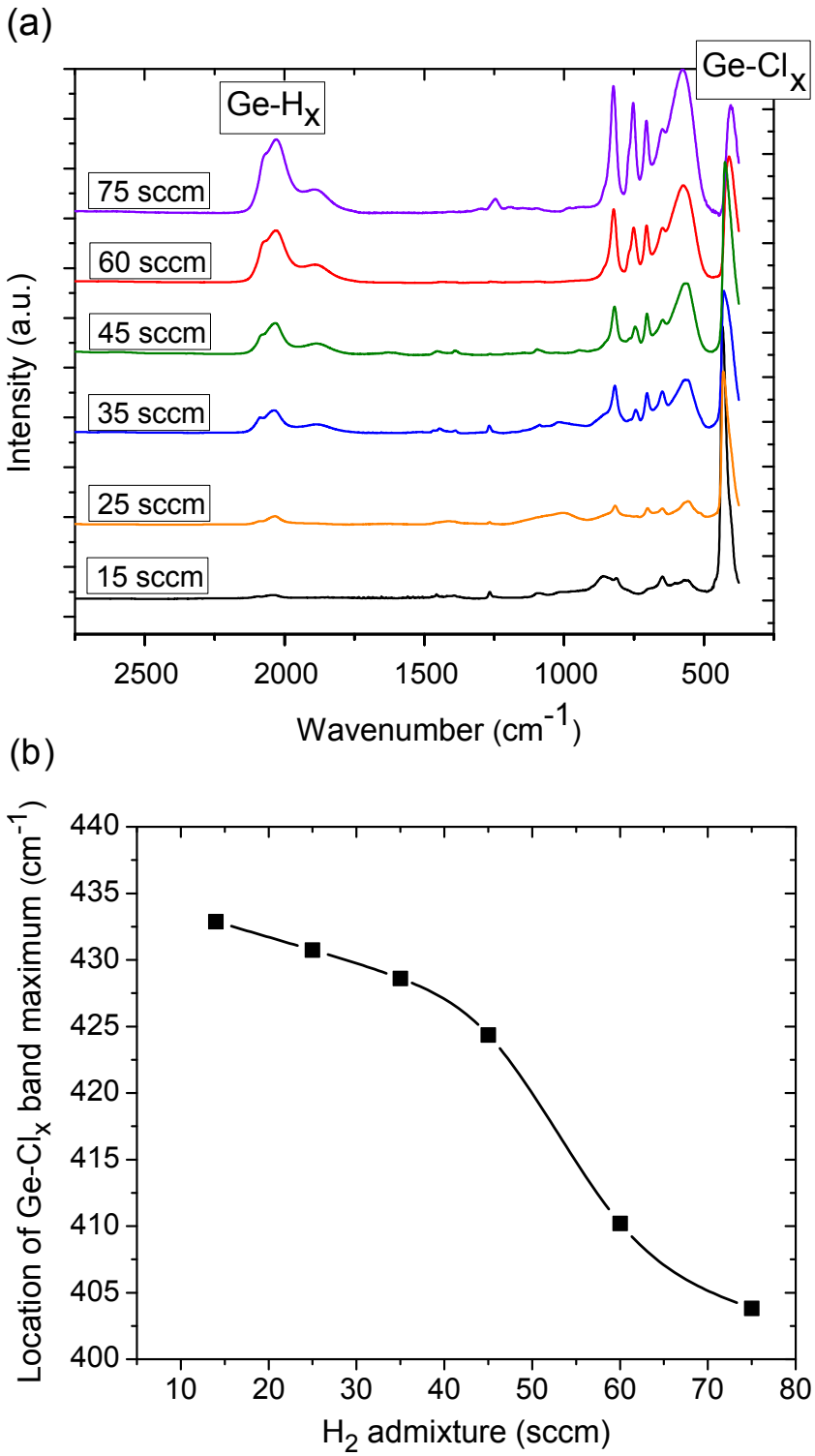

Figure 6.4: *a) FTIR spectra of as-synthesized Ge NPs for different hydrogen admixtures into the nonthermal plasma at fixed power (50 W) and fixed pressure (345 Pa). The Ge–H_x bands show an increase with H_2 partial pressure. For clarity the spectra are normalized. b) The evolution of the Ge–Cl_x band position (red shift) with H_2 flow rate. The line is a guide to the eye.*

hydrogen species on the surface of Ge NP influences on Ge–Cl_x bond. The electrostatic interaction between chlorine species and hydrogen species on the NP surface lengthens the Ge–Cl_x bond and, consequently, shifts the corresponding stretching band in the IR spectrum to the lower energy. This red shift is more pronounced at high hydrogen admixtures (Figure 6.4(b)), since in this regime more chlorine species are substituted by hydrogen species. More hydrogen species on the NP surface enhance the electrostatic attraction of chlorine species and, subsequently, a stronger shift is present due to more Ge–Cl_x lengthening.

Finally, we point out that the mechanism described here is not limited to particles of a certain size or a certain reactor configuration. In the supporting information, we present data for smaller Ge NPs (3-5 nm in diameter) produced in a different reactor setup, which show the same trends as discussed here. See Supporting Information, figures S1-S3.

6.5 Conclusions

We studied the role of hydrogen admixture in the synthesis of Ge NPs in nonthermal plasmas at constant power and pressure. We find that an increasing H_2 flow allows to shift the NP microstructure from crystalline to amorphous. Additionally, the surface coverage of Ge NPs can be adjusted between chlorine rich at low H_2 flow to hydrogen rich at high H_2 flow. A red shift of the Ge–Cl_x features in the FTIR spectra indicates weaker Ge–Cl_x bonds at high hydrogen admixture. The H_2 flow also significantly affects the NP size likely by changing the rate of precursor dissociation. This study suggests that controlling the composition of the process gases is a versatile technique to generate Ge NPs with tunable properties.

6.6 Acknowledgments

The authors thank Alexander Hintz for TEM measurements. A. M. Ahadi is grateful to the Shahid Chamran University of Ahvaz for financial support. K.I. Hunter acknowledges support by the National Science Foundation Graduate Research Fellowship Program under Grant No. 00039202. N. J. Kramer acknowledges support through a dissertation fellowship from the University of Minnesota. This work was partially supported by the German Research Foundation (DFG) within the framework of the Collaborative Research Center SFB TR24 - B13. This work was supported primarily by the U.S. National Science Foundation through the University of Minnesota MRSEC under Award Number DMR-1420013. Parts of this work were carried out in the Characterization Facility, University of Minnesota, which receives partial support from NSF through the MRSEC program.

Chapter 7

Summary and Outlook

7.1 Summary

Generation and characterization of metal, oxide metal and semiconductor NPs were investigated experimentally by employing different techniques, based plasma, within three individual projects. The possible scenarios and the physics beyond the observed phenomena were discussed and explained by suitable models. In the following, the main achievements of each part, are separately summarized.

7.1.1 DC and pulsed DC reactive sputtering for nanoparticle generation

The preliminary experiments, using a gas condensation chamber combined with a conventional (nonreactive) DC magnetron sputtering showed that the NP generation from reactive materials, such as titanium (Ti) and cobalt (Co), is not possible with common parameters [10]. It seems, the low binding energy of the pure Ti (and Co) atoms, prevents to form the stable nucleus in the GAS. Changing the chemistry of the NP seeds by adding a very low concentration of a reactive gas, such as oxygen or nitrogen, is a beneficial solution for the above problem [10]. Forming transition NPs from an oxidized target at different conditions proved that the reactive gas should concern as a crucial parameter in the NP generation process. Additional experiments using a constant stream of the oxygen admixture demonstrated that for generation of TiO_x NPs, equilibrium between the sputtering process and the target poisoning must be established [6,12]. Our findings have shown that at certain applied conditions (pressure, gas flow and magnetron power) the NP formation is achievable, if the reactive admixture gas is selected from an appropriately narrow range of admixture.

Additionally, due to the dynamic behavior of the sputtering and the poisoning process, the long term stabilized NP formation is not guaranteed for reactive materials. The evolution

of the NP generation is strongly depended on the reactive admixture, the history of the target and the operating conditions. It was also shown that only at certain oxygen admixture, **the stable TiO_x NP formation at low pressure (50 W) is achievable.** The range of oxygen flow for operating at the stable regime is very narrow and strongly depends on the magnetron power [12]. At higher applied pressures, increasing the number of return oxidized species to the target enhances the poisoning process and subsequently, reduces the sputtering rate. Therefore, the stable D.R. is shifted to a very low level or disappeared at all.

Using pulsed DC discharge instead conventional DC discharge, led to a huge increase of the NP deposition. Preliminary experiments approved that the dominant mechanisms in the pulse regime are quite different compared to those in the DC regime [13]. In the pulsed DC regime, sputter off the oxidized species from the target have main contribution in the clustering process while in the DC regime, oxidation in the volume is more pronounced. Higher effective power density at the *time on* period provides more cluster seeds and eventually, an increase in the D.R. is observed for the pulsed DC regime.

The influence of the pulsing parameters (frequency and duty cycle) and the role of oxygen admixture in the NP formation process were also investigated. The analyzed data demonstrated that at given conditions, **the stable NP production is limited to a narrow range of oxygen admixture and a certain pulsing parameters.** Small changes from the optimal values led to an unstable NP deposition and/or shifting the stable D.R. to a lower level. The morphology of NP films showed a very narrow size distribution of the NPs generated by the pulsed DC sputtering [6]. Furthermore, **the size of NPs is significantly affected by the reactive admixture gas.**

7.1.2 Materials processing by an RF hollow electrode

Material processing in a controllable environment with well known characteristics, is preferred from different aspects. In this dissertation a typical electrode configuration, performing at low RF power and low pressure regime was designed and then characterized by different plasma diagnostic methods. According to the results of the several measurements, **the fluctuations of the RF potential do not significantly disturb the plasma parameters.** Thus, a single Langmuir probe, without RF compensation in the external circuit, is sufficient to characterize the electrostatic parameters of the ignited RF discharge. Furthermore, **this discharge resembles the one of the DC hollow cathode discharge with high plasma density.** A detailed study of the ignited discharge at different conditions indicated increasing electron density and decreasing electron temperature by pressure and power. Additionally, changing the gas composition by adding oxygen as a reactive admixture (which is needed for some materials processings), led to the lower electron density and lower electron temperature [169].

In the next step of this project, modification of a silver NP beam by the RF hollow electrode discharge was studied. Charge measurements of the NPs indicated, that **most of the NPs leave the plasma with negative charge(s).** The percentage of the positively charged particles in the beam was increased by the RF power. Furthermore, the dynamics

of the charged NPs is determined by the interparticle electrical forces which are specified by the dominant mechanisms in the discharge. As discussed in chapter 5, changing **the RF power influences the profile of the NP deposition** through two channels; first, by affecting on the interparticle electric forces via varying the charging process, and second, by increasing the bias voltage of the plasma walls which restricts the diffusion of negative species in the plasma volume. Hence, **the spatial distribution of NPs in the beam is affected by plasma conditions.** This fact was corroborated by the size distribution of NPs in the deposited spot. On the other hand, varying the density of NPs in the plasma volume can change the plasma parameters due to capture of electrons by the NPs in the plasma.

7.1.3 Controlled synthesis of semiconductor nanoparticles

The physical and chemical properties of the semiconductor NPs are important parameters in the fabrication of photovoltaic and optoelectronic materials. Therefore, the study of possible ways to control the properties of semiconductor NPs are of interest. As demonstrated in the last part of this thesis, tuning the chemical composition of the used gases can be applied as a novel technique to control the NP synthesis process in a nonthermal plasma reactor. Varying the hydrogen admixture could control the growth rate of NPs produced by this technique. **The content of the admixed hydrogen can influence on the concentration of different species in the plasma, which results NPs with different sizes and surface chemistry** [170]. Adjusting the crystallinity of the synthesized NPs, from mostly amorphous to highly crystalline NPs, is another interesting finding of this study. As it is well known, ion – electron recombination on the particle surface is the main process in elevating the temperature of the particles in plasmas [14, 68]. The plasma chemistry can control the rate of particle heating process by changing the plasma density. Therefore, **the crystal status of the NPs is indirectly determined by the gas composition in the plasma reactor.**

7.2 Outlook

Due to the novelty of the NP generation by reactive pulsed DC magnetron sputtering, many aspects of this technique are not yet clarified. For example, no accepted model and no practical evidence have been reported to explain the generation mechanism of very narrow sized NPs by this method. Furthermore, the contribution of different species in nucleation and growth processes is not clear. The influence of operating conditions on chemical structures of NPs and also the chemical activity of the formed NPs is another interesting subject for future investigation. As we have shown in chapter 5, most of the NPs are charged in the RF hollow electrode. The charge numbers of each particle and its variation by plasma conditions and particle size are very interesting topics for the next studies. High plasma density of the used discharge and control over the discharge parameters, promise the configuration to be a versatile system for plasma polymerization and also NP functionalization at the low pressure regime. In combination with other techniques, this unit could also be utilized for fabrication

of nanocomposites as well as core - shell NPs with tunable properties. High electric conductivity of semiconductor NC thin films is very interesting for electronic applications. To prevent the NCs agglomeration in a solution, the surface of NCs should be functionalized by long chain alkene molecules [69]. According to the previous report [69], the conductivity of the functionalized Ge NCs films is quite low even after an annealing process, because the alkyl molecules on the NCs inhibit charge transport between neighboring NCs. Measuring the electrical properties of the cast films of Ge NCs, after washing the alkene molecules from the NCs surfaces with a suitable technique, is an attractive subject for future study, too.

Bibliography

[1] H. Biederman, "Nanocomposites and nanostructures based on plasma polymers," *Surface and Coatings Technology*, vol. 205, pp. S10–S14, July 2011.

[2] F. Faupel, V. Zaporojtchenko, T. Strunskus, and M. Elbahri, "Metal-Polymer nanocomposites for functional applications," *Advanced Engineering Materials*, vol. 12, pp. 1177–1190, Dec. 2010.

[3] C. Binns, "Nanoclusters deposited on surfaces," *Surface Science Reports*, vol. 44, pp. 1–49, Oct. 2001.

[4] K. Wegner, P. Piseri, H. V. Tafreshi, and P. Milani, "Cluster beam deposition: a tool for nanoscale science and technology," *Journal of Physics D: Applied Physics*, vol. 39, pp. R439–R459, Nov. 2006.

[5] O. Polonskyi, P. SolaÅ, O. Kylián, M. Drábik, a. Artemenko, J. Kousal, J. Hanuš, J. Pešička, I. Matolínová, E. Kolíbalová, D. Slavínská, and H. Biederman, "Nanocomposite metal/plasma polymer films prepared by means of gas aggregation cluster source," *Thin Solid Films*, vol. 520, pp. 4155–4162, Apr. 2012.

[6] A. M. Ahadi, O. Polonskyi, U. Schürmann, T. Strunskus, and F. Faupel, "Stable production of TiO x nanoparticles with narrow size distribution by reactive pulsed dc magnetron sputtering," *J Phys D: Appl Phys*, vol. 48, no. 3, p. 35501, 2015.

[7] P. Solar, O. Polonskyi, A. Choukourov, A. Artemenko, J. Hanuš, H. Biederman, and D. Slavínská, "Nanostructured thin films prepared from cluster beams," *Surface and Coatings Technology*, vol. 205, pp. S42–S47, July 2011.

[8] W. Tang, J. J. Eilers, M. a. van Huis, D. Wang, R. E. I. Schropp, and M. Di Vece, "Formation and photoluminescence of cauliflower silicon nanoparticles," *The Journal of Physical Chemistry C*, vol. 119, pp. 11042–11047, May 2015.

[9] H. Haberland, M. Karrais, M. Mall, and Y. Thurner, "Thin films from energetic cluster impact: A feasibility study," *Journal of Vacuum Science & Technology A: Vacuum, Surfaces, and Films*, vol. 10, p. 3266, Sept. 1992.

[10] T. Peter, O. Polonskyi, B. Gojdka, A. M. Ahadi, T. Strunskus, V. Zaporojtchenko, H. Biederman, and F. Faupel, "Influence of reactive gas admixture on transition

metal cluster nucleation in a gas aggregation cluster source," *Journal of Applied Physics*, vol. 112, no. 11, p. 114321, 2012.

[11] A. Marek, J. Valter, S. Kadlec, and J. Vyskočil, "Gas aggregation nanocluster source â Reactive sputter deposition of copper and titanium nanoclusters," *Surf. Coat. Technol.*, vol. 205, pp. S573–S576, 2011.

[12] A. M. Ahadi, V. Zaporojtchenko, T. Peter, O. Polonskyi, T. Strunskus, and F. Faupel, "Role of oxygen admixture in stabilizing TiO x nanoparticle deposition from a gas aggregation source," *Journal of Nanoparticle Research*, vol. 15, p. 2125, Nov. 2013.

[13] O. Polonskyi, T. Peter, A. M. Ahadi, A. Hinz, T. Strunskus, V. Zaporojtchenko, H. Biederman, and F. Faupel, "Huge increase in gas phase nanoparticle generation by pulsed direct current sputtering in a reactive gas admixture," *Applied Physics Letters*, vol. 103, no. 3, p. 033118, 2013.

[14] U. Kortshagen, "Nonthermal plasma synthesis of semiconductor nanocrystals," *Journal of Physics D: Applied Physics*, vol. 42, p. 113001, June 2009.

[15] A. Alivisatos, "Semiconductor clusters, nanocrytals, and quantum dots," *Science*, vol. 271, no. 5251, pp. 933–937, 1996.

[16] L. Mangolini, E. Thimsen, and U. Kortshagen, "High-yield plasma synthesis of luminescent silicon nanocrystals.," *Nano letters*, vol. 5, pp. 655–9, Apr. 2005.

[17] R. Gresback, Z. Holman, and U. Kortshagen, "Nonthermal plasma synthesis of size-controlled, monodisperse, freestanding germanium nanocrystals," *Applied Physics Letters*, vol. 91, no. 9, p. 093119, 2007.

[18] S. M. Rossnagel, "Magnetron plasma deposition processes," *Thin Solid Films*, vol. 171, pp. 125–142, 1989.

[19] P. J. Kelly and R. D. Arnell, "Magnetron sputtering : a review of recent developments and applications," *Vacuum*, vol. 56, pp. 159–172, 2000.

[20] J. Musschoot and J. Haemers, "Qualitative model of the magnetron discharge," *Vacuum*, vol. 84, pp. 488–493, Dec. 2009.

[21] J. W. Bradley, R. D. Arnell, and D. G. Armour, "Measurement and modelling of the bulk plasma in magnetron sputtering sources," *Surface and Coatings Technology*, vol. 97, pp. 538–543, 1997.

[22] Donald L. Smith, *Thin film deposition.*
McGrow - Hill, 1995.

[23] S. Girshick, C. Chiu, R. Muno, C.Y.Wu, L. Yang, S. K. Singh, and P. H. Mcmurry, "IRON PARTICLES," *Journal of Aerosol Science*, vol. 24, no. 3, pp. 367–382, 1993.

[24] K. Wegner, B. Walker, S. Tsantilis, and S. E. Pratsinis, "Design of metal nanoparticle synthesis by vapor ow condensation," *chemical Engineering Science*, vol. 57, pp. 1753–1762, 2002.

[25] P. V. Kashtanov, B. M. Smirnov, and R. Hippler, "Magnetron plasma and nanotechnology," *Physics Uspekhi*, vol. 50, no. 5, pp. 455–488, 2007.

[26] B. M. Smirnov, "Cluster Plasmas," *Physics Uspekhi*, vol. 43, no. 5, p. 453, 2000.

[27] B. M. Smirnov, "Generation of cluster beams," *Physics-Uspekhi*, vol. 46, pp. 589–628, June 2003.

[28] W. M. Haynes and D. R. Lide, eds., *CRC Handbook of Chemistry and Physics*. CRC Press, Boca Raton, 91th ed., 2010.

[29] H. T. N. Matsunami, Y. Yamamura, Y. Itikawa, N. Itoh, Y. Kazumata, S. Miyagawa, K. Morita, R. Shimizu, "Energy dependence of the Ion-Induced solids sputtering yields of monatomic," *Atomic data and nuclear data tables*, vol. 31, pp. 1 – 80, 1984.

[30] A. Belkind, A. Freilich, J. Lopez, Z. Zhao, W. Zhu, and K. Becker, "Characterization of pulsed dc magnetron sputtering plasmas," *New Journal of Physics*, vol. 7, pp. 90–90, Apr. 2005.

[31] G Zhao-qiang, WU Xue-mei, YAO Wei-guo, "Experimental Study on RF Hollow Cathode Discharge," *Plasma Science and Technology*, vol. 3, no. 6, pp. 1037–1042, 2001.

[32] S. Muhl and A. Pérez, "The use of hollow cathodes in deposition processes: A critical review," *Thin Solid Films*, vol. 579, pp. 174–198, Mar. 2015.

[33] G. Franz, *Low pressure plasmas and microstructuring technology*. Springer, 2009.

[34] W. Kohsiek, "Measurement of the electron temperature and density of a helium plasma produced by a hollow cathode {...}," *Plasma Physics*, vol. 17, pp. 1083–1089, 1975.

[35] F. Paschen, "No Title," *Annalen Der Physik*, vol. 355, no. 16, p. 901, 1916.

[36] R. W. Boswell, "Very efficient plasma generation by whistler waves near the lower hybrid frequency," *Plasma Physics and Controlled Fusion*, vol. 26, no. 10, pp. 1147–1162, 1984.

[37] L. Bardos, H. Barankova, and S. Berg, "Thin film processing by radio frequency hollow cathodes Â´," *Surface and Coatings Technology*, vol. 97, pp. 723–728, 1997.

[38] C. M. Horwitz, B. S, , G. M, and D. K, "Hollow cathode etching and deposition," *Journal of Vacuum Science & Technology A: Vacuum, Surfaces, and Films*, vol. 6, p. 1837, May 1988.

[39] H. Barankova and L. Bardos, "Hollow cathode plasma sources for large area surface treatment," *Surface and Coatings Technology*, vol. 146-147, pp. 486–490, 2001.

[40] R. Soukup, N. Ianno, and J. Huguenin-Love, "Analysis of semiconductor thin films deposited using a hollow cathode plasma torch," *Solar Energy Materials and Solar Cells*, vol. 91, pp. 1383–1387, Sept. 2007.

[41] A. Dyson, P. Bryant, and J. E. Allen, "Multiple harmonic compensation of Langmuir probes in rf discharges," *Measurement Science and Technology*, vol. 11, pp. 554–559, 2000.

[42] R. R. J. Gagne and A. Cantin, "Investigation of an rf Plasma with Symmetrical and Asymmetrical Electrostatic Probes," *Journal of Applied Physics*, vol. 43, no. 6, p. 2639, 1972.

[43] N. M. B. N St J Braithwaite and J. Allen, "An electrostatic probe technique for RF plasma," *Journal of Physics E:Scientific Instruments*, vol. 20, p. 1046, 1987.

[44] J. S. Kim, G. H. Kim, T. H. Yeom, and K. H. Kwon, "Characterization of an Oxygen Plasma by Using a Langmuir Probe in an Inductively Coupled Plasma," *Journal of the Korean Physical Society*, vol. 38, no. 3, pp. 259–263, 2001.

[45] H. K. Yasuda, *Plasma polymerization*.
Academic press, 2012.

[46] V. Fortov, a. Ivlev, S. Khrapak, a. Khrapak, and G. Morfill, "Complex (dusty) plasmas: Current status, open issues, perspectives," *Physics Reports*, vol. 421, no. 1-2, pp. 1–103, 2005.

[47] A. V. Kozyrev and A. N. Shishkov, "Two Regimes of heat exchange between a metal particle and a nonequilibrium plasma," *Technical physics letters*, vol. 28, no. 6, pp. 504–506, 2002.

[48] Y. V. Martynenko, M. Y. Nagel, and M. a. Orlov, "A nanoparticle in plasma," *Plasma Physics Reports*, vol. 35, no. 6, pp. 494–498, 2009.

[49] A. A. Samarian, O. S. Vaulina, A. P. Nefedov, V. E. Fortov, B. W. James, and O. F. Petrov, "Positively charged particles in dusty plasmas," *Phys. Rev. E*, vol. 64, p. 056407, Oct 2001.

[50] Y. Martynenko and L. Ognev, "Thermal radiation from nanoparticles," *Technical physics*, vol. 50, no. 11, pp. 1522–1524, 2005.

[51] N. J. Kramer, R. J. Anthony, M. Mamunuru, E. S. Aydil, and U. R. Kortshagen, "Plasma-induced crystallization of silicon nanoparticles," *Journal of Physics D: Applied Physics*, vol. 47, p. 075202, Feb. 2014.

[52] S. Boninelli, F. Iacona, G. Franzò, C. Bongiorno, C. Spinella, and F. Priolo, "Formation, evolution and photoluminescence properties of Si nanoclusters," *Journal of Physics: Condensed Matter*, vol. 19, p. 225003, June 2007.

[53] W. Gerberich, W. Mook, C. Perrey, C. Carter, M. Baskes, R. Mukherjee, a. Gidwani, J. Heberlein, P. McMurry, and S. Girshick, "Superhard silicon nanospheres," *Journal of the Mechanics and Physics of Solids*, vol. 51, pp. 979–992, June 2003.

[54] A. N. Goldstein, C. M. Echer, and A. P. Alivisatos, "Melting in Semiconductor Nanocrystals," vol. 256, no. June, pp. 1425–1427, 1992.

[55] M. Hirasawa, T. Orii, and T. Seto, "Size-dependent crystallization of Si nanoparticles," *Applied Physics Letters*, vol. 88, no. 9, p. 093119, 2006.

[56] J. P. Wilcoxon, G. A. Samara, and P. N. Provencio, "Optical and electronic properties of si nanoclusters synthesized in inverse micelles," *Phys. Rev. B*, vol. 60, pp. 2704–2714, Jul 1999.

[57] D. Jurbergs, E. Rogojina, L. Mangolini, and U. Kortshagen, "Silicon nanocrystals with ensemble quantum yields exceeding 60%," *Applied Physics Letters*, vol. 88, no. 23, p. 233116, 2006.

[58] A. A. Howling, J. L. Dorier, and C. Hollenstein, "Negative ion mass spectra and particulate formation in radio frequency silane plasma deposition experiments," *Applied Physics Letters*, vol. 62, no. 12, p. 1341, 1993.

[59] A. A. Howling, L. Sansonnens, J.-L. Dorier, and C. Hollenstein, "Time-resolved measurements of highly polymerized negative ions in radio frequency silane plasma deposition experiments," *Journal of Applied Physics*, vol. 75, no. 3, p. 1340, 1994.

[60] M. T. Swihart, "Electron Affinities of Selected Hydrogenated Silicon Clusters (Si x H y , x) 1-7 , y) 0-15) from Density Functional Theory Calculations," pp. 6083–6087, 2000.

[61] A. Gallagher, a. a. Howling, and C. Hollenstein, "Anion reactions in silane plasma," *Journal of Applied Physics*, vol. 91, no. 9, p. 5571, 2002.

[62] A. Gallagher, "Model of particle growth in silane discharges," *Physics Review E*, vol. 62, p. 2690, 2000.

[63] U. Bhandarkar, U. Kortshagen, and S. L. Girshick, "Numerical study of the effect of gas temperature on the time for onset of particle nucleation in argon â silane low-pressure plasmas," *Journal of Physics D: Applied Physics*, vol. 36, pp. 1399 – 1408, 2003.

[64] U. V. Bhandarkar, M. T. Swihart, S. L. Grishick, and U. R. Kortshagen, "Modelling of silicon hydride clustering in a low-pressure silane plasma," *Journal of Physics D: Applied Physics*, vol. 33, pp. 2731 – 2746, 2000.

[65] Y. Watanabe, "Formation and behaviour of nano/micro-particles in low pressure plasmas," *Journal of Physics D: Applied Physics*, vol. 39, pp. R329–R361, Oct. 2006.

[66] J Goree, "Charging of particles in a plasma," *Plasma Sources Science and Technology*, vol. 3, pp. 400 – 406, 1994.

[67] U. Kortshagen and U. Bhandarkar, "Modeling of particulate coagulation in low pressure plasmas.," *Physical review. E, Statistical physics, plasmas, fluids, and related interdisciplinary topics*, vol. 60, pp. 887–98, July 1999.

[68] H. R. Maurer and H. Kersten, "On the heating of nano- and microparticles in process plasmas," *Journal of Physics D: Applied Physics*, vol. 44, p. 174029, May 2011.

[69] Z. C. Holman and U. R. Kortshagen, "Solution-processed germanium nanocrystal thin films as materials for low-cost optical and electronic devices.," *Langmuir : the ACS journal of surfaces and colloids*, vol. 25, pp. 11883–9, Oct. 2009.

[70] S. Iyer and Y. H. Xie, "Emission from Silicon," *Science*, vol. 260, pp. 40–46, 1993.

[71] C. Suryanarayana and M. G. Norton, *X-ray diffraction; A practical approach.* Springer - US, 1998.

[72] A. L. Patterson, "The scherrer formula for x-ray particle size determination," *Phys. Rev.*, vol. 56, pp. 978–982, Nov 1939.

[73] G. Sauerbrey, "Verwendung von Schwingquarzen zur Wägung dünner Schichten und zur Mikrowägung," *Z.Phys.*, vol. 155, no. 2, p. 206, 1959.

[74] E.V. Shunko, *Langmuir probe in theory and practice.*
Universal publishers-Boca Raton, Florida, 2009.

[75] B. E. Cherrington, "The use of electrostatic probes for plasma diagnostics-A review," *Plasma Chemistry and Plasma Processing*, vol. 2, no. 2, pp. 113–140, 1982.

[76] N. Hershkowitz, M. H. Cho, and C. H. Nam, "Langmuir probe characteristics in RF glow discharges," *Plasma Chemistry and Plasma Processing*, vol. 8, no. 1, pp. 35–52, 1988.

[77] I. H. Hutchinson, *Principles of plasma diagnostics.*
Cambridge: Cambridge University Press, 2002.

[78] S. T. Bauer G, Pittner F, "Metal nanocluster biosensors," *Microchum Acta*, vol. 114, pp. 107–114, 1999.

[79] G. Schultes, M. Schmidt, M. Truar, D. Goettel, O. Freitag-Weber, and U. Werner, "Co-deposition of silver nanoclusters and sputtered alumina for sensor devices," *Thin Solid Films*, vol. 515, pp. 7790–7797, July 2007.

[80] J. P. Wilcoxon and B. L. Abrams, "Synthesis, structure and properties of metal nanoclusters.," *Chemical Society reviews*, vol. 35, pp. 1162–94, Nov. 2006.

[81] C. Anders, E. M. Bringa, G. Ziegenhain, and H. M. Urbassek, "Stopping of hypervelocity clusters in solids," *New Journal of Physics*, vol. 13, p. 113019, Nov. 2011.

[82] F. Baletto and R. Ferrando, "Structural properties of nanoclusters: Energetic, thermodynamic, and kinetic effects," *Rev. Mod. Phys.*, vol. 77, no. 1, pp. 371–423, 2005.

[83] W. de Heer, "The physics of simple metal clusters: experimental aspects and simple models," *Reviews of Modern Physics*, vol. 65, pp. 611–676, July 1993.

[84] E. Grabowska, H. Remita, and A. Zaleska, "No Title," *Physicochem prob. Miner Proc*, vol. 45, pp. 29–38, 2010.

[85] T. Hihara and K. Sumiyama, "Formation and size control of a Ni cluster by plasma gas condensation," *Journal of Applied Physics*, vol. 84, no. 9, pp. 5270–5276, 1998.

[86] R. E. Palmer, S. Pratontep, and H.-G. Boyen, "Nanostructured surfaces from size-selected clusters.," *Nature materials*, vol. 2, pp. 443–8, July 2003.

[87] I. Shyjumon, M. Gopinadhan, C. a. Helm, B. M. Smirnov, and R. Hippler, "Deposition of titanium/titanium oxide clusters produced by magnetron sputtering," *Thin Solid Films*, vol. 500, pp. 41–51, Apr. 2006.

[88] M. Drabik, A. Choukourov, A. Artemenko, O. Polonskyi, O. Kylian, J. Kousal, L. Nichtova, V. Cimrova, D. Slavinska, and H. Biederman, "Structure and composition of titanium nanocluster films prepared by a gas aggregation cluster source," *The Journal of Physical Chemistry C*, vol. 115, pp. 20937–20944, Nov. 2011.

[89] M. Drabik, A. Choukourov, A. Artemenko, J. Kousal, O. Polonskyi, and P. Solar, "Morphology of Titanium Nanocluster Films Prepared by Gas Aggregation Cluster Source," *Plasma Processes and Polymers*, vol. 8, no. 7, pp. 640–650, 2011.

[90] I. Safi, "Recent aspects concerning DC reactive magnetron sputtering of thin films : a review," *Surf. Coat. Technol.*, vol. 127, pp. 203–219, 2000.

[91] D. Depla, X. Y. Li, S. Mahieu, and R. De Gryse, "Determination of the effective electron emission yields of compound materials," *Journal of Physics D: Applied Physics*, vol. 41, p. 202003, Oct. 2008.

[92] T. Peter, S. Rehders, U. Schürmann, T. Strunskus, V. Zaporojtchenko, and F. Faupel, "High rate deposition system for metal-cluster/SiO x C y H z âpolymer nanocomposite thin films," *Journal of Nanoparticle Research*, vol. 15, p. 1710, May 2013.

[93] P. V. Kashtanov, B. M. Smirnov, and R. Hippler, "Efficiency of cluster generation in a magnetron discharge," *EPL (Europhysics Letters)*, vol. 91, p. 63001, Sept. 2010.

[94] X. Chen and S. S. Mao, "Titanium dioxide nanomaterials: synthesis, properties, modifications, and applications.," *Chemical reviews*, vol. 107, pp. 2891–959, July 2007.

[95] A. Podesta, G. Bongiorno, P. E. Scopelliti, S. Bovio, P. Milani, C. Semprebon, and G. Mistura, "Cluster assembled nanostructured titanium oxide films with tailored wettability," *The Journal of Physical Chemistry C*, vol. 113, pp. 18264–18269, Oct. 2009.

[96] X. Wei, R. Skomski, B. Balamurugan, Z. G. Sun, S. Ducharme, and D. J. Sellmyer, "Magnetism of TiO and TiO[sub 2] nanoclusters," *Journal of Applied Physics*, vol. 105, no. 7, p. 07C517, 2009.

[97] X. Su, Q. Wu, X. Zhan, J. Wu, S. Wei, and Z. Guo, "Advanced titania nanostructures and composites for lithium ion battery," *Journal of Materials Science*, vol. 47, pp. 2519–2534, Sept. 2011.

[98] G. Corbelli, C. Ghisleri, M. Marelli, P. Milani, and L. Ravagnan, "Highly deformable nanostructured elastomeric electrodes with improving conductivity upon cyclical stretching.," *Advanced materials (Deerfield Beach, Fla.)*, vol. 23, pp. 4504–8, Oct. 2011.

[99] A. Choukourov, I. Gordeev, D. Arzhakov, A. Artemenko, O. Kylián, J. Kousal, O. Polonskyi, J. Pešička, D. Slavínská, and H. Biederman, "Nanocomposite gold/poly(ethylene oxide) -like plasma polymers prepared by plasma-assisted vacuum evaporation and magnetron sputtering," *Surface and Coatings Technology*, vol. 205, pp. 2830–2837, Jan. 2011.

[100] T. Caruso, C. Lenardi, R. G. Agostino, M. Amati, G. Bongiorno, T. Mazza, a. Policicchio, V. Formoso, E. Maccallini, E. Colavita, G. Chiarello, P. Finetti, F. Sutara, T. Skála, P. Piseri, K. C. Prince, and P. Milani, "Electronic structure of cluster assembled nanostructured TiO(2) by resonant photoemission at the Ti L(2,3) edge.," *The Journal of chemical physics*, vol. 128, p. 094704, Mar. 2008.

[101] C. Clavero, J. L. Slack, and A. Anders, "Size and composition-controlled fabrication of thermochromic metal oxide nanocrystals," *Journal of Physics D: Applied Physics*, vol. 46, p. 362001, Sept. 2013.

[102] J. Sagás, D. Duarte, and S. Fissmer, "Effect of oxygen concentration and system geometry on the currentâvoltage relations during reactive sputter deposition of titanium dioxide thin films," *Vacuum*, vol. 85, pp. 1042–1046, Apr. 2011.

[103] M. Drabik, a. Choukourov, a. Artemenko, J. Matousek, O. Polonskyi, P. Solar, J. Pesicka, J. Lorincik, D. Slavinska, and H. Biederman, "Aging of nanocluster Ti/TiOx films prepared by means of gas aggregation cluster source," *Surface and Coatings Technology*, vol. 205, pp. S48–S52, July 2011.

[104] Chapman B, *Glow discharge processes: sputtering and plasma etching*. New York: Wiley, 1980.

[105] A. Güntherschulze *, Z.Tech. Phys*, vol. 11, p. 49, 1930.

[106] A. Lompe, R. Seeliger, and E. Wolter, "Untersuchungen an Hohlkathoden," *Annalen Der Physik*, vol. 36, pp. 9–37 (In German), 1939.

[107] H. Helm, "Experimenteller Nachweis des Pendel-Effektes in einer zylindrischen Niederdruck-Hohlkathoden-Entladung in Argon," *Naturforsch.A*, vol. 27, p. 1812, 1972.

[108] M. E. Pillow, "A critical review of spectral and related physical properties of the hollow cathode discharge," *Spectrochimica Acta, Part B*, vol. 36B, no. 8, pp. 821–843, 1981.

[109] S. Komiya, "Physical vapor deposition of thick Cr and its carbide and nitride films by hollow-cathode discharge," *Journal of Vacuum Science and Technology*, vol. 13, p. 520, Jan. 1976.

[110] Y. S. Kuo, "Hot hollow cathode and its applications in vacuum coating: A concise review," *Journal of Vacuum Science & Technology A: Vacuum, Surfaces, and Films*, vol. 4, p. 397, May 1986.

[111] M. Quitzau and H. Kersten, "Determination of electron density and energy influx in a hollow cathode glow discharge used for powder modification," *The European Physical Journal D*, vol. 66, p. 47, Feb. 2012.

[112] I. L. Alberts, D. S. Barratt, A. K. Ray, and S. Member, "Hollow Cathode Effect in Cold Cathode Fluorescent Lamps : A Review," *Journal of Display Technology*, vol. 6, no. 2, pp. 52–59, 2010.

[113] M. Nistor, P. Charles, M. Ganciu, and M. Lamoureux, "Electron energy distribution function in a transient open-ended hollow cathode," *Plasma Sources Science and Technology*, vol. 11, pp. 183–189, 2002.

[114] D. M. Goebel, K. K. Jameson, I. Katz, and I. G. Mikellides, "Potential fluctuations and energetic ion production in hollow cathode discharges," *Physics of Plasmas*, vol. 14, no. 10, p. 103508, 2007.

[115] S. Tanaka, A. Masato, H. Hiroshi, O. Yoshikazu, Ohara, and Yoshihiro, "Effect of magnetic field on the characteristics of a hollow cathode ion source," *Review of Scientific Instruments*, vol. 54, no. 9, p. 1104, 1983.

[116] A. Latuszynski, A. Droździel, K. Pyszniak, J. Dupak, D. Mäczka, and J. Meldizon, "Plasma ion source with hollow cathode," *Vacuum*, vol. 70, pp. 451–455, Mar. 2003.

[117] C. M. Horwitz, "Hollow cathode reactive sputter etchingâA new high-rate process," *Applied Physics Letters*, vol. 43, no. 10, p. 977, 1983.

[118] C. M. Horwitz, , , and D. R. McKenzie, "High rate Hollow cathode amorphous silicon deposition," *Application of Surface Science*, vol. 22-23, pp. 925–929, 1985.

[119] C. Lejeune, J. P. Grandchamp, , O. Kessi, and J. P. Gilles, "RF multipolar plasma for broad and reactive ion beams," *Vaccum*, vol. 36 (11-12), pp. 837–840, 1986.

[120] L. Bardos, H. Barankova, and Y. Lebedev, "Performance of radio frequency hollow cathodes at low gas pressures," *Surf. Coat. Technol.*, vol. 163-164, pp. 654–658, 2003.

[121] L. Bardos, "Radio frequency hollow cathodes for the plasma processing technology," *Surf. Coat. Technol.*, vol. 86-87, pp. 648–656, 1996.

[122] V. A. Godyak, R. B. Piejak, and B. M. Alexandrovich, "Probe diagnostics of non-Maxwellian plasmas," *Journal of Applied Physics*, vol. 73, no. 8, p. 3657, 1993.

[123] V. A. Godyak and V. I. Demidov, "Probe measurements of electron-energy distributions in plasmas: what can we measure and how can we achieve reliable results?," *Journal of Physics D: Applied Physics*, vol. 44, p. 233001, July 2011.

[124] T. Lafleur and R. W. Boswell, "Particle-in-cell simulations of hollow cathode enhanced capacitively coupled radio frequency discharges," *Physics of Plasmas*, vol. 19, no. 2, p. 023508, 2012.

[125] M. B. Hopkins, "Langmuir Probe Measurements in the Gaseous Electronics Conference RF Reference Cell," *Journal of Research of the national Institute of Standard and Technology*, vol. 100, no. 4, pp. 415–425, 1995.

[126] R. W. Boswell and A. Bouchoute, "A Comparison between RF-Driven Single and Double Cathode Structures," *Plasma Chemistry and Plasma Processing*, vol. 8, no. 1, pp. 53–66, 1988.

[127] V. A. Godyak, R. B. Piejak, and B. M. Alexandrovich, "Electrical Characteristics of Parallel-Plate RF Discharges in Argon," *IEEE Transactions on Plasma Science*, vol. 19, no. 4, p. 660, 1991.

[128] Y. Catherine and P. Couderc, "Electrical characteristics and growth kinetics in discharges used for plasma deposition of amorphous carbon," *Thin Solid Films*, vol. 144, pp. 265–280, 1986.

[129] N. Mutsukura, K. Kobayashi, and Y. Machi, "Plasma sheath thickness in radio-frequency discharges," *Journal of Applied Physics*, vol. 68, no. 6, p. 2657, 1990.

[130] K. J. Taylor, S. Yun, and G. R. Tynan, "Control of plasma parameters by using noble gas admixtures," *Journal of Vacuum Science & Technology A: Vacuum, Surfaces, and Films*, vol. 22, no. 5, p. 2131, 2004.

[131] K. J. Taylor and G. R. Tynan, "Control of dissociation by varying oxygen pressure in noble gas admixtures for plasma processing," *Journal of Vacuum Science & Technology A: Vacuum, Surfaces, and Films*, vol. 23, no. 4, p. 643, 2005.

[132] P. Kocian, "Radial density distribution of charged particles in an electronegative discharge plasma with space charges," *Physics of Fluids*, vol. 18, no. 12, p. 1710, 1975.

[133] H. Nakanishi, K. J. M. Bishop, B. Kowalczyk, A. Nitzan, E. a. Weiss, K. V. Tretiakov, M. M. Apodaca, R. Klajn, J. F. Stoddart, and B. a. Grzybowski, "Photoconductance and inverse photoconductance in films of functionalized metal nanoparticles.," *Nature*, vol. 460, pp. 371–5, July 2009.

[134] R. Subbiah, M. Veerapandian, and K. S. Yun, "Nanoparticles: functionalization and multifunctional applications in biomedical sciences," *Current Medicinal Chemistry*, vol. 17, pp. 4559–4577, 2010.

[135] S. Jiang, K. Y. Win, S. Liu, C. P. Teng, Y. Zheng, and M.-Y. Han, "Surface-functionalized nanoparticles for biosensing and imaging-guided therapeutics.," *Nanoscale*, vol. 5, pp. 3127–48, Apr. 2013.

[136] I. Yamada and G. H. Takaoka, "Ionized cluster beams: physics and technology," *Japanese Journal of Applied Physics*, vol. 32, no. 5A, p. 2121, 1993.

[137] L. Ravagnan, G. Divitini, S. Rebasti, M. Marelli, P. Piseri, and P. Milani, "Poly(methyl methacrylate)âpalladium clusters nanocomposite formation by supersonic cluster beam deposition: a method for microstructured metallization of polymer surfaces," *Journal of Physics D: Applied Physics*, vol. 42, p. 082002, Apr. 2009.

[138] T. Hanemann and D. V. Szabó, "Polymer-Nanoparticle Composites: From Synthesis to Modern Applications," *Materials*, vol. 3, pp. 3468–3517, May 2010.

[139] R. Katoh, T. Hihara, D. L. Peng, and K. Sumiyama, "Composite deposition of Co and Si clusters by rf/dc plasma-gas-codensation," *Applied Physics Letters*, vol. 82, no. 16, p. 2688, 2003.

[140] A. A. Turkin, M. V. Dutka, Y. T. Pei, D. I. Vainshtein, and J. T. M. De Hosson, "On the evolution of nanocluster size distribution in a nanocluster aggregation source," *Journal of Applied Physics*, vol. 111, no. 12, p. 124326, 2012.

[141] B. Balasubramanian, K. L. Kraemer, S. R. Valloppilly, S. Ducharme, and D. J. Sellmyer, "Cluster synthesis of monodisperse rutile-TiO2 nanoparticles and dielectric TiO2-vinylidene fluoride oligomer nanocomposites.," *Nanotechnology*, vol. 22, p. 405605, Oct. 2011.

[142] F. Faupel, V. Zaporojtchenko, H. Greve, U. Schürmann, V. S. K. Chakravadhanula, C. Hanisch, a. Kulkarni, a. Gerber, E. Quandt, and R. Podschun, "Deposition of nanocomposites by plasmas," *Contributions to Plasma Physics*, vol. 47, pp. 537–544, Nov. 2007.

[143] B. Gojdka, V. Zaporojtchenko, V. Hrkac, J. Xiong, L. Kienle, T. Strunskus, and F. Faupel, "Highly versatile concept for precise tailoring of nanogranular composites with a gas aggregation cluster source," *Applied Physics Letters*, vol. 100, no. 13, p. 133104, 2012.

[144] A. M. Ahadi, T. Trottenberg, S. Rehders, T. Strunskus, H. Kersten, and F. Faupel, "Characterization of a radio frequency hollow electrode discharge at low gas pressures," *Physics of Plasmas*, vol. 22, p. 83513, 2015.

[145] T. Baloniak, R. Reuter, C. Flötgen, and A. von Keudell, "Calibration of a miniaturized retarding field analyzer for low-temperature plasmas: geometrical transparency and collisional effects," *Journal of Physics D: Applied Physics*, vol. 43, no. 5, p. 055203, 2010.

[146] A. Dinklage, T. Klinger, G. Marx and L. Schweikhard, *Plasma physics: confinement, transport and collective effects.*
Springer, Berlin-Heidelberg, 2005.

[147] J. Kousal, O. Polonskyi, O. Kylián, A. Choukourov, A. Artemenko, J. Pešička, D. Slavínská, and H. Biederman, "Characterization of nanoparticle flow produced by gas aggregation source," *Vacuum*, vol. 96, pp. 32–38, Oct. 2013.

[148] T. Trottenberg, B. Brede, D. Block, and A. Piel, "Resonance cones in a dusty magnetized plasma," *Physics of Plasmas*, vol. 10, no. 12, p. 4627, 2003.

[149] O. Havnes, G. E. Morfill, and C. K. Goertz, "Plasma potential and grain charges in a dust cloud embedded in a plasma," *Journal of Geophysical Research: Space Physics*, vol. 89, no. A12, pp. 10999 –11003, 1984.

[150] W. U. Huynh, J. J. Dittmer, and A. P. Alivisatos, "Hybrid Nanorod-Polymer solar cells," *Science*, vol. 295, no. March, pp. 2425–2428, 2002.

[151] K.-Y. Cheng, R. Anthony, U. R. Kortshagen, and R. J. Holmes, "High efficiency silicon nanocrystal light emitting devices," *Nano letters*, vol. 11, pp. 1952–1956, 2011.

[152] Z. C. Holman, C.-Y. Liu, and U. R. Kortshagen, "Germanium and silicon nanocrystal thin-film field-effect transistors from solution.," *Nano letters*, vol. 10, pp. 2661–6, July 2010.

[153] D. L. Klein, R. Roth, and A. K. L. Lim, "A single-electron transistor made from a cadmium selenide nanocrystal," *Nature*, vol. 389, pp. 699–701, 1997.

[154] S. Prabakar, A. Shiohara, S. Hanada, K. Fujioka, K. Yamamoto, and R. D. Tilley, "Size controlled synthesis of germanium nanocrystals by hydride reducing agents and their biological applications," *Chemistry of Materials*, vol. 22, pp. 482–486, Jan. 2010.

[155] N. A. Hill, S. Pokrant, A. J. Hill, B. Laboratories, L. Technologies, M. Ave, and M. Hill, "Optical Properties of Si-Ge Semiconductor Nano-Onions," *Journal of Physical Chemistry B*, vol. 103, pp. 3156–3161, 1999.

[156] L. T. Canham, "Silicon quantum wire array fabrication by electrochemical and chemical dissolution of wafers," *Applied Physics Letters*, vol. 57, no. 10, p. 1046, 1990.

[157] T. Takagahara and K. Takeda, "Theory of quantum confinement effect on excitons in quantum dots of indirect-gap materials," *Physical review B*, vol. 46, no. 23, pp. 578–581, 1992.

[158] G. Nesher, L. Kronik, and J. R. Chelikowsky, "Ab initio absorption spectra of Ge nanocrystals," *Physical Review B*, vol. 71, p. 035344, Jan. 2005.

[159] J. P. Wilcoxon, P. P. Provencio, and G. A. Samara, "Synthesis and optical properties of colloidal germanium nanocrystals," *Phys. Rev. B*, vol. 64, p. 35417, June 2001.

[160] W. Wang, J. Huang, and Z. Ren, "Synthesis of germanium nanocubes by a low temperature inverse micelle solvothermal technique," *Langmuir*, vol. 21, no. 2, pp. 751–754, 2005.

[161] D. C. Lee, J. M. Pietryga, I. Robel, D. J. Werder, R. D. Schaller, and V. I. Klimov, "Colloidal synthesis of infrared emitting germanium nanocrystals," *Journal of the American Chemical Society*, vol. 131, pp. 3436–3437, 2009.

[162] L. M. Wheeler, L. M. Levij, and U. R. Kortshagen, "Tunable band gap emission and surface passivation of germanium nanocrystals synthesized in the gas phase," *The Journal of Physical Chemistry Letters*, vol. 4, p. 3392, 2013.

[163] T. Matsoukas and M. Russell, "Particle charging in low-pressure plasmas," *Journal of Applied Physics*, vol. 77, no. 9, p. 4285, 1995.

[164] D. A. Ruddy, J. C. Johnson, E. R. Smith, and N. R. Neale, "Size and Bandgap Control in the solution- Phase Synthesis of Near Infrared-Emitting Germanium Nanocrystals," *ACS nano*, vol. 4, no. 12, pp. 7459–7466, 2010.

[165] A. Bogaerts, "Computer simulations of argon-hydrogen Grimm-type glow discharges," *Journal of Analytical Atomic Spectrometry*, vol. 23, no. 11, pp. 1476–1486, 2008.

[166] K. Nakagawa, Y. Yoshida, S. Miyazaki, and M. Hirose, "Insights into surface reactions during a-SiGe : H deposition and hydrogen plasma annealing as obtained from infrared attenuated total reflection spectroscopy," *Journal of Non-Crystalline Solids*, vol. 227-230, pp. 48–52, 1998.

[167] C. J. Fang, K. J. Gruntz, L. Ley, M. Cardona, F. J. Demond, G. Müller, and S. Kalbitzer, "The hydrogen content of a-Ge:H and a-Si:H as determined by ir spectroscopy, gas evolution and nuclear reaction techniques," *Journal of Non-Crystalline Solids*, vol. 35â36, Par, pp. 255–260, Jan. 1980.

[168] J. Joseph and E. D. Jemmis, "Red- , Blue- , or No-Shift in Hydrogen Bonds : A Unified Explanation," *Jopurnal of American Chemical Society*, vol. 129, pp. 4620–4632, 2007.

[169] A. M. Ahadi, A. Hinz, O. Polonskyi, T. Trottenberg, T. Strunskus, H. Kersten, and F. Faupel, "Modification of a metal nanoparticle beam by a hollow electrode discharge," *Journal of Vacuum Science & Technology A: Vacuum, Surfaces, and Films*, vol. 34, no. 2, pp. 1–6, 2016.

[170] A. M. Ahadi, N. J. Kramer, T. Strunskus, H. Kersten, F. Faupel, and R. Kortshagen, "Controlled synthesis of germanium nanoparticles by nonthermal plasmas," *Applied Physics Letters*, vol. 108 (9), p. 93105, 2016.